TOWARDS A METHOD TO QUANTIFY PLASTIC LOSS OF A FLOATING BARRIER DUE TO WAVE OVERTOPPING

Graduation thesis by H.M. Limburg

TOWARDS A METHOD TO QUANTIFY PLASTIC LOSS OF A FLOATING BARRIER SYSTEM DUE TO WAVE OVERTOPPING

by

Hans Maarten Limburg
Author[1]
Delft University of Technology & The Ocean Cleanup
Delft, Netherlands

Under the guidance of

Prof. Dr. Ir. R.A.P. van 't Veer
Graduate Professor
Delft University of Technology
Delft, Netherlands

Dr. Ir. P.W. Wellens
University Supervisor
Delft University of Technology
Delft, Netherlands

Ir. J.S. Vérjut
Company Supervisor
The Ocean Cleanup
Delft, Netherlands

Dr. Ir. B. Sainte-Rose
Company Supervisor
The Ocean Cleanup
Delft, Netherlands

Graduation committee:
Prof. Dr. Ir. A.P. van 't Veer
Dr. Ir. P.R. Wellens
Ir. K. Visser
Dr. Ir. B. Sainte-Rose
Ir. J.S. Vérjut

[1] Thesis report was submitted on 15-05-2018 in partial fulfillment for the degree Master of Science in Offshore & Dredging Engineering at Delft University of Technology, Delft, The Netherlands.

Preface

This report is the result of my graduation project at The Ocean Cleanup. Within a few weeks I will give a colloquium about my work and conclude my study period at Delft University of Technology. My research project was part of the work on plastic capturing efficiency studies performed by The Ocean Cleanup.

Carrying out my research project has been of great joy as it allowed me to dig deeper into subjects that really struck my interest. Carrying it out for The Ocean Cleanup feels special as I was able to dedicate my work to a good cause. It makes me feel privileged that I could add value to their ambitious goal to rid the oceans of plastic. All in all, the process leading to this report has been a great journey and I feel humble that I may present my results at a conference in Madrid.

Achievements never come easy however, this was something I've already learned during my rowing activities next to my studies. My greatest struggle was thus not putting a lot of effort in my research work, but rather know how to put an end to it. During my research I often found myself trying to explain it all. Finally, I had to accept that when you're doing research, your work is never finished. It comforts me that I am not the only one struggling with this. I am not so much for the cheesy quotes, but I recently stumbled upon a saying by Sir Isaac Newton that exactly covers this. He once said: "To explain all nature is too difficult a task for any one age. 'Tis much better to do a little with certainty, and leave the rest for others that come after you, than explain all things".

The first people I would like to mention are the ones who supervised my research. Without them this work would just be incomplete. Peter, our weekly meetings were really valuable to me. Having access to your knowledge provided me of great guidance. I would also like to thank you for pushing me to take the hurdles I encountered during my research (sometimes these hurdles were set up by myself). A turning point in my research process was the moment when you drew the brand logo of a well-known sports apparel accompanied with their slogan: "just do it". Bruno, you were a constant source of valuable input to my work. Next to this you provided me with some great lessons on academic writing. Your thorough revisions of my work are greatly appreciated. I would also like to thank you for being available at unconventional hours when I was (again) running late for a deadline. It is not forgotten that you saved me from getting a mental breakdown when my computer crashed, just before I had to hand in my conference paper. After reminding me of the existence of Murphy's law, you provided a valuable helping hand. Jean-Sébastien, having access to your knowledge on hydrodynamics and your years of practical experience were very useful to me. You were always available to explain hydrodynamic concepts to me. Your input and recommendations formed the foundation of my research and you helped me to shape my work into something meaningful.

After my graduation I will continue my work for The Ocean Cleanup. I would like to express my gratitude to my colleagues for believing in me, but also for being so much fun! You guys provide the best working environment I could ever wish for. Your "nothing is impossible" mentality inspires me and I am really happy that my adventure continues with you. A special mention is in place for the colleagues who provided me with data and helped shaping my ideas: Reijnder, Bénédicte, Hendrik, Jetteke, Laurent, Fedde and Jaap.

To all the study friends, rowing friends and colleagues I met during my time in Delft: Thank you for making my student life so joyful!! I won't mention you all by name as this would probably extend this preface by an extra page (and it would be sad if I accidently forgot someone). A special mention goes out to the housemates I had in Delft. Thank you Jelle, Gerrit, Wessel, Sigurd, Daan and Aubin for playing part in some of the best memories I have from my time spent in Delft. Also, thank you for being there for me when needed.

I would like to express my gratitude to my family for always believing in me. I really feel blessed to have you. It is great to have a family on which you can always fall back to. Finally, I would dedicate this work to my grandmother, who recently passed away.

Hans Maarten Limburg
Delft, May 15th 2018

Abstract

Plastic pollution in the marine environment is an increasing problem with severe impacts on ecosystems and economies around the globe. The Ocean Cleanup (TOC) Foundation develops a floating barrier able to intercept, concentrate and extract plastic from the marine environment. TOC has conducted several experiments and numerical studies to determine the plastic capturing efficiency of its system. One of the phenomena leading to degradation of capturing efficiency is wave overtopping. During a wave overtopping event, the system is not able to properly follow the waves. This allows water to wash over the system and possibly lead to plastic, which was retained by the system, escape into the open ocean. This issue is amplified by the use of a stiffer barrier than the original concept that was developed by TOC.

To model and quantify plastic loss due to wave overtopping, the ideal approach would be to use a nonlinear 3D CFD method including hydro-elasticity of the barrier structure. Given the size of the problem and the number of conditions that need to be simulated to characterize the design space of the system, the use of such a method is computationally expensive and therefore unrealistic. Therefore, the objective of this work is to propose an alternative method. A method is presented which aims to quantify overtopping volumes by coupling a hydrodynamic solver to a 2D CFD solver. This thesis work will present the method in three parts.

Part I develops a hydrodynamic model to predict the first order (linear) motion response to wave excitation of a 2D cylinder with a spring attached. It is proposed that this model approximates the motions of a 2D cross-section of a long flexible cylinder subject to random wave excitation. The model's output is a time trace of the motion response, which allows for coupling to a 2D CFD solver. It is found that the spring constant is dependent on the wave characteristics of the ambient wave field. Also, the ability of the 2D cylinder to follow waves is sensitive to the spring stiffness introduced in the model.

Derivation of the spring constant is handled in part II. Here, A model to approximate bending effects into a linear spring is set up. The ambient 3D wave field surrounding the capturing system is modelled and wave statistics are derived. Based on these wave statistics, spring constants are derived for given physical and environmental configurations. From the results it is found that for the wave cases 1 to 4, values of the equivalent spring stiffness coefficient are significant enough to influence the motion response of the floater. For case 5 and 6, values for the equivalent spring stiffness are relatively low and its influence on the response is expected to be negligible.

Part III handles coupling of the hydrodynamic model to the CFD solver ComFLOW. In the cases with low wave steepness, derivation of overtopping statistics has been achieved and results show that overtopping performance can be assessed by performing the steps taken in this research project. In these cases, the wave field is generally behaving linear and the motion response obtained from the hydrodynamic model can be coupled to the CFD solver. Results show that wave height and the applied spring stiffness are governing parameters for overtopping performance. It was also found that in some cases, non-linearities are introduced in the wave field. In the cases where non-linearities occur, the motion response derived by the hydrodynamic model deviates from the motion response that one would expect.

Table of Contents

List of figures

List of tables

Nomenclature

Abbreviations:

TOC	*The Ocean Cleanup*
PCS	Plastic Capturing System
GPGP	*Great Pacific Garbage Patch*
JONSWAP	*Joint North Sea Wave Project*
CFD	*Computational Fluid Dynamics*
EOM	*Equation of motion*
RAO	*Response Amplitude Operator*
VOF	*Volume of Fluid*
NWT	*Numerical Wave Tank*

symbols:

t	*time*	H	*Wave height*
x	*Position along x-axis / displacement in surge*	η	*Wave amplitude*
y	*Position along y-axis / displacement in sway*	λ	*Wave length*

z	*Position along z-axis / displacement in heave*	T	*Wave period*
$u, \dot{x}$	*Velocity in x-direction*	ω	*Wave frequency*
$v, \dot{y}$	*Velocity in y-direction*	k	*Wave number*
$w, \dot{z}$	*Velocity in z-direction*	φ	*Phase*
$\dot{u}, \ddot{x}$	*Acceleration in x-direction*	θ	*Wave direction*
$\dot{v}, \ddot{y}$	*Acceleration in y-direction*	s	*Depending on subscript:*
$\dot{w}, \ddot{z}$	*Acceleration in z-direction*		*s: wave steepness*
h	*Heave motion*		s_p*: relative vertical motion*
ζ	*Wave elevation*	g	*Gravitational constant*
γ	*gamma*	d, h	*Depth*
P	*Position of point P*	ϕ	*Wave potential*
$\boldsymbol{u}$	*Velocity vector* $\boldsymbol{u} = (u, v, w)^T$	p	*pressure*
L	*Length*	KC	*KC-number*
D	*Diameter*	Re	*Reynolds number*
r	*Radius*	a	*Added mass coefficient*
f	*Geometrical freeboard*	b	*Hydrodynamic damping coefficient*
T	*Draft*	c	*Hydrostatic coefficient*
M	*Unit dry mass*	F	*Force*
EI	*Bending stiffness*	ρ	*Density*
S	*Depending on subscript:*	δ	*Deflection*
	S_{swl}*: Sea waterline area*	q	*Distributed force*
	S*: Position free surface*	μ	*Dynamic viscosity*
	S_{z_a}*: Response spectrum*	ν	*Kinematic viscosity*
Ω	*Domain*	σ	*Stress*
Γ	*Domain boundary*	κ	*Coefficient of bulk viscosity*
dt	*Time step*	Q	*Volumetric flow rate*
A	*Axis*	V	*Volume*
$\boldsymbol{x}$	*Point x*		
$\boldsymbol{y}$	*Point y*		
$\boldsymbol{q}$	*Point q*		

Subscripts:

0	*Origin*	$hydrodynamic$	*Hydrodynamic*
$mean$	*Mean of a variable*	$hydrostatic$	*Hydrostatic*
e	*Effective*	FK	*Froude-Krylov*
f	*Floater*	in	*Inlet*
f	*Skirt*	out	*Outlet*
p	*Value in point P*	n	*Normal direction*
r	*Relative*	t	*Tangential direction*
s, $1/3$	*Significant / highest* $\frac{1}{3}$	max	*Max value*
i, j	*Index numbers*	$FEMAP$	*value derived from FEMAP*
o	*Outer*	$Major$	*major*
dry	*Dry*	$Minor$	*minor*
a	*Amplitude*	up	*up-crossing*
orb	*Orbital*	$down$	*down-crossing*
11	*Surge (uncoupled)*	q	*Point q*
33	*Heave (uncoupled)*	$K0$	*Zero stiffness*
$Kinf$	*Infinite stiffness*	Kp_50	*50th percentile stiffness*
Kp_20	*20th percentile stiffness*	Kp_05	*5th percentile stiffness*

MAIN MATTER

1 Introduction

1.1 PLASTIC POLLUTION IN OUR OCEANS

As described by Susan Freinkel in her book 'Plastic – A toxic love story', life in 'Plasticville' has become a fact. Our present-day lives are impossible to imagine without the use of plastics. It made possible today's living standard and created 'wealth for the masses'. Plastic provides unique properties at low cost and therefore plays a centralized role in satisfying our need for consumer goods. Since the 1950's, global plastic production has shown an exponential growth reaching 322 million tonnes a year in 2015 [1]. Due to its availability and being inexpensive, plastics are becoming more and more of a short-term-use product. Modern days society may well be distinguished as a 'throw-away-society'. Unfortunately, this society only tends to forget that the world is not a disposable product.

Main inputs of plastic waste in the environment are due to waste mismanagement and improper human behavior (incorrect disposal) [2]. As a result, an averaged 8 million tonnes of plastic leaks into the marine environment annually [3]. After entering the ocean waters, plastic debris are influenced by ocean currents transporting them over large distances [4]. Eventually, it washes ashore or ends up in gyres that act as accumulation zones [4,5]. The largest zone, known as the Great Pacific Garbage Patch (GPGP), is located between Hawaii and California. Recently the GPGP has been estimated to cover an area of 1.6 million km^2, containing 1.8 trillion pieces of plastic with a combined mass of 79000 tonnes [6].

One of the most desirable properties plastic possesses is durability. However, once having entered the marine environment, the fact that plastic deteriorates slowly, becomes a curse. It takes decades, up to centuries, for plastic to break down into basic elements harmless to nature. According to a study performed by The Ocean Cleanup, plastic debris form several hazards [7]:

- **Ecological hazards**: Marine species may become entangled in large debris, while smaller debris is ingested when taken for food. Also, potentially invasive species are known to harm ecosystems when they travel with marine debris towards new areas.
- **Damage to economy**: Plastic debris causes direct and indirect economical loss to a society. Direct costs are related to damage to an industry. Indirect cost manifests itself as loss of income due to degraded benefits from the oceans.
- **Eco-toxic hazards:** Organisms could absorb toxic additives sometimes found in plastic into their cell tissue. This particularly forms a hazard for organisms high in the food chain, due to accumulation of these additives.

Despite raising awareness by several institutions [8-12], the problem of marine pollution is expected to increase in the future. By 2050, projections show that the oceans could contain more plastic than fish (in weight ratio) [11].

1.2 THE OCEAN CLEANUP FOUNDATION

The Ocean Cleanup (TOC) was founded in 2013 by Boyan Slat in order to realize his goal to rid the oceans of plastic pollution. Based in Delft, TOC is developing a plastic capturing system (PCS) to make possible the biggest cleanup in history. Their ocean engineering team is currently working on the structural design and hydrodynamics of this system.

1.3 A PASSIVE PLASTIC CAPTURING SYSTEM

The largest fraction of buoyant plastics is found on or near the ocean's surface [13]. As stated earlier, it is known that plastic debris drifts with the governing ocean surface currents. These findings imply that a floating barrier system could be efficient in capturing plastics when it is able to follow the surface currents (and thus the plastic debris). Now, if a relative velocity of the barrier system with respect to the ocean surface current is introduced, it is possible to capture and retain plastic debris inside the barrier. Figure 1 depicts the workings of the current concept. The PCS consists of a floater with a screen attached underneath. The PCS will passively float with the current, just like the plastics. Governing winds induce a drag load on the system. This results in a difference in velocity of the barrier with respect to the surrounding debris. Also, the system is designed to be wind-vaning: it orients itself with the predominant direction of the wind. Assuming the deployment of a fleet of cleanup systems with a combined span of 100 kilometers, internal developed models show it is possible to reduce the plastic content of the GPGP by 50% within five years.

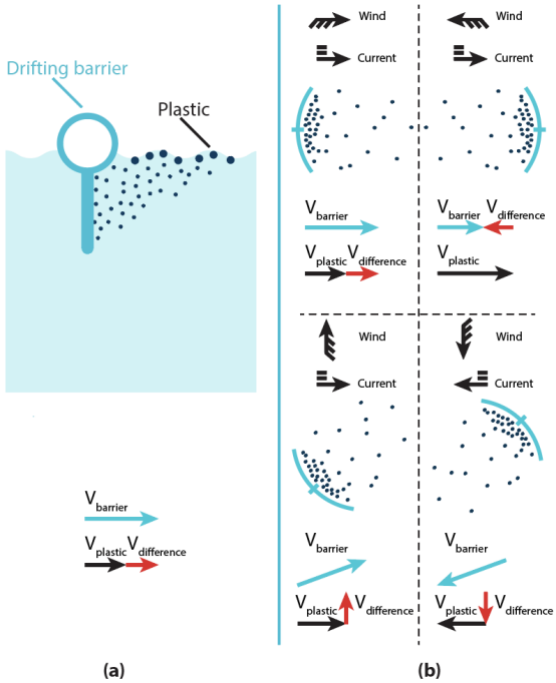

Figure 1 – Schematic drawings of the PCS workings. (a) Cross-sectional view of the barrier showing plastic collecting in front of the floating barrier system. (b) Top view of the barrier showing the barrier catching plastic under several environmental wind and current directions [Image courtesy of The Ocean Cleanup]

2 Problem analysis & research plan

2.1 FUNCTIONAL DESCRIPTION

The Ocean Cleanup states its mission as [14]:

"The Ocean Cleanup's mission is to develop advanced technologies to rid the oceans of plastic"

The main function of the PCS is thus to catch plastic debris from the ocean and preventing it from escaping again. The functional description of the PCS can therefore be defined as:

"The capability of catching and retaining plastic debris at the floating barrier"

2.2 PLASTIC ESCAPING PHENOMENA

Wave-, wind- and current action might lead to functional degradation of the barrier. Figure 2, on the right, shows an overview of the failure mechanisms identified:

1. **Plastic loss due to leakage under boom:** Occurs due to wave action, current action and/or accumulation failures
    a. **Boom bridging**: Floater rests on the wave crest, creating a reduced draft in the troughs. The reduced draft allows plastics to escape underneath the screen.
    b. **Boom planing**: Wave and/or current action reduces draft due to an induced pitch motion. The reduced draft allows plastics to escape underneath the screen.
    c. **Entrainment:** The fluid flow under passing the barrier is sufficient to counteract plastic rising velocity.
    d. **Accumulation failures:** The volume of debris exceeds the capacity of the barrier. Plastic accumulates and (partly) leaks away underneath the barrier.
2. **Plastic loss due to leakage over boom:** Occurs due to wind and/or wave action.
    a. **Wave overtopping**
        i. **Boom submergence:** Insufficiently following of vertical free surface elevation and waves run over the barrier system. Causing debris to wash over.
        ii. **Splash over:** High relative horizontal fluid velocities with respect to the barrier cause water and thus plastics to splash over the barrier.
    b. **Spray over**: Wind action may cause plastics to spray over the barrier.
3. **Plastic loss due to difference in directional velocity:** Action by reflected/radiation waves and/or current cause debris to drift away from the barrier system.

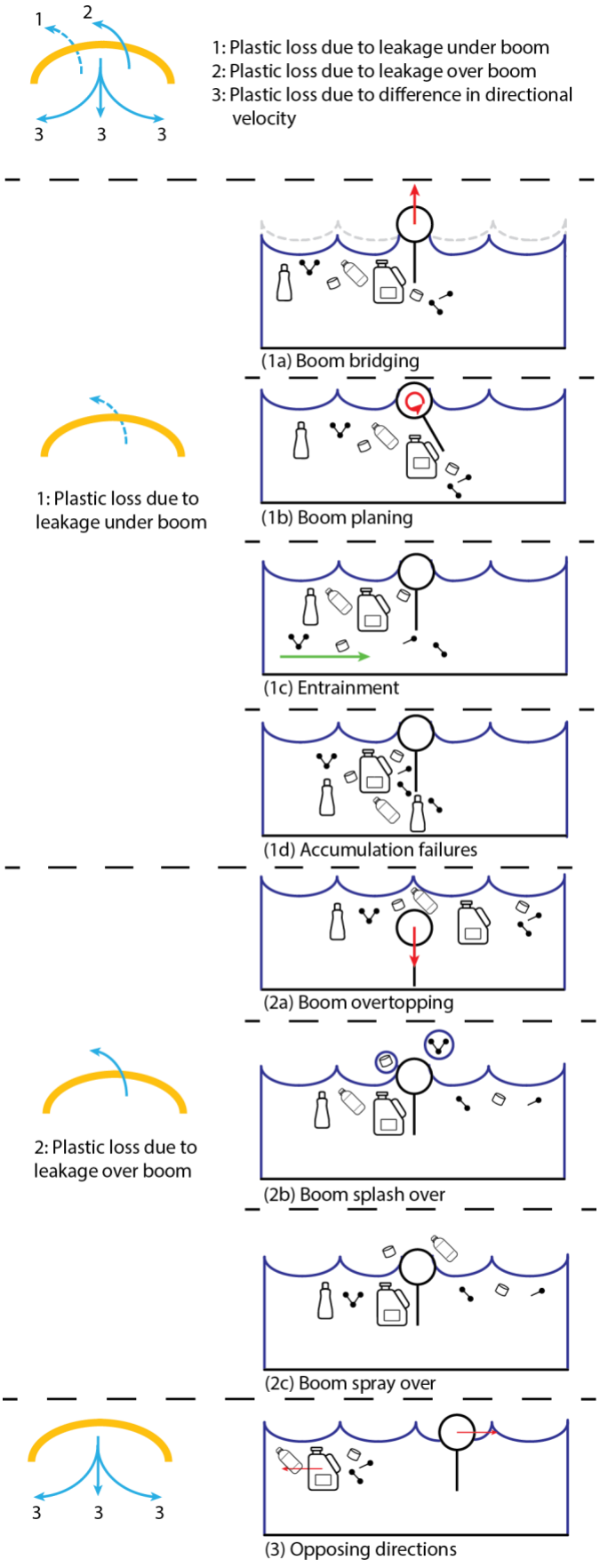

Figure 2 - Identified mechanisms of failure leading to functional degradation of the PCS.

2.3 PROBLEM STATEMENT

In order to design an efficient cleanup system, plastic escaping phenomena should be reduced to a minimum. Concerning this goal, The Ocean Cleanup is interested in developing a tool able to identify plastic loss due to wave overtopping. The research focus of this thesis project is the development of a method which is able to quantify wave overtopping over the structure.

Wave overtopping is a local wave-structure interaction occurring along the barrier causing water to run over the structure. This phenomenon can be subdivided into 2 parts. During boom submergence, the floater is pulled under water in a wave crest and water runs over the barrier. In the case of boom splash over, high relative horizontal fluid velocities cause water to splash over. This means that in order to reach effective containment, the barrier should follow the vertical surface elevation in waves and high relative horizontal velocities must be avoided. This is one of the conclusions drawn from previous research on the performance of pollution containment barriers [15].

The dynamic response of a floating barrier system to the prevailing environmental conditions is a complex phenomenon. It involves large relative accelerations, hydro-elasticity, fluid-structure interaction, and large relative vertical motions with respect to the floaters diameter.

2.4 PREVIOUS RESEARCH CONDUCTED BY TOC

During the concept design phase, several tests and studies concerning barrier hydrodynamics have been conducted. In 2015, Deltares measured wave forcing on a 2D scale model [16]. Based on these measurements, Mocean conducted a comparison study [17] with 2D hydrodynamic numerical models developed at The Ocean Cleanup. Outcome of the study showed that the 2D numerical models, at the time, matched the test results insufficiently. Later in 2015, another test was conducted by Mocean (using MARIN test facilities) to gain a better understanding of the flexible barrier hydrodynamics [18]. This test considered a 3D floating barrier scale model subject to waves and currents from different directions. Although it gave a better understanding of barrier hydrodynamics, it was not possible to quantify overtopping using these tests. Overtopping was only visually observed, pictures taken of a few events. Conclusions drawn from test results where that some cases yielded overtopping, in particular for short-crested wave conditions.

No further quantification was made. Figure 3 shows an overtopping event observed during the scale model tests conducted by Mocean at MARIN test facilities.

In addition to the limited information on overtopping that can be drawn from previous research, it should be noted that, there has been a concept change. In the updated design, the material of the floater part is changed to a stiffer material when compared to the old design. Previous results might be only partially useful for the understanding of overtopping phenomena.

2.5 DISCUSSION ON METHODOLOGY

To model and quantify plastic loss due to wave overtopping, the ideal approach would be to use a nonlinear 3D CFD method including hydro-elasticity of the barrier structure. Given the size of the problem and the number of conditions that need to be simulated to characterize the design space of the system, the use of such a method is computationally very expensive and

Figure 3 – Visually observed overtopping event during scale model tests conducted by Mocean at MARIN test facilities in 2015. (Image courtesy of The Ocean Cleanup)

therefore unrealistic. This work proposes an alternative method: that overtopping results can be drawn by coupling a hydrodynamic solver to a 2D CFD solver.

2.6 RESEARCH OBJECTIVE

The aim is to develop a method able to quantify overtopping volumes due to boom overtopping of the floating barrier system. This method is then used to conduct a performance analysis with respect to the functional efficiency of the barrier.

In order to develop this methodology, the following topics are of interest:

- 2D dynamic behavior of floating barrier system
- 3D dynamic behavior of floating barrier system
- Influencing parameters on overtopping
- Environmental conditions

The actual loss of plastic not only depends on the dynamic behavior of the floater, but also on the behavior of the plastics itself. The near-barrier behavior of plastic debris is important to assess functional performance of the PCS. Near-barrier behavior of plastic is not within the scope of this thesis. Overtopping volumes will be quantified, which can be used in a future plastic loss assessment.

2.7 OVERVIEW OF THE APPROACH

The thesis work will be divided into three parts:

PART I – 2D (HYDRO-) DYNAMIC BEHAVIOR OF A 2D CYLINDER WITH A SPRING ATTACHED

Part one considers a 2D cross-section of the barrier in an ideal fluid. It is assumed that its hydrodynamic response to wave forcing is linear or can be linearized. These assumptions allow the 2D barrier response to be described using linearized 2D potential theory. The software package OCTOPUS-Office (commercial successor of SEAWAY) is used to determine the 2D hydrodynamic coefficients. A 2D equivalent spring stiffness is calculated with the use of a beam element model. In this way, the effect of barriers bending stiffness is accounted for. Matlab is

then used to determine the frequency domain and time domain response of a 2D cross-section of the floater.

PART II – ASSESMENT OF THE AMBIENT WAVE FIELD AND DETERMINATION OF THE EQUIVALENT STIFFNESS COEFFICIENT

Part II analyses the wave environment surrounding the PCS. A method to derive the crest length of incoming waves is developed and statistics are derived. Based on the spatial size of the ambient waves, equivalent spring stiffness coefficients are derived to incorporate the approximate bending behavior of the structure.

PART III – WAVE OVERTOPPING ASSESMENT BASED ON A COUPLED HYDRODYNAMIC-CFD ANALYSIS

An overtopping assessment based on a coupled hydrodynamic-CFD analysis is performed along the barrier system. A motion time trace is derived from a hydrodynamic model and imposed into a 2D CFD model set-up in the CFD code ComFLOW. Via this method, 2D overtopping statistics are related to the wave and motion of the barrier. The overtopping statistics derived from this model are then related to overtopping events occurring along the barrier.

3 System & surroundings

3.1 COORDINATE SYSTEMS

The coordinate systems used are defined in Figure 4. An earth fixed coordinate system (XYZ) and a steadily translating coordinate system (xyz) are defined. The translating axis system is defined such, that it moves with the steady state speed of the barrier V_{mean} induced by current and wind action. Motions due to wave action is then depicted as oscillations around this steadily translating coordinate system. The origin of the steady translating system is located at the center point of the floater, halfway the length of the barrier.

3.2 SYSTEMS MAIN CHARACTERISTICS AND PROPERTIES

The plastic capturing system essentially is a barrier consisting of three parts: a floater, a skirt and a ballast weight. The floater's functions are to maintain the system's structural integrity, follow the sea surface elevation and (of course) to keep the system afloat. The skirt's function is to retain plastic behind the barrier and the ballast weight is attached to the screen to counteract its buoyancy and ensure enough draft under oceanic conditions.

Figure 7 shows a top view of the floating barrier in the X-Y plane. L is the total length of the floater. Due to tensioning, current, wave and wind action the floater takes the shape of an arc. During this research project, the arc and therefore the length between the end points of the floater, effective length L_e, is assumed to be fixed.

Figure 6 shows a cross-section of the barrier in the Z-X plane. The geometrical freeboard f of the floater is the above water clearance when resting in still water. The geometrical draft of the floater T_f defines how far the floater is immersed when resting in still water. Summation of the floater geometrical draft T_f and the skirt length L_s gives the geometrical draft of the system T_s (system immersion at rest). Table 1 shows an overview of the systems main characteristics and properties.

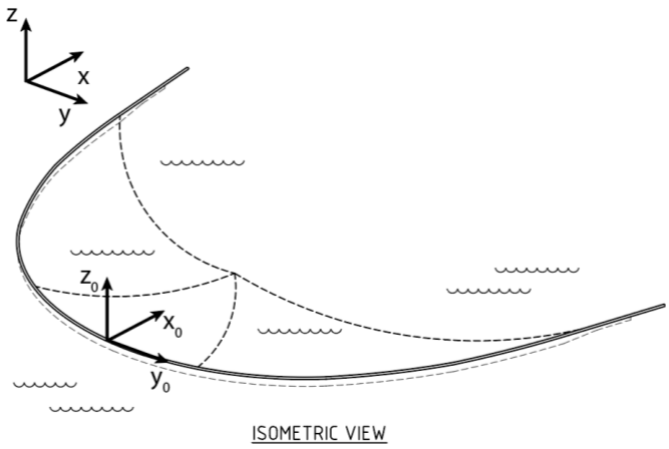

Figure 4 Isometric view of the barrier defining coordinate system used. (Image courtesy of The Ocean Cleanup)

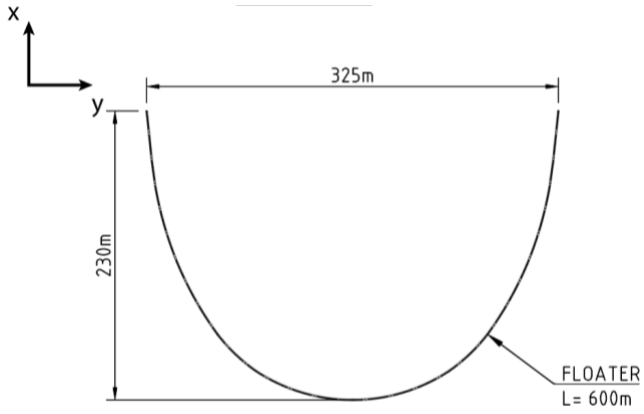

Figure 5 Top view of the barrier defining its main dimensions in the X-Y plane. (Image courtesy of The Ocean Cleanup)

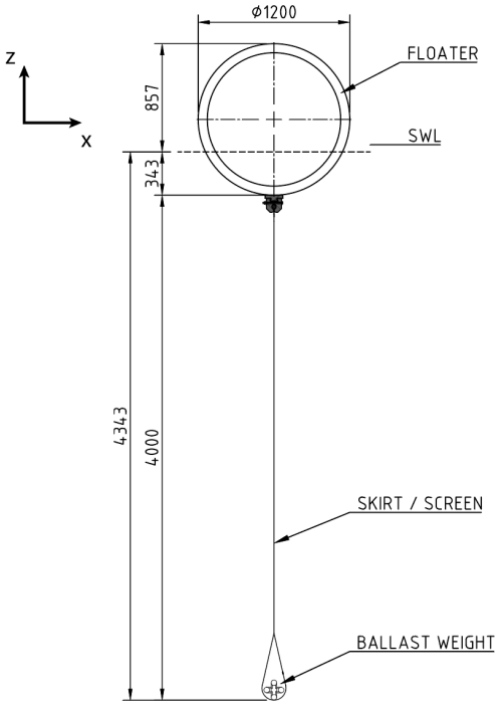

Figure 6 Cross-section of the barrier defining its main dimensions [mm] in the Z-X plane. (Image courtesy of The Ocean Cleanup)

3.3 SYSTEM CONVENTIONS

Figure 7 shows a cross-sectional view of the barrier in the Z-X Plane. Relative freeboard is defined as the sum of the geometrical free board and the relative vertical motion of the structure:

$$f_r(t) = f + s_p(t) \quad (1)$$

Interactions of the system with waves induce a heave motion of the floating barrier. The relative vertical motion s_p with respect to the undisturbed wave surface at point P is defined as the difference between local heave motion and the local wave elevation [19]:

$$s_p(t) = h_p(t) - \zeta_p(t) \quad (2)$$

3.4 ENVIRONMENTAL CONDITIONS

It is important to know the environmental conditions encountered by the PCS to assess its operational performance. The system is located in the 'splash-zone' and will be subject to current, wind and wave action. This thesis study only takes the effect of (surface gravity) waves on overtopping into account, any coupled effects of wind and current action are neglected. The PCS's will first be deployed in the GPGP. Figure 8 maps the 10-year-averaged distribution of plastic particles within the GPGP which was calculated from a model developed during an intensive three-year research project performed by TOC [6]. Bright yellow indicates the denser center region. A Met-ocean study [20] performed by Metocean Solution Ltd by order of TOC provides data of the wave conditions encountered for the location 30°N, 138°W, about 1000 nautical miles east of Los Angeles. This data will be used for the definition of environmental parameters. For each of the defined environmental parameter configurations, wave overtopping is then evaluated.

A wave rose plot indicating the dominant direction of waves is shown in Figure 9. This figure shows that mean annual wave direction is from the North-West. Scatter plots are found in Appendix A. Wave scatter plots are given for the full wave energy spectrum and for the wind wave energy spectrum respectively. In these scatter plots T_p is defined as the peak period, or the wave period with the highest energy in the wave spectrum. H_s is known as the significant wave height, or the mean of the highest one-third of waves in the wave record [21]:

$$H_s = H_{1/3} = \frac{1}{N/3}\sum_{j=1}^{N/3} H_j \quad (3)$$

I n which N is the number of wave occurrences and H_j the rank number of the wave based its wave height (e.g. $J = 1$ corresponding with the highest wave).

Table 2 shows extreme value wave conditions for the 10-year return period.

3.4.1 Wave theories

Several theories have been developed to describe the propagation of surface gravity waves over time and space. Theories handled here are based on the assumption of waves

Property	Symbol	Value	Unit
Floater length	L	600	[m]
Floater effective length	L_e	325	[m]
Floater outer diameter	D_o	1200	[mm]
Floater geometrical freeboard	f	800	[mm]
Floater geometrical draft	T_f	343	[mm]
Skirt length	L_s	4000	[mm]
Total geometrical draft system	T	4343	[mm]
Total unit dry weight system	M_{dry}	262	[kg/m]
Bending stiffness floater	EI	39000	[KNm^2]

Table 1 Systems main characteristics and properties

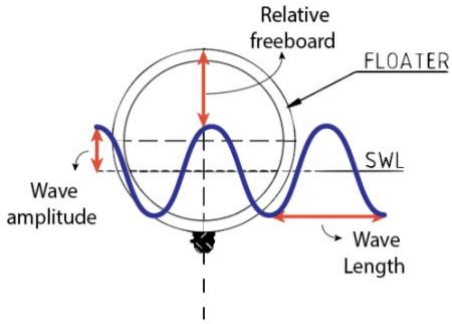

Figure 7 – Schematic convention drawings of the system. Cross sectional view: defining its main conventions. (Image courtesy of The Ocean Cleanup)

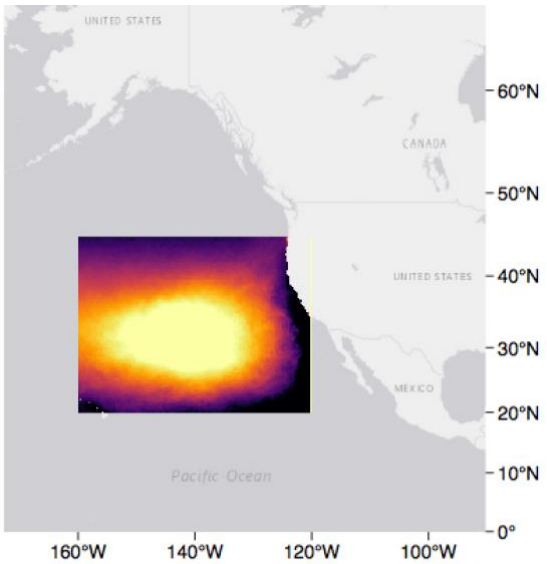

Figure 8 Distribution of plastic density in garbage patch averaged over 10 years. Based on data from models developed within TOC. Bright yellow corresponds to a high density of plastic particles. Dark purple corresponds to a low density of plastic particles. Map generated using QGIS. (Image courtesy of The Ocean Cleanup)

being periodic and uniform. This enables the application of harmonic functions in describing surface gravity waves. The validity range of a wave theory depends upon environmental parameters such as depth, wave height and period [22]. For shallow depth, as well as the combination of wave height and period (or wavelength), non-linearity's may be introduced and an adequate wave theory should be applied. Figure 10 summarizes the validity range of wave theories based on the shallow water parameter and wave steepness parameter. The shallow water parameter determines whether presence of the seabed affects water particle motion. It is defined as [23]:

$$\mu = 2\pi * \frac{d}{gT^2} = \frac{d}{\lambda} \quad (4)$$

In the vicinity of the garbage patch, the oceans are so deep, $\lambda \ll d$, that the wave-induced orbital motion of the water particles is unaffected by the seabed. As a result, deep water conditions may be considered [21]. Such waters are also known as 'oceanic waters'. Waves in oceanic waters may be assumed to behave linearly when they meet the small amplitude approximation: wave amplitudes are small compared to their wave lengths. When wave amplitudes grow too large compared to their wave lengths, the surface slope of the wave becomes too large and non-linearity's are introduced. In this case, the small amplitude approximation does not hold anymore and one should resort to a wave theory which takes non-linear effects into account. The surface slope of a wave is classified in terms of wave steepness, defined by [23]:

$$S = 2\pi * \frac{H}{gT^2} = \frac{H}{\lambda} \quad (5)$$

When waves grow too steep, they break according to the breaking criterion (for deep water) [21]:

$$\frac{H}{\lambda} = 0.142 \quad (6)$$

In the previous functions (eq. 4-6), H is the wave height, T the wave period, d the depth, λ the wavelength and g the gravitational acceleration.

3.4.2 Linear wave theory

Linear wave theory, also known as the Airy wave theory, is the most basic one in the known wave theories. It is a first order regular wave theory, describing waves as a harmonic (co)-sine function with amplitude, frequency, wavenumber and phase.
For a regular wave, the free surface elevation is described in the form of a propagating wave:

$$\eta(x,t) = \eta_a \cos(\omega t - kx + \varphi) \quad (7)$$

The fluid motions are then described by the following velocity potential function:

$$\phi = \widehat{\phi} \sin(\omega t - kx + \varphi) \quad (8)$$

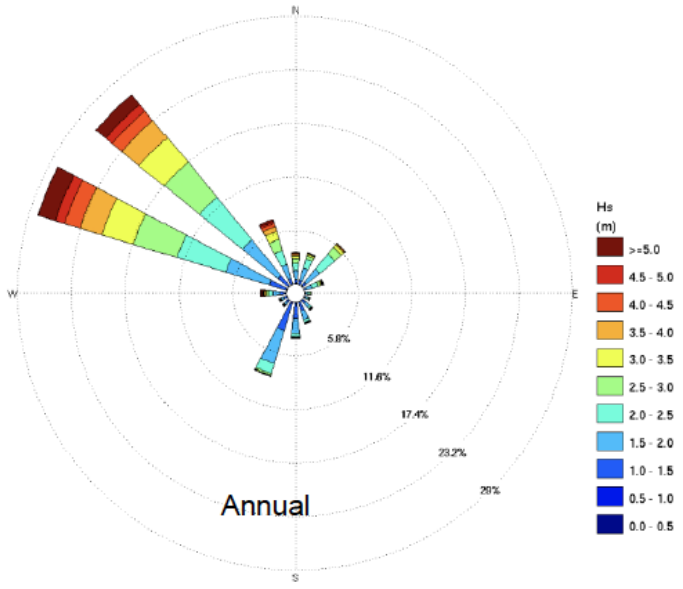

Figure 9 Wave rose plot showing annual wave direction for the location 30°N, 138°W (image taken from [20])

10 year return period	Symbol	Value	Unit
Significant wave height	H_s	11.03	[m]
Peak period	T_p	19.41	[s]

Table 2 extreme value wave conditions for the 10-year return period [20]

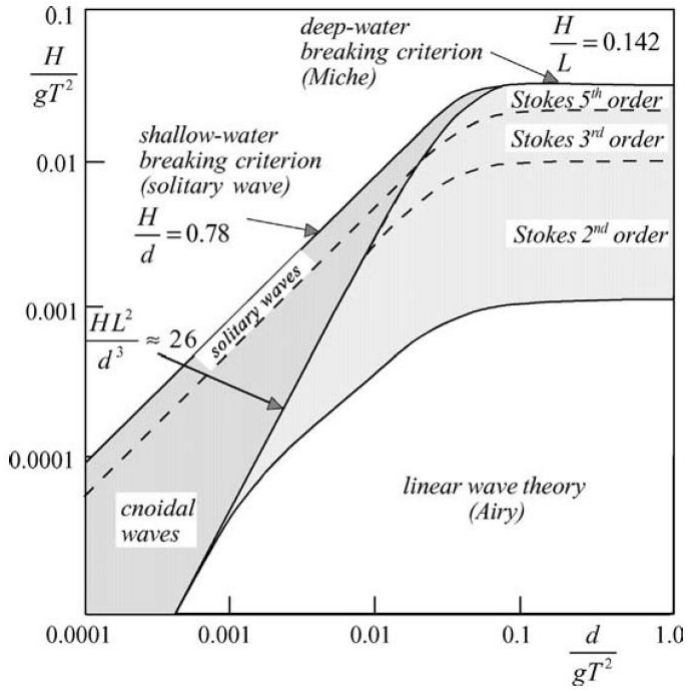

Figure 10 Applicability range of several wave theories. (Figure taken from [21])

With:

$$\hat{\phi} = \frac{\eta_a g}{\omega} \frac{\cosh[k(d+z)]}{\sinh(kd)} \quad (9)$$

These harmonic wave functions are derived from the Laplace equation and kinematic boundary conditions. The derivation leading to these solutions can be found in [21].

The linearized Bernoulli equation is defined as [21]:

$$\frac{\partial \phi}{\partial t} + \frac{p}{\rho} + gz = 0 \quad (10)$$

Substitution of the velocity potential gives:

$$p = -\rho g z + \rho g a \frac{\cosh[k(d+z)]}{\sinh(kd)} \sin(\omega t - kx + \varphi) \quad (11)$$

The second term of equation 11 is the wave-induced pressure:

$$p_{wave} = \rho g a \frac{\cosh[k(d+z)]}{\sinh(kd)} \sin(\omega t - kx + \varphi) \quad (12)$$

The velocity field is derived by taking the gradient of the velocity potential function described in equation 8. The water particle velocities and accelerations read:

$$u = \omega \eta_a \frac{\cosh[k(d+z)]}{\sinh(kd)} \cos(\omega t - kx + \varphi) \quad (13)$$

$$w = \omega \eta_a \frac{\sinh[k(d+z)]}{\sinh(kd)} \sin(\omega t - kx + \varphi) \quad (14)$$

$$\dot{u} = \omega \eta_a \frac{\cosh[k(d+z)]}{\sinh(kd)} \sin(\omega t - kx + \varphi) \quad (15)$$

$$\dot{w} = -\omega^2 \eta_a \frac{\sinh[k(d+z)]}{\sinh(kd)} \cos(\omega t - kx + \varphi) \quad (16)$$

The dispersion relationship for surface gravity waves reads [20]:

$$\omega^2 = gk \tanh(kd) \quad (17)$$

$$\lambda = \frac{g}{2\pi} T^2 \tanh \frac{2\pi d}{\lambda} \quad (18)$$

For deep water ($\tanh(kd) \approx 1$) the dispersion relationship approaches:

$$\omega^2 \approx gk \quad (19)$$

$$\lambda \approx \frac{g}{2\pi} T^2 \quad (20)$$

The relationship between wave period and frequency is:

$$T = \frac{2\pi}{\omega} \quad (21)$$

Using the dispersion relationship, the wave celerity $c = \frac{\lambda}{T} = \frac{\omega}{k}$ is derived:

$$c = \sqrt{\frac{g}{k} \tanh(kd)} \quad (22)$$

In the previous functions (eq. 7-22), η_a is the wave amplitude, k the wave number, φ the phase, ω the wave frequency, d the depth, p the pressure, ρ the density, λ the wavelength, T the wave period and g the gravitational acceleration.

3.4.3 Description of an irregular wave system

Under the assumption of linearity, it is possible to reconstruct an irregular wave from the summation of individual small linear wave components with different amplitudes [24]. This method is practiced in the random/phase amplitude model for random waves. The random phase/amplitude model is the simplest and most applied model in simulation of irregular sea states [21,23]. It describes the sea surface elevation as a zero-mean Gaussian stochastic process, representing the free surface elevation as a summation of independent harmonic wave components. Amplitudes are Rayleigh distributed and phases uniformly distributed. The one-dimensional random phase/amplitude model is defined as:

$$\underline{\eta}(t) = \sum_{i=1}^{N} \underline{a}_i \cos\left(\omega_i t + \underline{\varphi}_i\right) \quad (23)$$

By extending the random phase/amplitude model to the x and y-space, while accounting for wave directionality, a wave field is defined as follows:

$$\eta(x,y,t) = \sum_{i=1}^{N} \sum_{j=1}^{M} a_{i,j} \cos\left(\omega_i t - k_i x \cos\theta_i - k_j y \cos\theta_j + \varphi_{i,j}\right) \quad (24)$$

A random sea surface can now be constructed with the use of a given frequency-direction spectrum.

3.4.4 Wave spectrum

For a given sea state, a wave spectrum gives the spectral distribution of the wave energy. As the system is wind vaning [25], wind waves will often travel perpendicular to the barrier and are of special interest. This is explained further in part I. The spectra will be composed from the wind wave scatter plots given in Appendix A. The environmental variables H_s and T_p will be used to express the wave spectrum. This will be done by using the Jonswap [26] spectrum, while taking $\gamma^A = 1.522$:

$$S_\eta(\omega) = \frac{320 H_s^2}{T_p^4} \omega^{-5} e^{\frac{-1950}{T_p^4}\omega^{-4}} \gamma^A \quad (25)$$

The wave amplitude a_i used in the random phase/amplitude model is determined from the spectrum as follows:

$$a_i = \sqrt{2 S_\eta(\omega_i) \Delta\omega_i} \quad (26)$$

Geometric progression is applied to prevent repetition of the incoming wave pattern [26]. Accounting for wave directionality, the directional spectrum is defined as:

$$S_\eta(\omega,\theta) = S_\eta(\omega)D(\theta) \tag{27}$$

Using a cos^{2s} model [21] for the directional distribution $D(\theta)$. By definition, the following must hold:

$$\int_{\theta=0}^{2\pi} D(\theta)\, d\theta = 1 \tag{28}$$

4 Reading Guide

The main matter section provides an introduction to this thesis work. Here, the research problem is analyzed and a research plan presented. Also, the properties and characteristics of the system and its surroundings are analyzed.

Part I, II and III of this thesis are written (roughly) according to the article format. The purpose of this is that these parts can be read on an individual basis. These parts include their own abstract, introduction, main part, discussion and conclusion. Part I describes the local dynamic behavior of the PCS. Part II covers an assessment of the ambient wave field and provides a coefficient to include an equivalent spring stiffness into the model from Part I. Part III concerns the coupling of the hydrodynamic model to the CFD solver ComFLOW. Finally, wave overtopping statistics are derived from simulations in a 2D numerical wave tank with imposed motion.

A shared nomenclature is found in front of the main matter section. A shared reference list is found after Part III, followed by the appendix section.

PART I – (HYDRO-)DYNAMIC BEHAVIOR OF A 2D CYLINDER WITH A SPRING ATTACHED

Part I (Hydro-)Dynamic behaviour of a 2D cylinder with springs attached

Keywords

2D hydrodynamics, 2D equivalent spring stiffness, Wave Induced Response, Frequency Response Characteristics, Time Domain Motion Response

Abstract

In order to understand the development of wave overtopping, the hydrodynamic behavior of the system needs to be studied first. A hydrodynamic model is designed to model the first order motion response to wave excitation of a 2D cylinder with springs attached. Derivation of the spring constants is based on the ambient three-dimensional wave field. It is proposed that this model approximates the motions of a 2D cross-section of a long flexible cylinder subject to random wave excitation. Individual components of the model, as well as the model itself, are evaluated through verification, validation and/or comparison with existing models. The hydrodynamic model is the first part in a proposed method for the investigation of wave overtopping over a floating barrier system. The model allows for coupling to a 2D CFD solver. The 2D CFD model with imposed motion can then be used to analyze local effects of wave overtopping. It has been shown that the ability of the 2D cylinder to follow waves is extremely sensitive to the equivalent spring stiffness introduced in the model.

1 Introduction

In the understanding of wave overtopping phenomena, it is crucial to determine the dynamic response of the considered system. The relative motion of the structure to the water particles determines the severity of an overtopping event. In order to focus on overtopping phenomena, only the floater part is modelled. This part looks into the response of a circular flexible floater to waves. For a flexible system, the response is not only dependent on hydrodynamic behavior, the structural response should also be taken into account. The floater is modelled as a flexible semi-submerged cylinder. The floater is assumed to be long with respect to its diameter. The 2D hydrodynamic effects in the cross-sectional plane are expected to be governing for the hydrodynamic behavior of the barrier. Therefore, the hydrodynamic problem is reduced to a moving cylinder in the cross-sectional plane. The structural response is captured using a 2D equivalent spring stiffness model. Only the (uncoupled) effect of heave and surge motions is looked into.

2 Outline

Theory of wave forcing on structures will be handled first. Then a model for wave-induced motions of a flexible cylinder is derived. Model implementation and case-specific input data are presented. After this, model outputs are discussed. Results in the form of wave induced motions are presented. Next, the model will be evaluated. Thereafter, the approach taken and results are discussed. Finally, part I is concluded.

3 Formulation of hydrodynamic model

3.1 FORMULATION OF HYDRODYNAMIC WAVE FORCING ON A 2D CYLINDER

Wave forcing on cylindrical structures has been a topic under extensive research over the past century. In literature, two types of approaches are found. The first one is a theoretical derivation based on potential flow theory. The second one is an empirical derivation based on experimental results, also known as the Morison approach. The basis and grounds of these theories are limited to the physical geometry of the structure compared to the dimensions of the wave field.

3.1.1 Choice of hydrodynamic theory

The region of applicability of wave forcing theories depends on the encountered wave field and the geometry of the structure. The dimensions of the wave field are characterized by the wavelength and wave height. The structure, a cylinder, is characterized by its geometry and surface roughness. When performing hydrodynamic research, the choice of approach is often based on a dimensionless analysis. Using dimensionless analysis, parameters are derived that determine what phenomena have to be taken in to account and which theory should be considered [22]. Figure 11 shows a graph taken from DNV recommended practice [24] and determined by Chakrabarti [22]. The applicability regions of wave force theories can be determined based on this graph using the diffraction parameter and the KC-number related H/D ratio.

The diffraction parameter gives an indication whether the presence of a structure in waves may alter the surrounding pressure field due to diffraction of waves. The severity of diffraction effects depend on the characteristic dimension D of the structure versus wave length λ. The diffraction parameter is defined as:

$$Diffraction\ parameter = \frac{\pi D}{\lambda} \qquad (29)$$

When a cylinder is placed in a fluid flow, the importance of drag effects should be considered. For cylinders in an oscillatory flow, the Keulegan-Carpenter number is defined. This parameter gives the importance of drag effects compared to inertia effects. For small KC-numbers (~ <5), the inertia forces are dominant over drag forces, when the KC-number is large (~ >40), drag forces are found to be dominant [27]. When considering linear deep-water theory:

$$KC = \frac{\pi H}{D} \qquad (30)$$

Considering Figure 11 and the wave environment determined in chapter 3.4 and Appendix A, it can be concluded that the system will mainly operate in region III and partly in V during day-to-day conditions. Under extreme wave conditions, the system will operate in region V only. From the equation for the KC-number it is seen that drag forces have increasing importance for higher waves. In low/moderate conditions, inertia forces are governing. In high seas, drag effects become more and more important. Extreme seas are not taken into account as the system will be in survivability mode, rather than operational mode.

From Figure 11, it may be concluded that the usage of potential theory is stretching the limits of its applicability in some of the handled environmental cases. However, as a first approach to the motion behavior of the boom, this thesis research does apply potential theory to develop a model approximating the motion response of the structure to wave excitation.

Note that, as an extra, a derivation of Morison's theory applied on a horizontal cylinder is handled in appendix B. It will not be applied in this thesis research however.

3.1.2 Potential flow theory

Potential flow theory is used to describe the velocity field for irrotational flow of an idealized fluid. In 1949, Ursell [28] made a first contribution to the solution of fluid motion around a cylinder using linear potential theory. He proposed that the fluid flow around a heaving cylinder in still water can be described by a superposition of potential functions. Now, by conforming to the boundary conditions stated in Appendix C, it is possible to derive an analytical solution of the velocity potential for a partially submerged circular cross-section heaving in the 2-dimensional plane:

$$\phi(x,z,t) = \phi(x,z)e^{-i\omega t} \tag{31}$$

The hydrodynamic pressure acting on a certain point in the fluid is given by the linearized Bernoulli equation (see also eq. 10-12):

$$p = -\rho\frac{\partial\phi}{\partial t} \tag{32}$$

Where ρ represents the mass density of the surrounding fluid. The hydrodynamic force acting on the cylinder is found by integrating the pressure over the wetted cylinder surface. The resulting hydrodynamic force can be decomposed in a term in-phase with the acceleration and a term in-phase with the velocity of the cylinder. After evaluation of the terms, the hydrodynamic reaction force is rewritten in the following form:

$$F_{hydrodynamic} = -a_{33}(\omega)\ddot{z} - b_{33}(\omega)\dot{z} \tag{33}$$
(for heave)

$\ddot{z}$ is defined as the heave acceleration, $\dot{z}$ the heave velocity. The acceleration component $a_{33}(\omega)\ddot{z}$ is the result of acceleration of surrounding fluid and does not dissipate energy. When a body surrounded by a fluid is accelerated, a particular volume of fluid surrounding the body is (in some degree) accelerated with the body. This results in a hydro-mechanic force and the frequency-dependent mass $a_{33}(\omega)$ of this volume can be seen as an 'added mass' accelerated with the body. The velocity component $b_{33}(\omega)\dot{z}$ does dissipate energy. When a body surrounded by a fluid is moving, it generates radiating waves. The radiation of these waves dissipate energy, resulting in a damping force. This term is known as the hydrodynamic damping term with frequency-dependent damping coefficient $b_{33}(\omega)$. When the cylinder is displaced in heave, its buoyancy is changed. This introduces a reaction force due to hydrostatics:

$$F_{hydrostatic} = -c_{33}z \tag{34}$$
(for heave)

The hydrostatic force $c_{33}z$ can be seen as a restoring spring term with heave displacement z and hydrostatic spring coefficient:

$$c_{33} = \rho g S_{wl} \tag{35}$$

With gravity acceleration constant g and water plane area of the body S_{wl}.

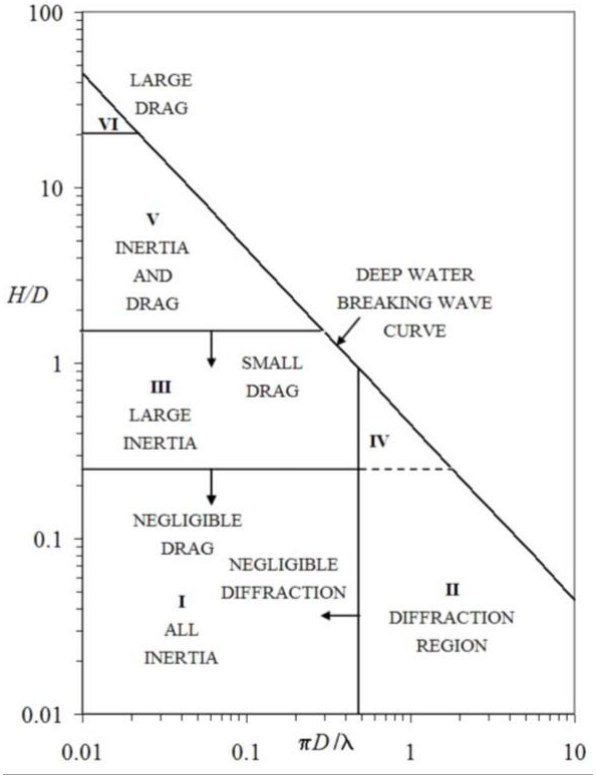

Figure 11 applicability regions of wave theories, (graph taken from [22] and [24]).

To calculate wave exciting forces, Froude-Krylov assumed that the presence of the geometry did not influence the pressure field of the wave. Integration of the pressure field over the wetted cylinder surface gives the undisturbed wave exciting force, known as the Froude-Krylov force. The total wave exciting force is calculated by adding a corrective diffraction term:

$$F_{wave\ excting} = F_{FK} + F_D \tag{36}$$
(for heave)

Now, the linearized and uncoupled equation of motion (EOM) for a 2D cylinder in heave direction is determined from newton's second law:

$$m\ddot{z} = \sum F \tag{37}$$
(for heave)

Substitution of equation 33, 34 and 36 results in:

$$\big(m + a_{33}(\omega)\big)\ddot{z} + b_{33}(\omega)\dot{z} + c_{33}z = F_{FK} + F_D \tag{38}$$
(for heave)

The motion of the barrier cross-section in heave is now modelled as a linear mass-spring-dashpot system. Taking coordinate x is zero at the location of the barrier; displacement, velocity and acceleration due to excitation by a regular wave, see eq. 7, are then written as:

$$z(t) = z_a\cos\left(\omega t - \varphi_{z,\eta}\right) \tag{39}$$

$$\dot{z}(t) = \omega z_a\sin\left(\omega t - \varphi_{z,\eta}\right) \tag{40}$$

$$\ddot{z}(t) = -\omega^2 z_a\cos\left(\omega t - \varphi_{z,\eta}\right) \tag{41}$$
(for heave)

Where z_a the heave amplitude and $\varphi_{z,\eta}$ the phase shift between the free surface elevation and the response of the cylinder.
Rewriting equations 7, 39, 40 and 41 in complex notation and substitution into equation 38 gives the EOM in complex form. With some reshuffling and rewriting of terms:

$$\left[-\omega^2\left(m + a_{33}(\omega)\right) + i\omega b_{33} + c_{33}\right]\hat{z}_a = F_{FK} + F_D \quad (42)$$

By rewriting the terms, the heave amplitude $\hat{z}_a$ is related to the wave exciting force $F_{FK}(\omega)$ and the free surface elevation profile η:

$$RAO_{z,\eta} = \frac{\hat{z}_a}{\hat{\eta}} = \frac{F_{FK} + F_D}{-\omega^2\left(m + a_{33}(\omega)\right) + i\omega b_{33}(\omega) + c_{33}} \quad (43)$$

This transfer function is known as the motion response operator (RAO).
The phase shift of the response with respect to the exciting wave force is written as:

$$\varepsilon_{z,\eta} = \tan^{-1}\frac{-m\omega^3 b_{33}(\omega)}{c_{33} - \omega^2\left(m + a_{33}(\omega)\right)} \quad (44)$$

With equations 43 and 44, the frequency characteristics of the cylinder in heave are determined. The energy response spectrum can now be determined as:

$$S_{z_a}(\omega) = S_\eta(\omega) * RAO^2_{z,\eta} \quad (45)$$

Calculation of the response in time-domain is based on the assumption of linearity. Considering the exciting wave as a superposition of independent harmonic wave components, the time domain response is the superposition of responses to these individual components:

$$z(t) = \sum_{i=1}^{N} \mathrm{a}_i \left|RAO_{z,\eta}(\omega_i)\right| cos\left[\omega_i t + \varphi_i + arg\left(RAO_{z,\eta}(\omega_i)\right)\right] \quad (46)$$

Considering equation 46, it is seen that the frequency dependent RAO and frequency dependent phase are used for calculation of the time domain response. Note that implementing this equation in a hydrodynamic model does not make it a true time-domain model, but it may be used to describe responses to sinusoidal excitations in the time domain, given that the hydrodynamic coefficients are evaluated at the frequencies of wave excitations and given that these coefficients are functions of wave frequency only [29-32].
A similar derivation can be made for the EOM in surge direction resulting in:

$$(m + a_{11})\ddot{x} + b_{11}\dot{x} = F_{FK} + F_D \quad (47)$$
(for surge)

With the following frequency characteristics:

$$RAO_{x,\eta} = \frac{\hat{x}_a}{\hat{\eta}} = \frac{F_{FK} + F_D}{-\omega^2\left(m + a_{11}(\omega)\right) + i\omega b_{11}(\omega)} \quad (48)$$

$$\varepsilon_{x,\eta} = \tan^{-1}\frac{-m\omega^3 b_{11}(\omega)}{-\omega^2\left(m + a_{11}(\omega)\right)} \quad (49)$$

And the energy response spectrum defined as:

$$S_{x_a}(\omega) = S_\eta(\omega) * RAO^2_{x,\eta} \quad (50)$$

Finally, the time domain response is written as:

$$x(t) = \sum_{i=1}^{N} \mathrm{a}_i \left|RAO_{x,\eta}(\omega_i)\right| cos\left[\omega_i t + \varphi_i + arg\left(RAO_{x,\eta}(\omega_i)\right)\right] \quad (51)$$

3.2 EXTENSION TO A FLEXIBLE FLOATER

The 2D linear potential flow problem previously described, can be used to approximately model the wave excitation response of a 2D cross section of the considered floater. Because the floater is flexible, any bending effects should be incorporated.
As seen in Figure 12, in a realistic sea-state, waves are not infinitely long crested. Wave components with different directions cause seas to have crests with limited lengths L_c. Load distribution along the barrier is not uniform and resistance against bending is expected to play a significant role in the motion behavior of the cylinder. A method is proposed to account for bending stiffness effects in a 2D hydrodynamic model. To make use of the two-dimensional model derived in section 3.2.1, the model should be extended with a term accounting for these bending effects. First, a few assumptions have to be made however:

- The system is wind vaning, therefore the wind waves are the most interesting, as they always travel perpendicular to the barrier
- Only the middle section of the floater is considered. In this region, the curvature of the barrier is small and assumed neglectable. This middle section is then simplified into a long flexible straight pipe. In heave, the problem of a flexible floater subject to non-uniform wave forcing is reduced into a simply supported beam subject to a distributed loading q, see Figure 13. The max deflection of the beam is [33]:

$$\delta_{max} = \frac{5qL_{spec}{}^4}{384EI} \quad (52)$$

with q the distributed load applied on the beam, L_{spec} the specific length of the beam and EI the bending stiffness. Note that both L_c and L_{spec} depend on the encountered wave field.

- Assuming the non-uniform load distribution along the barrier to be sinusoidal, the specific length of the beam can be expressed in terms of the crest length L_c:

$$L_{spec} = 2L_c \quad (53)$$

Now, a slice in the middle of the beam, indicated with red in Figure 13, is now modelled as a partially submerged cylinder

with a spring attached. Figure 14 depicts the 2D model used to approximate the motion response of the flexible floater to wave excitation. Effects of bending stiffness (in heave) in the 2D problem are now modeled by proposing an equivalent spring stiffness. Recalling Hooke's law [34], '*ut tensio, sic vis*', applied to a linear spring:

$$F = k_{spring}x \tag{54}$$

Giving:

$$k_{spring} = \frac{F}{x} \approx \frac{q * L_c}{\delta} = \frac{384EI * L_c}{5{L_{spec}}^4} \tag{55}$$

Expressing L_{spec} in terms of L_c, results in the following expression for the equivalent spring stiffness in heave:

$$k_{eq} = \frac{24EI}{5{L_c}^3} \tag{56}$$

See Figure 14, the two-dimensional hydrodynamic model is now extended with an equivalent spring stiffness in heave direction. The previously derived equations of motion now become:

$$\big(m + a_{33}(\omega)\big)\ddot{z} + b_{33}(\omega)\dot{z} + (c_{33} + k_{spring})z = F_{exciting} \tag{57}$$
(for heave)

$$\big(m + a_{11}(\omega)\big)\ddot{x} + b_{11}(\omega)\dot{x} = F_{exciting} \tag{58}$$
(for surge)

The RAO's for these EOM's are determined in the similar way as discussed in section 3.1.2. The equivalent stiffness incorporates effects due to three-dimensional bending in the two-dimensional model. The stiffness of this spring is based on the crest length L_c. This variable will be determined during the wave field assessment, which can be found in Part II of this thesis work.

3.3 NATURAL FREQUENCY AND DAMPING RATIO

The natural frequency ω_n is an important parameter in the assessment of motion behavior of a dynamic system. When a system is excited at its natural frequency, resonance phenomena occur, which may be driving the system to oscillate at large amplitudes of motions due to accumulation of energy. The undamped natural frequency is calculated as:

$$\omega_n = \sqrt{\frac{k}{m}} \tag{59}$$

In the case of the hydrodynamic model including equivalent spring stiffness, the formula is rewritten to:

$$\omega_n = \sqrt{\frac{c_{ii} + k_{spring}}{m + a_{ii}(\omega_n)}} \tag{60}$$

Natural frequency ω_n is found trough a process of iteration as added mass a is frequency dependent.

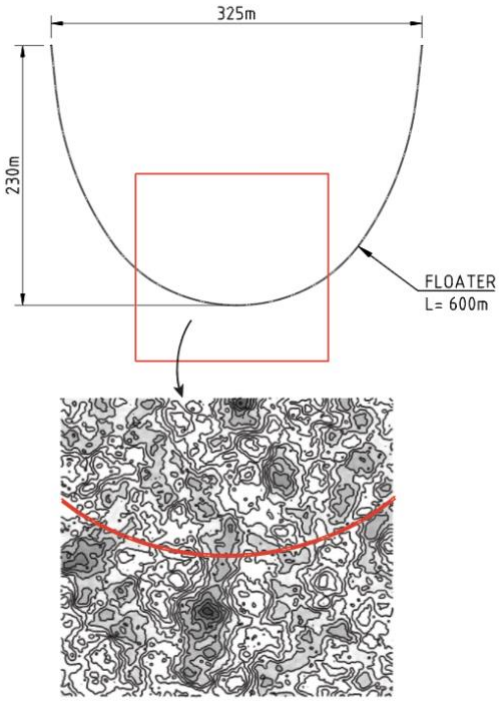

Figure 12 Contours of middle section barrier on sea surface elevation plot, grey areas are below SWL, white areas above SWL.

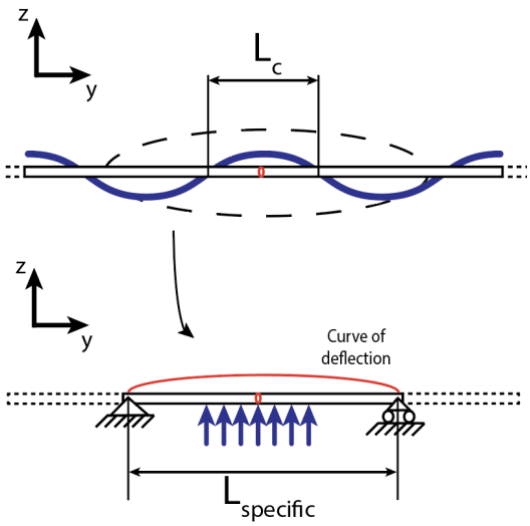

Figure 13 simplification of middle section floater to beam model

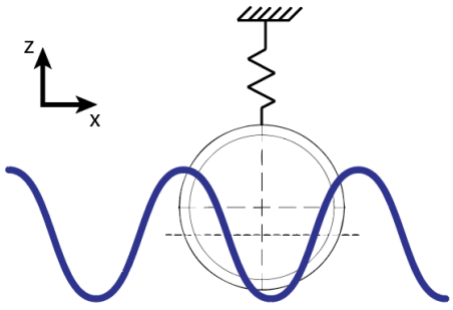

Figure 14 Two-dimensional model including equivalent spring stiffness

3.4 ENVIRONMENTAL MODEL

The free surface elevation is described using airy wave theory. A single regular wave traveling along the x-axis is defined as in equation 7:

$$\eta(x,t) = \eta_a \cos(\omega t - kx + \varphi)$$

Using equation 23, It is assumed that irregular waves can be represented as a summation of independent harmonic wave components:

$$\eta(t) = \sum_{i=1}^{N} \eta_i \cos(\omega_i t + \varphi_i)$$

Now, an irregular wave of interest is composed. Or, in the case of a random sea, the phase and amplitude are picked randomly, following the random phase/amplitude model.

4 Model implementation

A flow chart of the hydrodynamic model is depicted in Figure 15. Wave characteristics, geometry, and equivalent spring stiffness's are all defined using models designed in Matlab, these models are based on the previously handled theory. The geometry of the structure is drawn using the properties from Table 1 and formatted in a .hul-extension. Wave characteristics are calculated according to the environmental model described in section 3.4. The equivalent spring stiffness coefficients are calculated as described in section 3.2.

The geometry and equivalent spring stiffness's are used as an input for the software package OCTOPUS-Office. This program is used to perform a hydrodynamic analysis using potential flow theory, as described in section 3.1.2. Using the structures geometry as an input, the hydrostatic, added mass and hydrodynamic damping coefficients are obtained. After including the equivalent spring stiffness coefficients in the model, the frequency characteristics of the floater are calculated. Namely the frequency-dependent RAO and frequency dependent phase of the response.

The frequency characteristics are then implemented into the hydrodynamic model, which is designed in Matlab. This model calculates the response spectrum and time domain response according to equation 45, 46, 50 and 51 (with inclusion of the equivalent spring stiffness coefficient) as described in section 3.1.2 and 3.2.

5 Model output and visualization

OCTOPUS-Office calculates RAO's for frequencies from $\omega = 0$ to $\omega = 6$ rad/s. These are used by the hydrodynamic model to determine the frequency domain response and the time domain response.

In the frequency domain, the wave spectrum and corresponding response spectra are output and visualized. Figure 16 shows an example of the visualization of the wave and response spectra.

In the time domain, for every time step, the hydrodynamic model returns the free surface elevation and motions of the two-dimensional floater within the computational domain. The model also generates a (zoomed-in) movie of the floaters motion and the free surface elevation. Visualization of the floater motion in time domain is done to aid in the understanding of wave

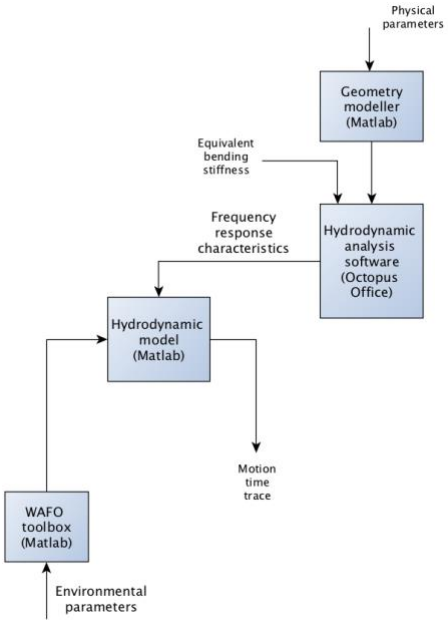

Figure 15 Flow chart hydrodynamic model

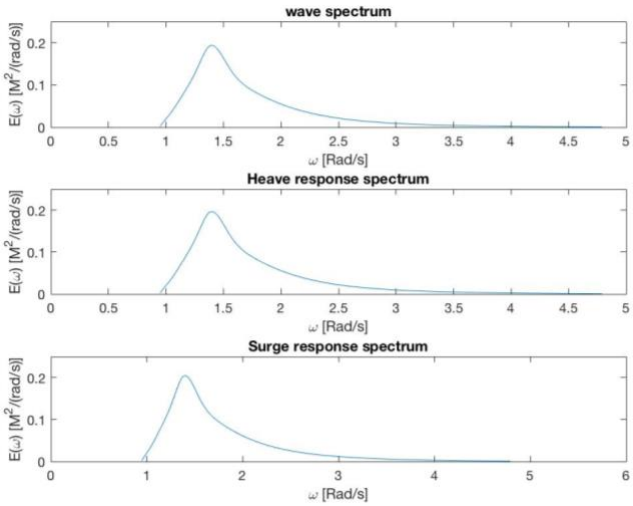

Figure 16 Example of wave and response spectra visualization

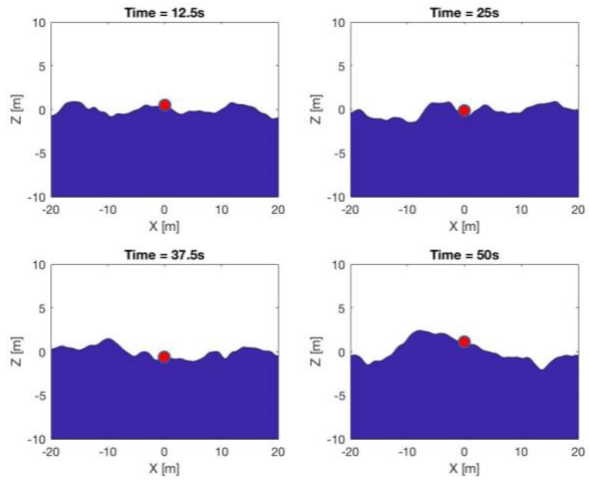

Figure 17 Example of floater motion visualization, shown are snapshots taken from the simulation.

overtopping. Figure 17 shows an example of the visualized floater motion and the free surface elevation in time domain.

6 Input data

6.1 PHYSICAL PROPERTIES OF FLOATER

The floater is modelled as a two-dimensional cylinder (circle) with physical properties found in Table 3.

6.1.1 Hydrostatic coefficient

The hydrostatic coefficient in heave c_{33} is calculated using OCTOPUS-Office and is found to be:

$$c_{33} = 10700 \frac{N}{m}$$

6.1.2 Added mass and damping

Added mass and hydrodynamic damping coefficients are calculated using the OCTOPUS-Office software package. The values of the obtained coefficients are found in Appendix D for heave and surge respectively.

6.1.3 Equivalent spring coefficient

The equivalent spring coefficient follows from equation 56, its value is dependent on the value of L_c, whose statistics are derived from the ambient wave field. This will be handled later on in this work (part II). Here, the equivalent stiffness coefficient will initially be chosen zero: A pure hydrodynamic model is assessed ($k_{eq} = 0$). Then, the sensitivity of the models' response to the equivalent spring stiffness is determined.

6.2 ENVIRONMENTAL TEST CASES

To maintain consistency, the same test conditions are chosen for all three parts. Although this part does not have an equivalent spring stiffness coefficient derived for a sea state yet, this coefficient is expected to be a governing parameter. From equation 56, it is seen that the equivalent spring stiffness will be inversely proportional to the encountered crest length to the third power. It is thus expected that, in short crested sea states, the floater will experience resistance in motion response due to bending stiffness effects. Therefore, the wind sea conditions given in Appendix A are looked into, as these conditions will result in short crested conditions. From the wind sea scatter plot a median, p90 and p99 H_s are chosen with a corresponding low T_p and most probable T_p. The low T_p will result in steeper conditions when compared to the most probable T_p with the same H_s. Table 4 gives the test cases chosen from the environmental conditions in Appendix A. The frequency cut-off value is the upper limit at which the considered wave spectrum will be truncated. The reason of this truncation will be explained further in part III, as it has to do with the boundary conditions of the applied model.

Property	Symbol	Value	Unit
Outer diameter floater	D_o	1200	[mm]
Geometrical freeboard floater	f	800	[mm]
Geometrical draft floater	T_f	343	[mm]
Unit dry weight system	M_t	262	[kg/m]
Bending stiffness floater	EI	39000	[KNm^2]

Table 3 Properties of floater

Irregular wave cases	Significant wave height H_s	Peak period T_p	Frequency cut-off	Characteristics
Case 1	1.5	4.5	5	Median H_s, low T_p
Case 2	1.5	6	5	Median H_s, most probable T_p
Case 3	3	6.5	4	P90 H_s, low T_p
Case 4	3	8	4	P90 H_s, most probable T_p
Case 5	6	9.5	3	P99 H_s, low T_p
Case 6	6	13	3	P99 H_s, most probable T_p

Table 4 Irregular wave cases

7 Results

7.1 FREQUENCY RESPONSE CHARACTERISTICS MODEL WITOUTH SPRING

RAO's and phase lags are calculated using OCTOPUS-Office, Figure 18 gives the frequency characteristics in the case of k_{eq} equal to zero. This is considered to be the 'pure hydrodynamic' model, no spring is attached. It is seen that for excitation frequencies

$$\omega < 5 \text{ rad/s}$$
$$RAO_{heave} \approx 1\ [m/m]$$
$$RAO_{surge} \approx 1\ to\ 1.2\ [m/m]$$

Above $5\ rad/s$, RAO_{heave} and RAO_{surge} decrease rapidly. Using equation 60, the natural frequency (heave) of the pure hydrodynamic model is calculated:

$$\omega_n = 4.3853\ rad/s$$

There is no significant amplification seen at natural frequency of the hydrodynamic model.

The wave spectra from Table 4 with corresponding response spectra, for a k_{spring}-value of 0, are given in appendix E. It is first observed that most of the energy of the wave spectra is contained in the $\omega < 2\ rad/s$ frequency region. The response spectra show that in the case of $k_{spring} = 0$, the heave and surge response spectra are (almost) equal to the wave spectrum. This is as expected, because for frequencies below $\omega < 2\ rad/s$ the floater $RAO_{heave} \approx RAO_{surge} \approx 1\ [m/m]$ as seen in Figure 18

7.2 SENSITIVITY TO EQUIVALENT STIFFNESS COEFFICIENT

Figure 19 shows the degradation in heave RAO for increasing equivalent spring stiffness. It is observed that for values of $k_{eq} > 10000\ N/m$, the amplitude of motion starts to be restricted significantly.

8 Evaluation of the model

8.1 VERIFICATION OF HYDROSTATIC COEFFICIENT

The hydrostatic coefficient c_{33} is calculated according to eq. 35:

$$c_{33} = \rho g S_{wl}$$

The water plane area S_{wl} defined in Figure 20, is calculated as follows:

$$S_{wl} = 2r\ sin\frac{\alpha}{2} \tag{61}$$

with:

$$\alpha = 2\ cos^{-1}\left(1 - \frac{T}{r}\right) \tag{62}$$

Filling in the floaters properties gives:

$$c_{33} = 10913\ \frac{N}{m}$$

8.2 VALIDATION OF ADDED MASS AND DAMPING COEFFICIENTS

Added mass and damping coefficients are obtained from the OCTOPUS-Office software package. This package has been under extensive validation during its development. Referred to is the work of Journee [35]. However, to check whether the input procedure of parameters is done correctly, a brief validation is made for the added mass and damping coefficients in heave. In literature, no added mass and damping coefficients were found for a circular cross section with the exact draft as used in this thesis. Therefore, the added mass and damping coefficient of a half-submerged cylinder are validated against available data from literature.

Figure 21 and Figure 22 give the non-dimensionalized added mass and non-dimensionalized hydrodynamic damping coefficients in heave for a half-submerged 2D cylinder. The results are obtained from the OCTOPUS-Office software package and compared with the theoretical solutions given by Porter [36] and Vugts' experimental values [37]. The values calculated by OCTOPUS-Office slightly overestimate the theoretical values, this might be explained by the numerical scheme used by OCTOPUS-Office. The differentiation of the experimental values with the theoretical values were explained by Vugts as experimental inaccuracies due to shallow water effects. The data from literature show good comparison with the results derived from OCTOPUS-Office. Together with the work done on validation by Journee, it is assumed that for a semi-submerged cylinder with a draft of 0.343 meter, use can be made of OCTOPUS-office to derive the frequency characteristics of the system.

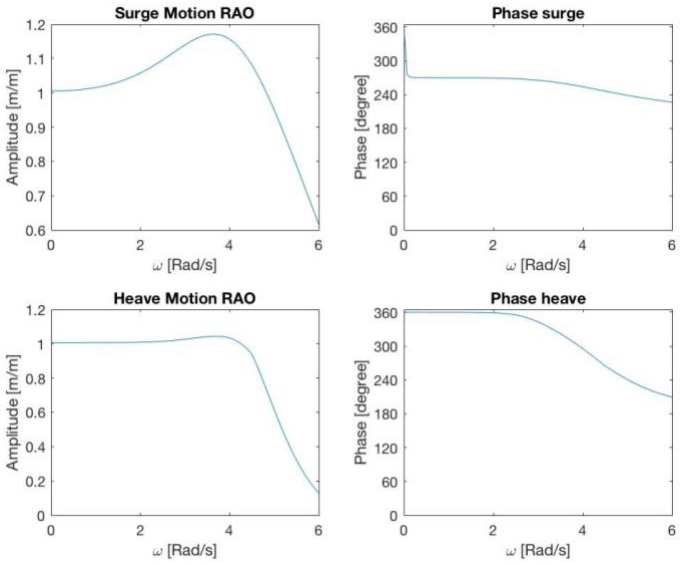

Figure 18 Frequency characteristics in heave and surge respectively for an equivalent spring stiffness of k = 0

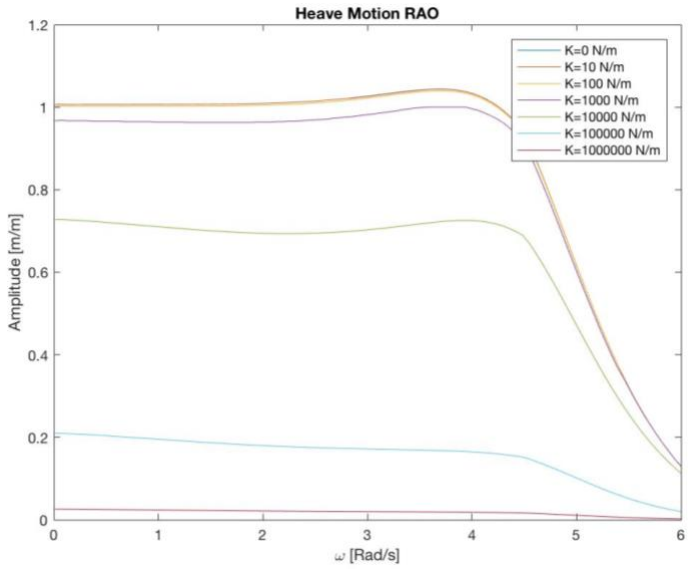

Figure 19 Degradation of Heave RAO for increasing values of k_{eq}

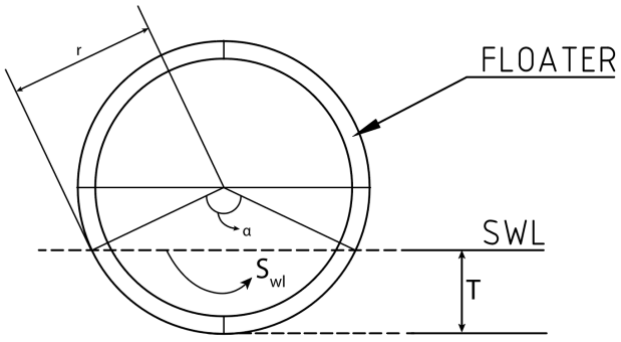

Figure 20 Definition of seawater line

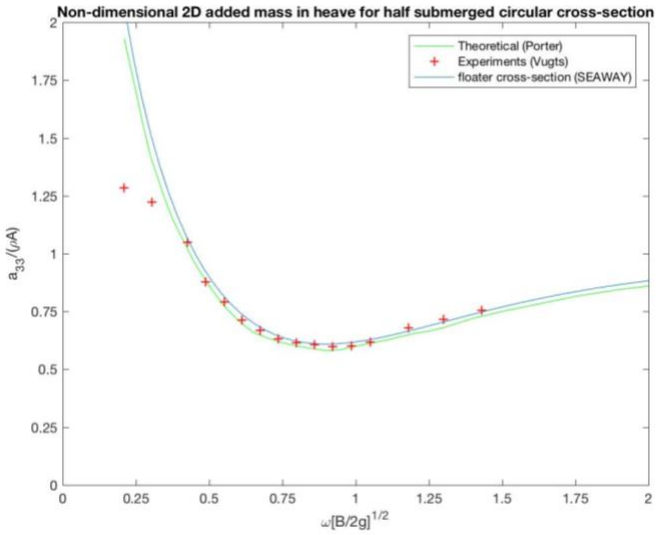

Figure 21 non-dimensionalized added mass in heave for a half-submerged circular cross-section. (Added mass a_{33} is non-dimensionlized by dividing through (ρA), in which A is the wetted surface area. Frequency ω is rescaled by multiplication of $\sqrt{B/2g}$ in which B is the beam of the floater)

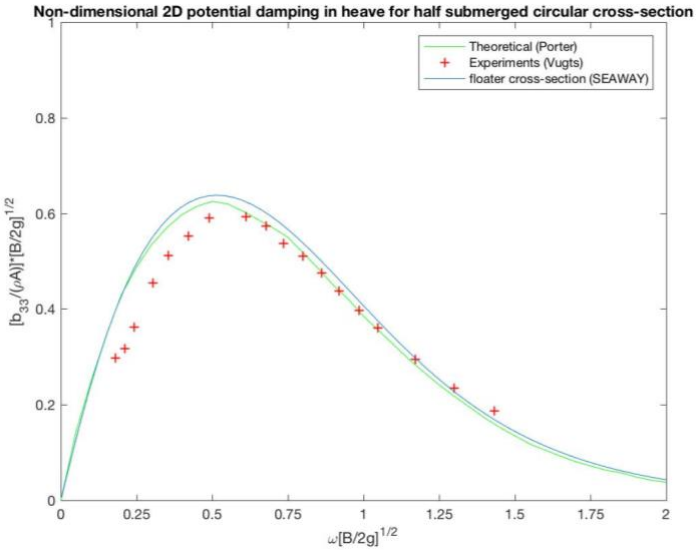

Figure 22 non-dimensionalized hydrodynamic damping in heave for a half-submerged circular cross-section. (Hydrodynamic damping b_{33} is non-dimensionlized by dividing through $[(\rho A)\sqrt{B/2g}]$. Frequency ω is rescaled by multiplication of $\sqrt{B/2g}$. A is the wetted surface area and B is the beam of the floater).

8.3 COMPARISON OF DEFLECTION OF BEAM MODEL WITH FEMAP MODEL

Recall equation 52 which determines the deflection of the beam model depicted in Figure 13:

$$\delta_{max} = \frac{5qL_{spec}{}^4}{384EI}$$

This equation was used to derive the formula of the equivalent spring coefficient. To check if deflections determined by equation 52 are right, the beam model is compared to a model designed in FEMAP. The software package FEMAP is used for structural analysis purposes.

To be able to compare the two models, a few parameters have to be defined first. The distributed load applied on the beam is approximated by only taking into account the Froude-Krylov force. The Froude-Krylov force is assumed to be linear and determined by integrating the pressure over the mean wetted hull surface:

$$F_{FK} = A * p \tag{63}$$

The distributed load is then calculated according to:

$$q = \frac{1}{2}\pi D * p \tag{64}$$

Assuming linear wave theory, the pressure is taken as the max of the wave induced pressure term in the Bernoulli equation, see eq. 10-12:

$$p = max[\rho g a \frac{\cosh[k(d+z)]}{\sinh(kd)} \sin(\omega t - kx + \varphi)] = \rho g a$$

The distributed load is then determined as:

$$q = \frac{1}{2}\pi D \rho g a \tag{65}$$

Properties used in this comparison study are found in Table 5, the max deflection, according to equation 52, is then calculated as:

$$\delta_{max} = 1.017\ [m]$$

Appendix F shows the model designed in FEMAP. The first figure shows the beam in its initial state, the second figure shows the beam in its deformed state. In the FEMAP model, the same constraints and distributed loading were applied. FEMAP determined the bending stiffness of the beam model about 15 percent higher than the one used in this thesis. The max deflection of the beam derived from the FEMAP model was calculated as:

$$\delta_{FEMAP} = 0.873\ [m]$$

The model in FEMAP shows a deviation of ~15% compared to results from equation 52. This explained by the higher bending stiffness applied in the FEMAP model. Taking this into account, it is found that both models show a satisfying comparison.

Property	Symbol	Value	Unit
Crest length	L_c	10	[m]
Specific length	L_{spec}	20	[m]
Bending stiffness floater	EI	39000	$[KN/m^2]$
Outer diameter floater	D_o	1200	[mm]

Inner diameter	D_i	1060	[mm]
Density	ρ	1030	$[kg/m^3]$
Distributed load	q	19046	[N/m]
Gravitational constant	g	9.81	$[m/s^2]$

Table 5 Properties used for deflection comparison study

8.4 COMPARISON OF HEAVE RESPONSE WITH ORCAFLEX

The hydrodynamic model ($k_{spring} = 0$) is compared with a model designed in OrcaFlex. OrcaFlex is a hydrodynamic modelling software package used by TOC to perform hydrodynamic calculations on the plastic capturing system. The properties used for this model are specified and verified by TOC. Figure 50 to Figure 55 in Appendix G show a comparison between the results calculated by the hydrodynamic model and the OrcaFlex comparison model for the considered test cases. The hydrodynamic model and OrcaFlex model compare very well for all of the environmental cases.

9 Discussion

9.1 REVIEW OF RESULTS

For the pure hydrodynamic model, the floater's heave and surge response spectra, found in Appendix E, are matching the wave spectrum very well. This was also expected as both the heave and surge RAO's are ≈1 for frequencies contained within the spectrum. The floater is expected to move typically like a 'sea gull', floating on the waves.

It is shown that introduction of bending stiffness to the model has a large effect on the relative motions of the barrier. Increasing bending stiffness leads to a reduced excitation response as seen in Figure 19.

9.2 REVIEW OF HYDRODYNAMIC THEORY

It is important to realize that calculation of the frequency- as well as the time domain response is based on linearization of the problem. Although the first order response of the structure usually provides the largest contribution to the total solution, higher-order effects can have a nonzero contribution to the hydrodynamic response of a structure. It should thus be emphasized that the first order motion, calculated here, only serves as a first approximation to the real hydrodynamic response of the structure in waves. Using linear potential theory, it is assumed that each wave component linearly induces a harmonic pressure on the structure and that individual components do not change the effect of one another. In reality however, waves can have non-linear profiles due to steepness and also the structure's response to a wave can be non-linear. Effects due to non-linear motion behavior on the total response is not looked into. It should be further noted that by applying potential theory, any effects due to drag forces are neglected. In section 3.1.1 it was already discussed that, serving as a first approach in developing a method, potential theory was applied to approximate the motion behavior of the considered structure. Any effects due to drag are thus not taken into account. From Figure 11 it was derived that, especially in high seas, drag may become of importance. The influence of these drag effects is not studied further and thus remain unknown. The OrcaFlex comparison model does apply the previously discussed Morison theory however. Morison's theory does account for drag effects. For all of the environmental cases that were considered, the hydrodynamic model and the OrcaFlex model fit each other very well. As the results from both models are similar, this gives indication that for both models the system's behavior is inertia dominated and any drag effects are small.

9.3 REVIEW OF APPROACH

In the research of the response of a floating barrier system, this work only considers the floater section. The addition of a screen, changes the characteristic dimension of the floater in surge direction significantly, while it stays the same in heave direction. When compared to the original model, the addition of a screen, should thus not give a large difference in heave frequency characteristics, while in surge a significant difference is expected. This statement could not be researched further as the OCTOPUS-Office software can't handle the addition of a thin screen to the floater section. Any effects of screen behavior on wave overtopping thus remain unknown.

The PCS is designed to accumulate plastic debris at the center part of the barrier. Effects due to overtopping will have the largest impact there. It is thus valid to focus on the middle section of the barrier, justifying the consideration made in paragraph 3.2.

The model considers a zero-forward speed, in reality the barrier moves passively with the ocean surface currents. A forward speed alters the encounter frequency of incoming waves. The forward speed of the barrier is [20]:

$$V_{barrier} \approx V_{meam\ ocean\ surface\ current} \approx 0.1\ m/s$$

For deep water, the 'frequency of encounter' is [19]:

$$\omega_e = \omega - \frac{\omega^2}{g} * v * cos\ \mu \qquad (66)$$

For higher frequencies, the difference in frequency of encounter ω_e and the wave frequency ω becomes larger. The highest wave frequency modelled is that of the cut-off frequency in case 1 and 2, $\omega = 5\ rad/s$. The frequency of encounter at this wave frequency and the considered $V_{barrier}$ is $\omega_e \approx 4.75\text{rad/s}$. The max difference in the modelled wave frequencies and the actual encounter frequencies then becomes:

$$\max(\omega - \omega_e) \approx 0.25\ rad/s$$

When regarding the modelled wave spectra, see Appendix E, it is observed that most of the energy lies in the region below <2 rad/s. Here, the difference in the modelled wave frequencies and the actual encounter frequencies become relatively small and it is thus safe to neglect the difference in frequency of encounter and the modelled wave frequencies.

A truncated domain of the wave spectra was used during the simulation of the environmental conditions, this is because of the frequency cut-off that has been set. It is expected that this does not lead to any consequences as most of the energy of the wave spectra was contained in the $\omega < 2\ rad/s$ frequency region, see appendix E.

To include the effects of bending behavior of the floater in the hydrodynamic model, without adding an extra layer of complexity, a tradeoff between simplicity and accuracy had to be made. In this work, choice was made for simplicity. The proposed method in which the effects due to bending resistance of a floater, excited by the ambient wave field, is captured in a constant value for a spring coefficient stiffness is a thus a simplified approximation to the real bending behavior of the floater.

10 Conclusions

A basic hydrodynamic model was developed to determine the 2D motion response of a floater. With implementation of an equivalent stiffness model, it is proposed that the model accounts for bending stiffness effects.

The derived motion behavior of the floater should be seen as a first approximation to the real motion behavior of a flexible floater subject to waves, because:

- Only linear hydrodynamic effects are taken into account.
- The bending stiffness model is a simplified model of the real bending behavior of a flexible floater
- Drag effects are neglected. In high seas, drag can be significant.

No significant amplification is seen at the natural frequency of the 'pure' hydrodynamic model. Resonant response in heave is neglectable.

From the sensitivity study, it is concluded that increased resistance against bending will have significant effects on the ability of the floater to follow waves.

Future research recommendations:

- Although all components of the model are evaluated, either by verification or comparison, the model is not validated by experiments. To further asses the quality of the results, a validation study is recommended.
- Inclusion of a (flexible) screen in the hydrodynamic model. It is expected that the screen has a significant effect on the motion behavior of the system.
- Study on effects of non-linearity
- Study on effects of drag forces
- Extension / Improvement of the bending stiffness model

PART II – ASSESSMENT OF THE AMBIENT WAVE FIELD AND DETERMINATION OF EQUIVALENT STIFFNESS COEFFICIENT

Part II – Assessment of the ambient wave field and determination of the equivalent spring coefficient

Keywords

Sea surface, Wave statistics, Wave Crest Length, Equivalent spring coefficient.

Abstract

From the previous part, it is observed that the presence of bending stiffness could resist the floater in its motion response. In turn, a reduced motion response can lead to increased overtopping. These findings emphasize that flexibility of the floater has to be taken into account when determining its motion response to wave excitation. A model to approximate bending effects into a linear spring is set up. The ambient 3D wave field surrounding the capturing system is modelled and wave statistics are derived. Based on these wave statistics, spring constants are derived for given physical and environmental configurations. From the results it is found that for the wave cases 1 to 4, the equivalent spring stiffness is significant enough to influence the motion response of the floater. For case 5 and 6 values for the equivalent spring stiffness are relatively low and its influence on the response is expected to be negligible.

1 Introduction

In part I, it was proposed that effects due to bending behavior could be approximated in a 2D model by adding an equivalent spring to the model. This part aims to determine equivalent stiffness coefficients based on an assessment of the ambient wavefield.

2 Outline

A model to determine the spatial characteristics of a wave field is developed first. Wave statistics for several environmental test cases are derived. From there, the equivalent stiffness is determined.

3 Description of wave field

3.1 FORMULATION OF WAVE ENVIRONMENT

A sea state is described by its wave spectrum. Recalling equation 27, a directional wave spectrum is defined as:

$$S_\eta(\omega,\theta) = S_\eta(\omega)D(\theta)$$

In which the wave spectrum $S_\eta(\omega)$ is modeled as a JONSWAP spectrum [26]. A cos^{2s} model [21] is used for the directional distribution $D(\theta)$. Environmental data is found in section 3.4 and Appendix A.

3.2 FORMULATION OF THE WAVE FIELD

From the spectral description, a Gaussian wave field is then modelled using the 3D random phase/amplitude model, defined in equation 24:

$$\eta(x,y,t) = \sum_{i=1}^{N}\sum_{j=1}^{M} a_{i,j}\cos\left(\omega_i t - k_i x\cos\theta_i - k_j y\cos\theta_j + \varphi_{i,j}\right)$$

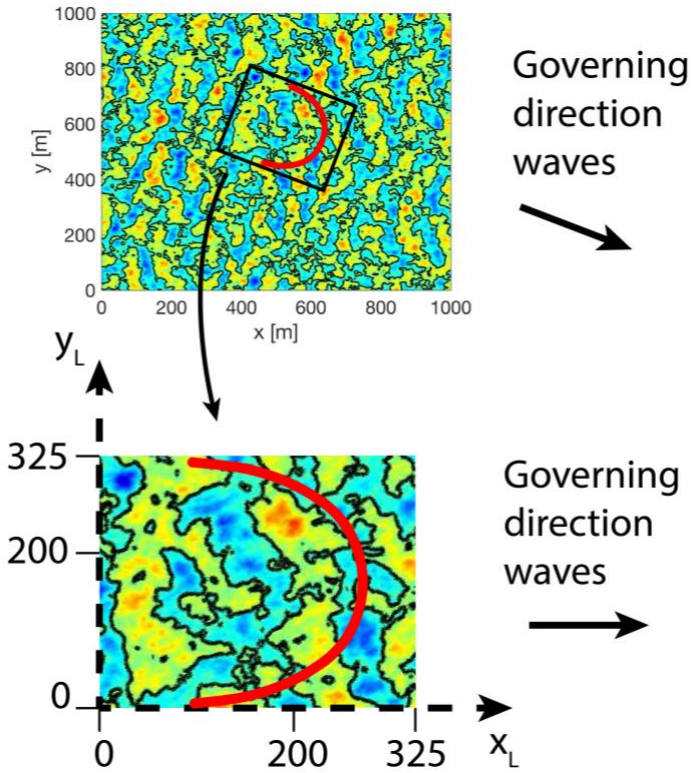

Figure 23 Transformation from global coordinate system to local coordinate system. The first figure shows a top view from a wave field defined in its global coordinates. The second figure shows a top view of a selected part of the wave field in its local coordinates.

3.3 DEFINING THE SPATIAL SIZE OF WAVES

From equation 56, it is observed that the equivalent bending stiffness k_{eq} is extremely sensitive to the crest length L_c of the incoming wave. A method to derive statistics for the crest length is given below. This method is inspired by the work of Podgórski and Rychlik [38].

First, recall the assumption of a wind vaning system (from part I). The governing direction of the wind waves will always be perpendicular to the barrier. Then transform the global coordinates of the wave field to a local coordinate system, such that the governing wave direction in the local coordinate system is always in x_L-direction. The crest length of a wave is then defined along its y_L -axis. Figure 23 gives a visualization of how the global coordinate system is transformed to the local coordinate system.

Now, within each wave crest, the highest local maximum $\boldsymbol{q} = (x_q, y_q)$ is sought for. Then, for this point, its distance to the zero-crossing points in x_L- and y_L-directions are looked into. An ellipse, identifying individual waves, is then drawn with its axis based on the distance to the zero-crossing points in x_L- and y_L-direction respectively.

For time instant t, let $\eta(x,y)$ be the stationary wave field, the previously described method is then following the next definition:

DEFINITION: "let $\boldsymbol{x}_{up} = (x_{up}, y_q)$ and $\boldsymbol{x}_{down} = (x_{down}, y_q)$ be the zero-crossing points in x-direction defined for point $\boldsymbol{q} = (x_q, y_q)$. While $\boldsymbol{y}_{up} = (x_q, y_{up})$ and $\boldsymbol{y}_{down} = (x_q, y_{down})$ are its zero-crossing points in y-direction. Then an ellipse, identifying a wave, is drawn when point $\boldsymbol{q}$ is the highest local maxima lying within the interior of the ellipse, $\eta(\boldsymbol{q}) = max_{(x,y)\in\mathcal{E}}[\eta(x,y)]$. And when its axis A_{minor}, A_{major}, centered at point $\boldsymbol{c}$, are not crossing any axis of other ellipses. The ellipse is centered at point $\boldsymbol{c} = (\frac{(x_{up}+x_{down})}{2}, \frac{(y_{up}+y_{down})}{2})$, with axis minor $A_{minor} = \frac{(x_{down}-x_{up})}{2}$ and axis major $A_{major} = \frac{(y_{down}-y_{up})}{2}$.

Figure 24 shows an example of a snapshot of the sea surface elevation $\eta(x,y)$ with ellipses $\mathcal{E}_i$ plotted, according to the definition given above. From the figure, it is observed that individual wave crests are now identified. Now, for any wave field that is transformed to the local coordinate system, the spatial spread of waves is indicated by A_{minor} and A_{major}. The same exercise can be applied per time step on the wave field $\eta(x,y,t)$, performing a space-time analysis. Using this model, the crest length of a wave is defined as:

$$L_c = A_{major} \tag{67}$$

4 Model implementation

A flow chart of the hydrodynamic model is given in Figure 25. The significant wave height H_s and peak period T_p are input as environmental parameters to the WAFO toolbox. The WAFO toolbox calculates a directional spectrum $S(\omega,\theta)$ and simulates a wave field $\eta(x,y,t)$. The wave field analyzer, developed in this part, derives statistics for the crest length L_c, which are used as an input for to calculate the equivalent stiffness coefficient according equation 56.

5 Model output and visualization

For given characteristics of the wave field, the model determines wave crest statistics and corresponding spring stiffness coefficients. Using the method described in section 3.3, an empirical cumulative distribution function of the measured crest lengths occurring in the wave field is derived. Note that the domain where measurements are performed is truncated to an area of 325m*325m. All measurements in x_L- and y_L-direction above 325m will be eluded. This means that the occurrence of a wave with crest length above 325m is counted, but its length is unknown and thus eluded from the data. For relatively long-crested sea state this gives an ECDF of known values. The sum of this ECDF does not equal to one because there are also samples with unknown values. Figure 26 shows examples of the visualization of crest length statistics for a short-crested and long-crested sea state respectively. Note that for the latter some data is eluded and thus the ECDF does not add up to one. Crest length statistics and corresponding equivalent stiffness coefficients will be also given in tables.

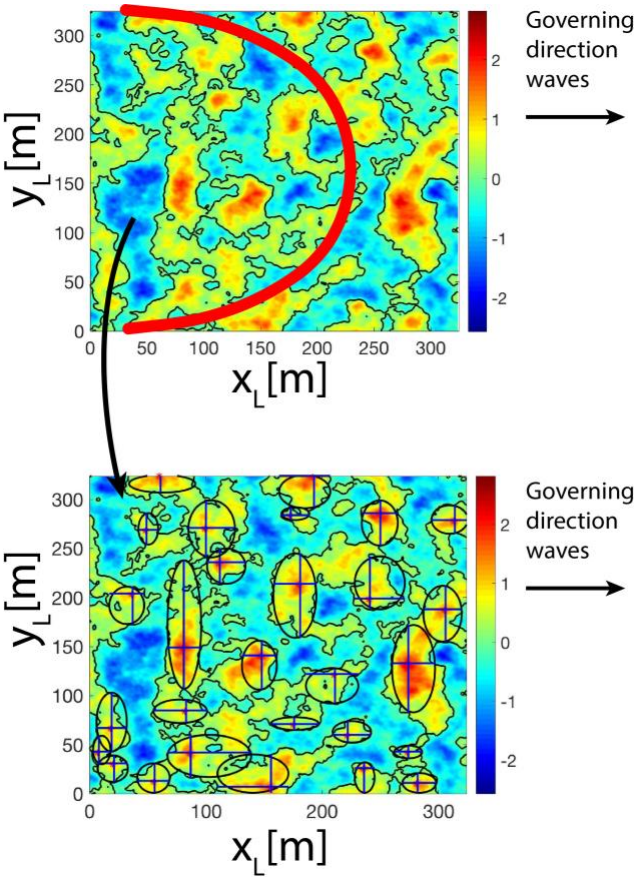

Figure 24 Identification of wave crest for $H_s = 3, T_p = 8$

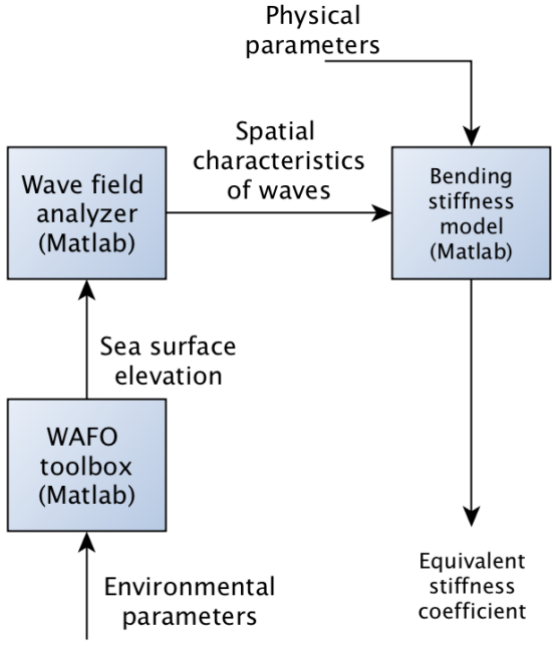

Figure 25 Flow chart model to determine the spatial characteristics of waves and determine equivalent stiffness coefficient.

6 Input data

6.1 ENVIRONMETAL TEST CASES

To maintain consistency, the same test conditions are chosen for all three parts. Referenced is to section 6.3 of part I and Table 4 where the wave cases are determined. An elaboration on the choice of these parameters is found there. The H_s and T_p values corresponding to these wave cases are used by the WAFO toolbox as an input.

6.2 SIMULATION PARAMETERS

6.2.1 Computational domain

The domain of the wave field that is measured is truncated to a square box of 325m by 325m.

6.2.2 Duration and time step

The simulation time was chosen as $t = 6000s$ with a time step of $dt = 1s$.

7 Results

7.1 CREST LENGTH STATISTICS

Using the environmental wave model, the crest lengths occurring in the wave field were analyzed. Figure 27 shows the empirical cumulative distribution functions of the measured crest length L_c in the wave field, per environmental case. When evaluating equation 56, it is seen that the equivalent bending stiffness is inversely proportional to the crest length to the power third. For small values of L_c, the stiffness increases rapidly. Therefore, the 5-, 20- and 50-percentile values of L_c derived from the ECDF's are looked into. The 5- and 20-percentile value are taken as a conservative value, while the 50-percentile value represents the median value. Values of L_c are given in Table 6.

7.2 EQUIVALENT SPRING COEFFICENTS

First, serving as reference values, a spring stiffness of zero and an infinite spring stiffness are chosen. Next, equation 56 is evaluated at the 5-, 20- and 50-percentile values for L_c given in Table 6. This results in five cases for the equivalent spring stiffness per wave case, given in Table 7.

7.3 FREQUENCY RESPONSE CHARACTERISTICS

Per wave case, the frequency response characteristics are determined for the different configurations of the equivalent spring stiffness k_{eq} (given in Table 7). Figure 62 to Figure 67 in appendix I, show the graphs of the frequency response characteristics for wave case 1 to wave case 6. It is shown that short-crestedness of waves is related to a degraded motion response of the hydrodynamic model. For decreasing percentile values, crest length L_c becomes smaller and the motion response is decreasing. Also, for decreasing peak period, the crest length L_c becomes smaller and the motion response is decreasing.

8 Evaluation

8.1 WAFO

The development of the WAFO toolbox has been thoroughly tested and had its theoretical background reviewed. See [39-41] for further information.

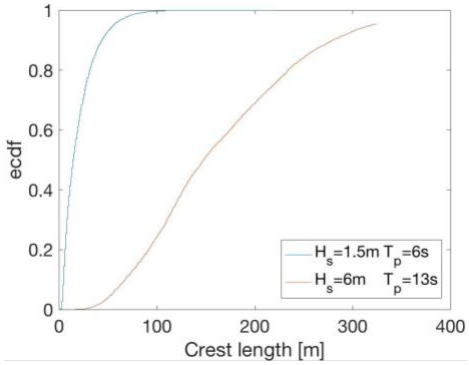

Figure 26 Visualization of crest length statistics in the form of empirical distribution functions

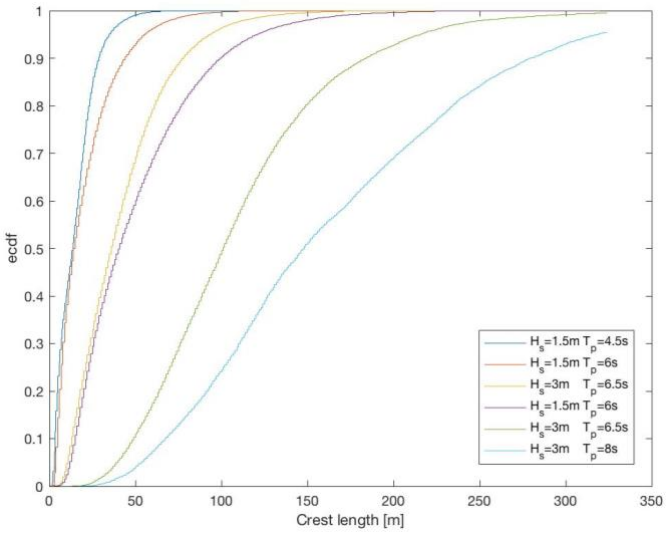

Figure 27 Empirical distribution functions of the considered wave cases

Wave case / Environmental parameter	H_s [m]	T_p [s]	Lcrest P50 [m]	Lcrest P20 [m]	Lcrest P5 [m]
Case 1	1.5	4.5	13.35	4.635	2.553
Case 2	1.5	6	14.02	5.949	3.403
Case 3	3	6.5	35.73	17.81	10.16
Case 4	3	8	40.08	19.76	11.86
Case 5	6	9.5	100.5	63.43	39
Case 6	6	13	147.2	91.24	53.15

Table 6 Wave cases and their crest length statistics

Wave case / Environmental parameter	k_0 [kN/m]	k_{inf} [kN/m]	k_{p_50} [kN/m]	k_{p_20} [kN/m]	k_{p_05} [kN/m]
Case 1	0	inf	78.732	1880.1	11248
Case 2	0	inf	67.886	889.33	4750.2
Case 3	0	inf	4.1033	33.125	178.59
Case 4	0	inf	2.9077	24.279	112.111
Case 5	0	inf	0.1841	0.7335	3.1545
Case 6	0	inf	0.0586	0.2465	1.2465

Table 7 Equivalent spring stiffness values per wave case

8.2 CONVERGENCE OF RESULTS WITH RESPECT TO SIMULATION TIME

For case 2 to 6, results were drawn from simulations with a simulated time of 6000s. For case 1, due to long run times, results were drawn from a simulation with a simulated time of 3000s. Convergence of measurements was checked with regard to the simulated time of the simulations. Appendix H shows results for different simulated times for each of the wave cases.

For case 2 to 6, results for simulated times of 500s, 1000s, 2000s, 3000s, 4000s, 5000s and 6000s were compared. For case 1, results for simulated times of 500s, 1000s, 2000s and 3000s were compared. The graphs in Appendix H show a quick convergence of results, showing that the chosen run times are sufficient.

8.3 CREST LENGTH MEASUREMENTS

Although some research was done on crest length statistics [38, 42-44], no comparable results or experimental data was found to perform a verification or validation study with.

9 Discussion

9.1 REVIEW OF RESULTS

When regarding the frequency response characteristics in appendix I, the test cases can be divided into three categories.

The first category includes wave case 1 and wave case 2. When the k_{p_50} spring case is taken, already a severe degradation in the motion response is seen. The k_{p_20} and k_{p_05} case show negligible motion response.

The second category covers wave case 3 and 4. The k_{p_50} spring case shows a relatively well performance. with this spring configuration, the floater will still be able to follow the waves sufficiently. When a k_{p_20} value is applied, the RAO-value will be about 0.5 [m/m]. For k_{p_05} the floater's motion response is still severely restricted.

The final, third, category includes wave case 5 and 6. There is neglectable degradation of the motion response found, even when the k_{p_05} value for the equivalent spring stiffness is applied.

9.2 REVIEW OF APPLIED THEORY

The linear wave model combined with a spectral description of the wave environment is a broadly used method to describe wave fields in oceanic waters. The WAFO toolbox was used to simulate wave fields, also see section 8.1.

9.3 REVIEW OF APPROACH

As already discussed in Part I, a tradeoff between simplicity and accuracy was be made. There, it was chosen to capture effects due to bending resistance in a single constant value in the form of an equivalent spring stiffness. In this part, it then was chosen to test a range of spring stiffness values per wave case. The spring cases k_0, k_{inf}, k_{p_50}, k_{p_20} and k_{p_05} are chosen to cover a range of possible bending resistance of the floater.

k_0 and k_{inf} would be the 'best' and 'worst' case scenarios respectively. The first excludes bending stiffness from the hydrodynamic model. While the latter applies an infinite spring stiffness, restricting the floater in (heave) motion.

The cases k_{p_50}, k_{p_20} and k_{p_05} were based on the ECDF's of the crest lengths found in Figure 27. In this way representative values for the equivalent spring stiffness based on wave conditions encountered throughout the domain could be found.

k_{p_50} was based on the median wave crest length found. 50% of the crest lengths are below this value and 50% above this value. It then means that when this value is chosen, the actual spring stiffness is overestimated 50% and underestimated 50% of the times when regarding the crest length of the incoming wave. As the equivalent spring stiffness coefficient leads to degraded motion response, underestimation of the spring stiffness leads to underestimation of the overtopping statistics. Overestimation of the spring stiffness coefficient would lead to overestimation of the overtopping statistics.

Case k_{p_20} considers a more conservative value for the equivalent spring stiffness when used in a wave overtopping assessment. Its value is based on the 20% shortest crest length present in the wave field.

The case k_{p_05} considers an extremely conservative value to approximate the bending behavior of the floater. The equivalent spring stiffness constant is based on the 5% shortest crest length present in the wave field.

10 Conclusions

A method to determine crest length statistics is developed. Using these statistics, values for the equivalent stiffness coefficients were derived. This method serves as a first approximation towards including bending stiffness effects into a hydrodynamic model by capturing bending resistance behavior in a linear spring. This method is not verified nor validated. The validity of this method is thus subject for future research.

It is expected that for wave cases 1 to 4, in at least one of the spring configurations, the motion response of the floater will be significantly restricted. For case 5 and 6, values for the equivalent spring stiffness are low and its influence on the response is expected to be negligible.

Future research recommendations:

- No validation or verification study was performed to assess the quality of the model. A future validation/verification study is advised.

PART III – WAVE OVERTOPPING ASSESMENT BASED ON A COUPLED HYDRODYNAMIC-CFD ANALYSIS

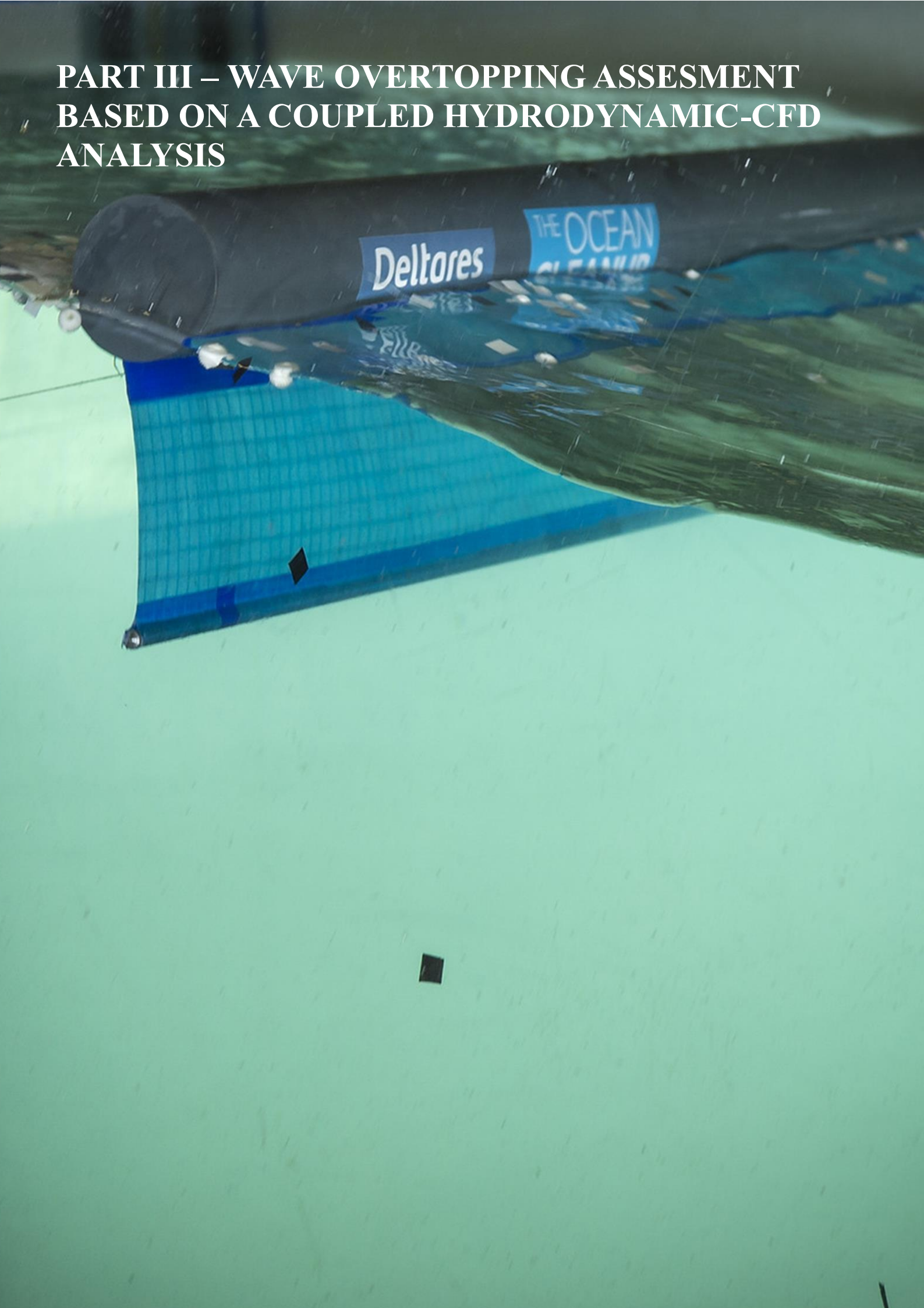

Part III – Global wave overtopping and plastic loss assessment

Keywords

Wave Overtopping, Fluid interaction with moving body, Free-surface motion, ComFLOW, Two-dimensional Computational Fluid Dynamics, Navier-Stokes, Volume-of-Fluid, Numerical modelling, Numerical wave tank

Abstract

In the investigation of wave overtopping, an accurate description of the free-surface and fluid flow around the object is required. Part III handles coupling of the previously developed hydrodynamic model to the CFD solver ComFLOW. Wave overtopping statistics are derived from simulations in a 2D numerical wave tank with imposed motion. In the cases with low wave steepness, derivation of overtopping statistics has been achieved and results show that overtopping performance can be assessed by performing the steps taken in this research project. In these cases, the wave field is generally behaving linear and the motion response obtained from the hydrodynamic model can be coupled to the CFD solver. Results show that wave height and the applied spring stiffness are governing parameters for overtopping performance. It was also found that in some cases, non-linearities are introduced in the wave field. In the cases where non-linearities occur, the motion response derived by the hydrodynamic model deviates from the motion response that one would expect. Here, a significant error is found in the overtopping statistics.

1 Introduction

This part aims to couple a volume of fluid (VOF) method to the time-domain motion of a two-dimensional cylinder. It is then proposed that a fluid flow over the considered object, due to overtopping, can be measured.

2 Outline

First, a summarized description of the workings of ComFLOW is given. Then, a motion time trace is calculated by the previously developed hydrodynamic model and imposed onto a model of the floater in the numerical wave tank. In this CFD model, an overtopping assessment is performed for the six considered environmental cases. Finally, results are discussed and part III is concluded.

3 Description of ComFLOW

ComFLOW [45] is a numerical tool based on the Navier-Stokes equations. One of its application areas is the marine and offshore industry, where it is used to describe complex free-surface problems (e.g. green water and wave impact loading). ComFLOW is able to run one-phase or two-phase models. The one-phase flow model, applied here, considers the Navier-Stokes equations, describing the flow of an incompressible viscous fluid with a free liquid surface [46].

3.1 CONCISE FORMULATION OF ONE-PHASE FLOW MODEL

A concise description of the one-phase model is given here. For a more thorough derivation of the governing equations, boundary conditions, as well as the description of space and time discretization techniques, reference is given is to literature: [45-49].

3.1.1 Governing Equations

The motion of a homogeneous, incompressible, viscous fluid in a three-dimensional domain Ω is described by the continuity equation (conservation of mass) and the Navier-Stokes equations (conservation of momentum). In conservative form, for a domain Ω with domain boundary Γ, they read:

$$\oint_{\Gamma} \boldsymbol{u} \cdot \boldsymbol{n}\, d\Gamma = 0 \tag{68}$$

$$\int_{\Omega} \frac{\partial \boldsymbol{u}}{\partial t} d\Omega + \oint_{\Gamma} \boldsymbol{u}(\boldsymbol{u} \cdot \boldsymbol{n}) d\Gamma + \frac{1}{\rho} \oint_{\Gamma} p\boldsymbol{n}\, d\Gamma - \upsilon \oint_{\Gamma} \nabla \boldsymbol{u} \cdot \boldsymbol{n}\, d\Gamma - \int_{\Omega} \boldsymbol{f}\, d\Omega = 0 \tag{69}$$

in which ρ is the density, υ the kinematic viscosity, $\boldsymbol{u} = (u, v, w)^T$ the velocity vector, $\boldsymbol{n}$ the vector normal to the volume boundary and $\boldsymbol{f}$ the vector containing external forces acting on the control volume. Note that density and viscosity are assumed to be constant.

Displacement of the free surface is, considering an incompressible fluid, described by:

$$\frac{DS}{Dt} = \frac{\partial S}{\partial t} + \nabla \cdot (\boldsymbol{u} S) = 0 \tag{70}$$

In which $S(\boldsymbol{x}, t)$ is the position of the free surface.

3.1.2 Boundary Conditions and Free Surface

To derive a solution for eq.'s 68, 69 and 70, conditions have to be set to all boundaries of the fluid domain. At solid boundaries, the no-penetration and no-slip conditions are applied. These conditions state that there is no fluid flow through (normal direction) or along (tangential direction) the solid boundary. In other words, the velocity of the fluid is zero relative to the boundary:

$$\boldsymbol{u} = 0$$

Or in the case of a moving solid boundary:

$$\boldsymbol{u} = \boldsymbol{u}_b$$

The free surface of the fluid is also a boundary and such an interface requires two conditions to be applied. By applying the normal stress balance and tangential stress balance:

$$-p + 2\mu \frac{\partial u_n}{\partial n} = -p_0 + \sigma\kappa \tag{71}$$

$$\mu\left(\frac{\partial u_n}{\partial t}+\frac{\partial u_t}{\partial n}\right)=0 \qquad (72)$$

Here, p is the pressure, p_0 the atmospheric pressure, μ dynamic viscosity, σ the surface tension, κ the curvature of the free surface and u_n and u_t the normal and tangential component of the velocity, respectively.

To reduce computational time, the size of the model domain is chosen such that it only covers the structure and the surroundings of interest. A guide on choosing the right size of the model domain is given in the ComFLOW manual [45].

The model domain Ω is bounded by the domain boundary Γ. In order to perform a realistic simulation, environmental conditions should be allowed to enter and leave the (truncated) domain. To achieve this, fluid must be allowed to flow in or out of the domain at certain boundaries. Here, the interest lies in the simulation of propagating waves. This requires the inflow and outflow boundary to be 'open' for the wave propagating through the fluid domain. A clever type of boundary condition is built in ComFLOW [45]. The generating and absorbing boundary condition (GABC) has a combined functionality of wave generation and wave absorption [47-49]. The GABC is able to generate waves while absorbing dispersive waves with a broad spectrum of wave numbers, reducing non-physical reflection of waves at the boundary to a minimum. The GABC is determined by [47]:

$$\left(1+b_1h^2\frac{\partial^2}{\partial z^2}\right)\frac{\partial\phi}{\partial t}+\sqrt{gh}\left(a_0+a_1h^2\frac{\partial^2}{\partial z^2}\right)\frac{\partial\phi}{\partial n}=0 \qquad (73)$$

In which:

$$\phi=\phi_{in}+\phi_{out} \qquad (74)$$

The coefficients a_0, a_1, b_1 are based on an approximation of the linear dispersion relationship [47]:

$$c\approx\sqrt{gh}\frac{a_0+a_1(kh)^2}{1+b_1(kh)^2} \qquad (75)$$

Where, h the depth, k the wavenumber and g the gravitational constant. The values of a_0, a_1, b_1 can be chosen such that a chosen range of the dispersion relationship is approximated, corresponding with the wavenumber range of the to be absorbed waves [45,47-49]. See Figure 28.

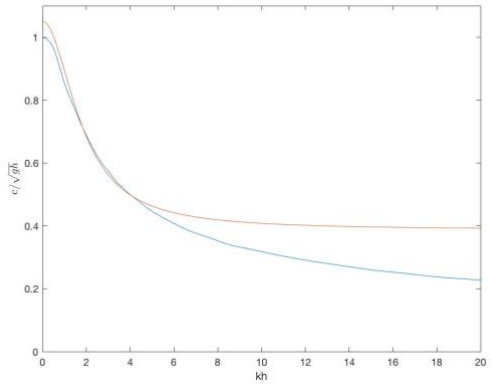

Figure 28 approximation of a chosen range of the dispersion relationship by equation 75

3.1.3 Wave generation

Waves are generated according to the wave potential ϕ_{in} formulated in equation 8:

$$\phi=\frac{\eta_a g}{\omega}\frac{\cosh[k(d+z)]}{\sinh(kd)}\sin(\omega t-kx+\varphi)$$

3.2 FORMULATION OF NUMERICS

Equations 68 and 69 are solved by using a numerical approach. The continuity equation and Navier-Stokes equations are discretized in time and space. First a structured Cartesian grid is defined for finite-volume discretization of the domain Ω. The grid defines cells, also known as control volumes. The sum of volume of individual cells is equal to the total volume of the domain. A uniform grid (cells are square boxes), as well as a stretched grid (cells are rectangular boxes) can be applied. The cells within the domain are separated in classes based on similarity of properties. Figure 29 depicts how cells are labeled. A boundary cell **B** cannot contain fluid and is fully filled by the object. The empty cell **E** does not contain fluid but fluid may flow in during simulation. A fluid cell **F** is (almost completely) filled with fluid and fluid may flow out/in during simulation. The free surface is positioned with surface cells **S**, they are partially filled with fluid and forming the boundary between fluid and empty cells. Cell labeling and the liquid fill ratio of **S** and **F** is resolved at every time step. Pressure and velocity are given for individual cells using staggered variables. Per control volume, pressures are defined in the cell center and the velocity component at its boundaries [46], see Figure 30.

ComFLOW applies a Volume-Of-Fluid (VOF) type of method with a local height function for spatial discretization of the Navier-Stokes equations. The forward Euler method, first-order accurate, is applied for time discretization of the Navier-Stokes equations. Solving of convection and diffusion in time is done by using an explicit method. Pressure is solved in time by using an implicit method. After pressure is solved, the velocity field is calculated. From there, the position of the free surface is redefined.

4 Derivation of wave overtopping characteristics

Two parameters are defined to specify overtopping characteristics. The volumetric flow rate Q and total overtopping volume V. The volumetric flow rate Q gives the volume of fluid passing through a certain surface per unit time:

$$\mathrm{Q(t)}=v*A \qquad (76)$$

With v the velocity of the fluid and A the surface area. In this study, a 2D case is considered. The volumetric flow rate is defined as the volume of fluid passing through a specified area per unit time, per meter section of the barrier. The surface area through which the volume flow is measured, is specified along the face edge of cells closest to the center of the barrier, as indicated with a red line in Figure 31. For each individual cell, ComFLOW gives the velocity at its face edges and the liquid fill ratio of the cell. The liquid fill ratio defines the percentage of volume of a cell that is actually filled with liquid. So, for N cells

with face edge at the surface area, indicated with red, the volumetric flow rate per meter section of the barrier is given as:

$$Q(\mathrm{t}) = \sum_{i=1}^{N} u_i(t) * FR_i * \frac{\Delta z}{\Delta y} \qquad (77)$$

For a moving barrier, and thus a surface moving with the barrier, the velocity of the barrier should be subtracted from the fluid velocity, in order to retrieve the volumetric flow rate through the moving surface area A:

$$Q(\mathrm{t}) = \sum_{i=1}^{N} [v_i(t) - v_{barrier}(t)] * FR_i * \frac{\Delta z}{\Delta y} \qquad (78)$$

With Δz the height of the cell, Δy the width of the cell, FR the liquid fill ratio of each cell in front of the surface edge and u the velocity of fluid in x-direction at the face edge of the cell.
The overtopping volume V gives the total volume of fluid, per meter section of the barrier, washed over the barrier during a simulation:

$$\mathrm{V} = \int_0^t \mathrm{Q(t)} dt \qquad (79)$$

5 Model implementation

Figure 32 gives a flowchart of the integration of the hydrodynamic model with the wave overtopping model. Based on given environmental parameters, the WAFO toolbox calculates a directional spectrum $S(\omega, \theta)$ and simulates a wave field $\eta(x, y, t)$. The wave field analyzer derives statistics for the crest length L_c, which are used as an input for to calculate the equivalent bending stiffness. OCTOPUS-office then determines the 2D frequency response characteristics. A motion time trace is then calculated by the hydrodynamic model in Matlab, based on equation 46 and 51. This motion time trace is then imposed into a numerical wave tank, using ComFLOW, while the corresponding sea surface elevation is modelled. Then, overtopping characteristics are derived from the results given by ComFLOW. The volumetric flow rate Q and overtopping volume V per meter section of the barrier are calculated according to the formulae defined in eq. 78 and 79 respectively.
ComFLOW comes with a post-processing tool, named PPR1. It makes use of the MatLab environment. PPR1 reads in the data generated by ComFLOW and is able to calculate cell properties, velocity fields and the pressure field per time step. ComFLOW is only able to measure the flux over a motionless object. Therefore, PPR1 had to be slightly altered and an additional object tracking flux measurement tool was developed: PPR2. A step-by-step guide of the required scripting and steps taken, is found in Appendix J.

6 Model output and visualization

ComFLOW's PPR1 reads in the data generated by ComFLOW and is able to plot cell properties, velocity fields and the pressure field per time step. An example of visualization of the u-component of the velocity is given in Figure 33. The post-processing tool is also able to generate movies of a simulation. This function can be used for visualizing change of a variable

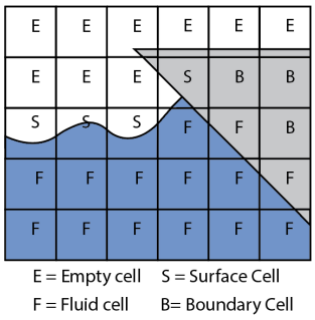

Figure 29 Cell labeling distinguishing empty, surface, fluid and boundary cells. The blue area corresponds with water, grey with an object and white with air. (Image based on [50])

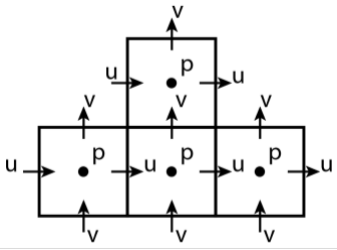

Figure 30 Definition of pressure and velocities. Pressures are defined at the cell center and the velocity component at its boundaries.

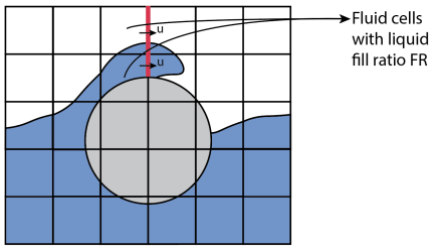

Figure 31 Definition of surface area where fluid passes through.

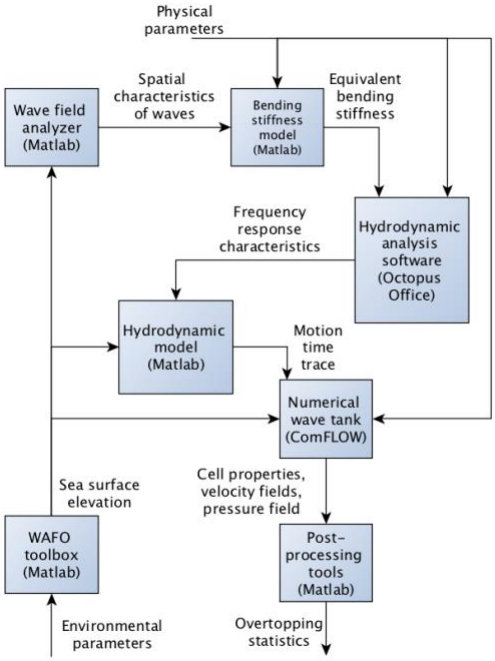

Figure 32 Flow chart wave overtopping model

over time, as shown Figure 34, or to visualise the simulation itself in a 3D plotting mode, as seen in Figure 35. PPR2 is written to derive the volume flux over the barrier and calculate overtopping statistics. The volumetric flow rate Q and overtopping volume V per meter section of the barrier are calculated according to the formulae defined in eq. 78 and 79 respectively. Figure 36 shows an example of the visualization of the volumetric flow rate per meter section of the barrier against time of simulation. The greyed-out area is the start-up/initialization phase, which is not taken into account during the wave overtopping assessment.

7 Input data

7.1 ENVIRONMENTAL CASES

To maintain consistency, the same test conditions are chosen for all three parts. Referenced to is section 6.3 of part I and Table 4 where the wave cases are determined. An elaboration on the choice of these parameters is found there. The H_s and T_p values corresponding to these wave cases are used by the WAFO toolbox as an input.

7.2 EQUIVALENT STIFFNESS COEFFICIENTS

Five cases for the equivalent spring stiffness, per wave case, are used. Referenced is to section 7.2 of part II and table 7. There, the equivalent spring stiffness was determined. A derivation of these coefficients can also be found in part II.

7.3 FREQUENCY RESPONSE CHARACTERISTICS

Per wave case, the frequency response characteristics are evaluated for the 5 different configurations of the equivalent bending stiffness k_{eq}. Referenced to is section 7.3 and Figure 62 to Figure 67 in appendix I.

7.4 SIMULATION PARAMETERS

The simulation parameters used in the CFD study are summarized in Table 8. Explanation of the parameters is given below in section 7.4.1-7.4.4.

7.4.1 Computational domain

The computational domain Ω of NWT has to be chosen carefully. The domain should be chosen as small as possible in order to perform time efficient simulations, but large enough so that waves do not interfere with the NWT's boundaries.

To model propagation of deep water waves accurately, the NWT should be deep enough so that waves do not interfere with the NWT's bottom. i.e., the NWT should be chosen deep enough so that $\tanh(kd)$ approaches 1 in the dispersion relationship and wavelength is not influenced by depth. From linear wave theory [21], taking λ_{max} the maximum wavelength found in the spectrum, deep water can be assumed when:

$$h > \frac{1}{2} * \lambda_{max}$$

this value is then chosen as the depth of the wave tank.

Also, the tank was chosen long enough so that waves could develop and not interfere with boundaries. These values where basically chosen on a trial and error basis and found in Table 8.

7.4.2 Spatial discretization of domain

Discretization of the spatial domain Ω of the NWT was done based on guidelines given in the ComFLOW manual [45].

A 3% cell stretching was applied in the vertical domain, reducing the number of cells needed, while maintaining a fine grid resolution in the vicinity of the sea surface. Values are found in Table 8.

7.4.3 Duration and time step

Simulations were run 200 seconds of which 50 seconds are an initialization phase and the last 150 seconds are used to calculate overtopping statistics. Timestep dt was chosen 0.01. CFL parameters are chosen as default [45]. See Table 8 for values.

7.4.4 GABC conditions

A Sommerfeld condition was applied to the GABC [47] boundary conditions. This means that the a_0-coefficient is determined as:

$$a_0 = \sqrt{\frac{\tanh(kh)}{kh}} \tag{80}$$

While a_1, b_1 are equal to zero. Equation 75 then becomes:

$$c \approx \sqrt{gh}\sqrt{\frac{\tanh(kh)}{kh}} \tag{81}$$

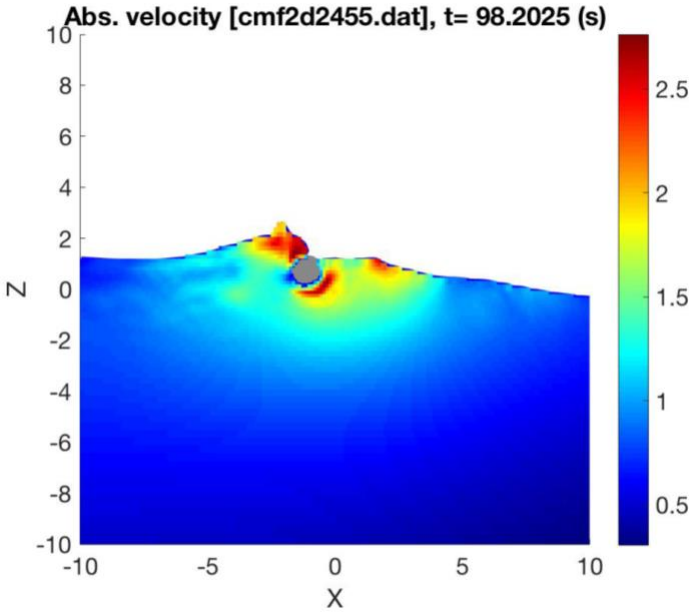

Figure 33 Visualization of u-component at time t

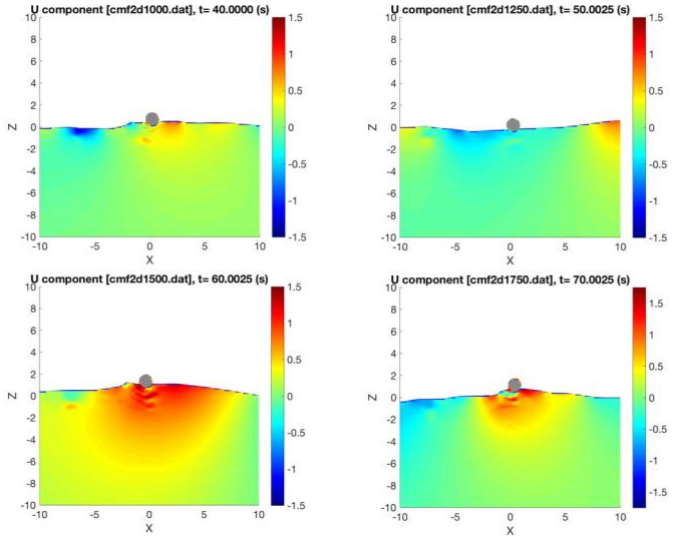

Figure 34 Snapshots of movie visualizing the variation of the u component over time.

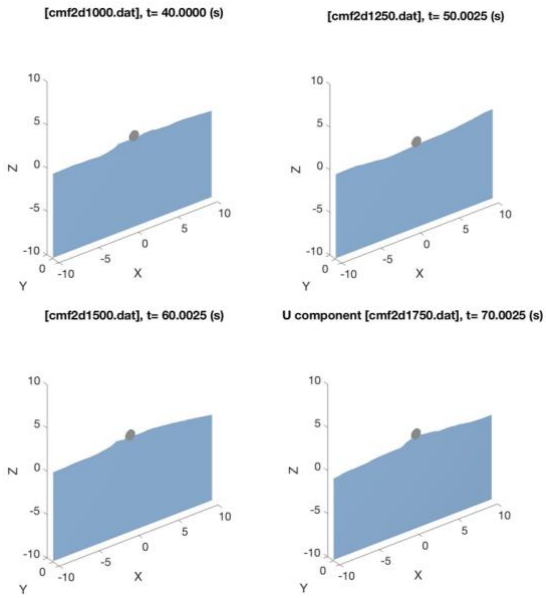

Figure 35 Snapshots taken from movie visualizing 2D simulation of waves including a floater with imposed motion.

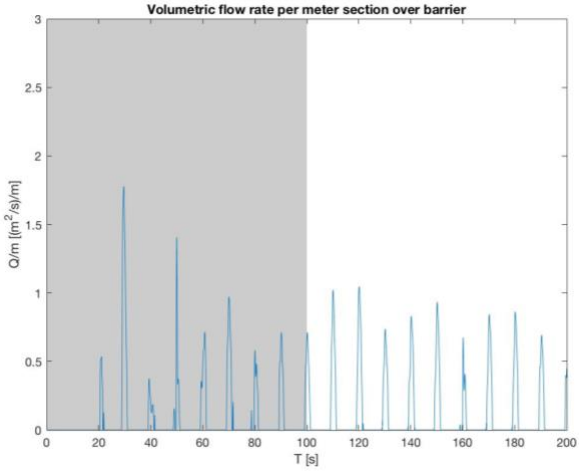

Figure 36 Example of visualization of volumetric flow rate over the barrier, per meter section of the barrier. Here, a regular wave (H=3, T=6) was applied on a non-moving floater.

Wave case / Simu-lation parameter	Case 1	Case 2	Case 3	Case 4	Case 5	Case 6
Length tank L_{tank}	64	114	132	132	132	132
Depth tank D_{tank}	-46.63	-82.34	-96.12	-147.5	-205.8	-386.5
Height tank h_{tank}	3.041	3.041	6.117	6.117	12.35	12.35
N_x	533	950	1100	1100	1100	1100
N_z	103	121	138	152	179	200
N_{total}	54899	114950	151800	167200	196900	220000
s_z	1.03	1.03	1.03	1.03	1.03	1.03
s_x	1.00	1.00	1.00	1.00	1.00	1.00
t	200s	200s	200s	200s	200s	200s
dt	0.01	0.01	0.01	0.01	0.01	0.01
Max (dt)	0.1	0.1	0.1	0.1	0.1	0.1
CFL-number	1	1	1	1	1	1
Min (CFL)	0.3	0.3	0.3	0.3	0.3	0.3
Max (CFL)	0.8	0.8	0.8	0.8	0.8	0.8
GABC a0 (Sommerfeld condition)	0.3285	0.3296	0.3305	0.3283	0.3301	0.3296

Table 8 Simulation parameters

8 Results

Overtopping statistics were derived for the considered test cases. Graphs of the volumetric flow rate Q per meter section of the barrier are found in Appendix K. The total overtopping volume per simulation run is found in Table 9.

Figure 74 to Figure 79 in Appendix L give the total overtopping volume plotted against the equivalent spring stiffness coefficient.

Finally, Figure 80 in Appendix M plots the total overtopping volume against wave steepness, corrected for wave height, for wave case 2, 4 and 6. The wave steepness was corrected for wave height and calculated as follows:

$$s_{corr} = \frac{2\pi(H - 0.5 * D)}{9.81T^2} \quad (82)$$

In which D is the cylinder's diameter, H the wave height and T the wave period. H and T were chosen as the H_s and T_p values respectively. The wave steepness was corrected in order to find a better trend in the results. The correction 'accounts' for the fact that wave cases with a lower wave height won't result in overtopping.

The cases 1, 3 and 5 showed erroneous results and where therefore not included in Figure 80. These errors are introduced by non-linearities occurring in the CFD simulations while this is not accounted for in the hydrodynamic model. From the movie images it was seen that wave breaking occurs and the wave field is distorted. The non-linearities are not accounted for in the linear wave model on which the hydrodynamic model was based on. The time trace that was determined from the hydrodynamic model and imposed onto the cylinder in the numerical wave tank is thus erroneous. In the movie images it seen that wave breaking occurred, the wave field was distorted, which results in a wrong motion response of the floater, sometimes causing it to plunge into the sea surface, resulting in large overtopping events. Figure 81 in Appendix N shows a series of snapshots visualizing an example of such a wave breaking event.

Test Case	Wave case	H_s [m]	T_p [s]	L_c [m]	k_{eq} [KN/m]	V [m^3/m]
1	Case 1	1.5	4.5	-	0	14.92
2	Case 1	1.5	4.5	-	inf	24.47
3	Case 1	1.5	4.5	13.35	78.732	20.47
4	Case 1	1.5	4.5	4.635	1880.1	24.61
5	Case 1	1.5	4.5	2.553	11248	23.94
6	Case 2	1.5	6	-	0	0.01676
7	Case 2	1.5	6	-	inf	0.3490
8	Case 2	1.5	6	14.02	67.886	0.05643
9	Case 2	1.5	6	5.949	889.33	0.5471
10	Case 2	1.5	6	3.403	4750.2	0.4712
11	Case 3	3	6.5	-	0	95.25
12	Case 3	3	6.5	-	inf	105.2
13	Case 3	3	6.5	35.73	4.1033	84.49
14	Case 3	3	6.5	17.81	33.125	77.94
15	Case 3	3	6.5	10.16	178.59	97.43
16	Case 4	3	8	-	0	8.502
17	Case 4	3	8	-	inf	30.21
18	Case 4	3	8	40.08	2.9077	7.091
19	Case 4	3	8	19.76	24.279	10.43
20	Case 4	3	8	11.86	112.111	21.22
21	Case 5	6	9.5	-	0	230.2
22	Case 5	6	9.5	-	inf	315.5
23	Case 5	6	9.5	100.5	0.1841	250.8
24	Case 5	6	9.5	63.43	0.7335	213.8
25	Case 5	6	9.5	39	3.1545	207.7
26	Case 6	6	13	-	0	3.002
27	Case 6	6	13	-	inf	102.6
28	Case 6	6	13	147.2	0.0586	3.033
29	Case 6	6	13	91.24	0.2465	5.194
30	Case 6	6	13	53.15	1.2465	4.515

Table 9 Overtopping volumes per meter section of the barrier for a simulation run of 200s, regular and irregular wave cases

9 Evaluation

9.1 COMFLOW

The development of the ComFLOW software has gone through several joint-industry-projects, in which it has been thoroughly tested and validated by its developers. For further information, See [51].

9.2 COMPARISON OF WAVE INPUT HYDRODYNAMIC MODEL AND SIMULATED WAVE IN COMFLOW

Appendix O compares the linear wave signal used by the hydrodynamic solver in part I with the measured wave signal in ComFLOW at the location of the cylinder, while following the same mesh strategy as described in section 7. This is done to check if the linearly derived motion time trace would be valid to use when imposed onto the cylinder in the CFD model.
It is seen that for case 2, 4 and 6 the signals compare relatively well. In case 1, 3 and 5 it is seen that events occur in which the signals show significant deviations from each other. This can be attributed to non-linearities occurring in the wave field simulated in ComFLOW. Due to these non-linearities, the wave field is changed and a linear description does not hold anymore. This leads to difference in the linearly derived wave signal and the signal measured in ComFLOW. It might thus also lead to an erroneous imposed motion time trace onto the cylinder in case 1, 3 and 5.

9.3 VALIDATION OF OVERTOPPING MEASUREMENTS

Calculation of the volumetric flow rate Q, by the PPR2 postprocessor, is validated against results derived from the flux measurement tool available within ComFLOW. The ComFLOW flux measurement tool is not able to track a moving object and the comparison study is thus done for waves running over a still cylinder. The case that is analyzed corresponds to waves of $H = 3m$ and $T = 6s$ which are running over a fixed cylinder with $D = 1.2m$, for a duration of $t = 5T = 30s$. Figure 37 shows the graphs produced by the reference and the PPR2 tool respectively. It is observed that the PPR2 tool produces comparable results as the ComFLOW reference tool.

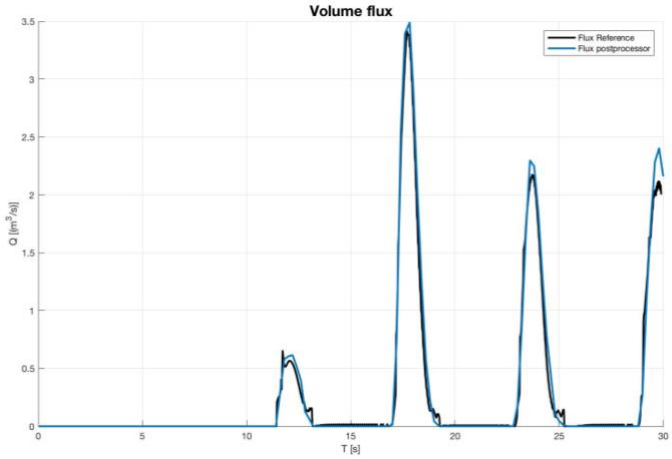

Figure 37 Validation of flux postprocessor with ComFLOW measurement tool. Test case: $H = 3, T = 6, D = 1.2, t = 3$

10 Discussion

10.1 REVIEW OF RESULTS

For Case 1 (see Figure 68 and Figure 74), Case 3 (see Figure 70 and Figure 76), Case 5 (see Figure 72 and Figure 78), relatively

high volumes of overtopping were observed. As explained in section 8, this is introduced due to non-linearities introduced in the wave field. Over the 200 seconds of simulated time, it is evaluated that the wave field will deviate too much from the linear wave signal, which was used for the hydrodynamic model. These cases are therefore not taken into account when concluding upon the overtopping performance of the floater.

For case 2, see Figure 69 and Figure 75, it is first seen that overtopping is neglectable for spring configurations of K0 and K0_50. Although in the latter case the motion response is already heavily restricted, wave overtopping is not observed due to the relatively low wave height ($H_s = 1.5m$), compared to the cylinders diameter ($D = 1.2m$). For the other spring configurations, Kinf, K020 and K005, a comparable development of the volumetric flow rate is seen. Also, the overtopping values lie in the same order of magnitude for these configurations, still being relatively low. This is again explained by the relatively low wave height. Waves seem not to be high enough to be able to run over the floater.

Case 4, Figure 71 and Figure 77, shows a gradual development of overtopping volumes for increased spring stiffness values. This is as expected, as it also shows a gradually decreasing motion response in heave, see Figure 65. A large overtopping volume is observed for a spring stiffness chosen k_{inf}, which is not very realistic however, as bending stiffness is not expected to restrict motions this extreme.

Case 6 shows comparable overtopping results for spring cases k_0, k_{p0_50}, k_{p0_20} and k_{p0_05}. Again, from figure 53, comparable motion response is observed for these spring configurations. Also, here, a large overtopping volume is seen for k_{inf}, but motions are not expected to be restricted this significantly.

When regarding Figure 80 in Appendix M, a trend seems to develop, increased overtopping volumes are observed for an increased corrected steepness and an increased equivalent spring stiffness. However, before one jumps to conclusions, considering the amount of data points more measurements should be performed.

10.2 REVIEW OF APPLIED THEORY

The flow model in this CFD study is based on the Navier-Stokes equations, allowing for non-linear wave behavior. The motion time trace which is imposed on the floater, is derived from the hydrodynamic model developed in part I. This motion is the first order response, an error is thus introduced when waves start to behave non-linearly, while the associated response is still assumed to be linear.

Although the individual models are verified against existing models, it is proposed that the method described is subject to a future validation study.

Also, due to time limitations, the ComFLOW user guide was used to determine the spatial discretization of the domain. There is no domain optimization and grid refinement study performed. This means that the model is not optimized in efficiency and accuracy. It is recommended to do this for future research. As the focus lies on wave overtopping over a cylinder, a refinement based on the cylinder diameter could be a fitting approach [52]:

$$\Delta = \frac{D}{ppcd} \tag{83}$$

10.3 REVIEW OF APPROACH

The one-phase flow model is applied here, modelling sea-water flow including a free surface, while neglecting the presence of air. This is a valid assumption due to the significant difference in density between sea-water and air. Under the conditions where the PCS's are deployed, sea-water is able to contain a large amount of momentum relative to air. The effects of sea-water will thus be governing in wave overtopping phenomena.

A negative volumetric flow rate is not incorporated in the calculation of the total overtopping volume. As a conservative assumption, a volume of water that has flowed over the barrier is considered to be lost and volume flowing back is not considered.

11 Conclusions

A first step into the development of a method able to determine overtopping statistics for a floating boom model has been made. A hydrodynamic motion response model has been combined with accurate free surface simulations in a numerical wave tank. In the cases with low wave steepness, derivation of overtopping statistics has been achieved and results show that overtopping performance can be assessed by performing the steps taken in this research project. In these cases, the wave field is generally behaving linear and the motion response obtained from the hydrodynamic model can be coupled to the CFD solver.

In the cases were non-linearities occur, the motion response derived by the hydrodynamic model deviates from the motion response that one would expect. Here, a significant error is found in the overtopping statistics.

Based on the results from case 2, 4 and 6, it is found that wave height and the value for the equivalent spring stiffness are governing parameters for overtopping performance.

Although more measurement data is needed, Figure 80 seems to hint that there is a link to the (corrected) wave steepness and overtopping volumes. The underlying parameters for steepness are known to be the wave height and period.

Future research recommendations:

- Effects of non-linearity are a recommended subject for future research. A suggestion could be to use a ComFLOW model itself to calculate the motion response. This would however lead to a significant increase in computational time. Solving of the fully coupled motion would require a relatively high resolution of the domain in the vicinity of the cylinder's surface, in order to accurately solve the pressure distribution around the cylinder.
- In order to further asses the quality of the results, it is recommended to perform a thorough verification and validation study.
- A Domain optimization study is recommended for increased efficiency and accuracy of simulations


THE OCEAN CLEANUP
OCEAN FORCE ONE
N120TG

References

1. PlasticsEurope. (2016). Plastics - The facts 2016: An analysis of European plastics production, demand and waste data. Available from: http://www.plasticseurope.org.
2. Barnes D.K.A., Galgani F., Thompson R.C., Barlaz M. (2009). Accumulation and fragmentation of plastic debris in global environments. *Philosopical Transactions Of The Royal Society B.* **364**(1526): p. 1985–1998.
3. Jambeck J. R., Geyer R., Wilcox C., Siegler T.R., Perryman M., Andrady A., Narayan R., Law, K.L. (2015). Plastic waste inputs from land into the ocean. *Science*. **347**(6223): p. 768-771.
4. Lebreton L.C.M., V.d.Z.J., Borrero J.C. (2012). Numerical modelling of floating debris in the world's oceans. *Marine Pollution Bulletin*. **64**(653 - 661): p. 653-661
5. Moore C.J., Moore S.L., Leecaster M.K., Weisberg S.B. (2001). A comparison of plastic and plankton in the North Pacific central gyre. *Marine Pollution Bulletin*. **42**(12): p. 1297–1300.
6. Lebreton L., Slat B., Ferrari F., Sainte-Rose B., Aitken J., Marthouse R., Hajbane S., Cunsolo S., Schwarz A., Levivier A., Noble K., Debeljak P., Maral H., Schoeneich-Argent R., Brambini R., Reisser J. (2018). Evidence that the Great Pacific Garbage Patch is rapidly accumulating plastic. *Scientific Reports*. **8**(4666)
7. Slat B. et al. (2014) How the oceans can clean themselves: A feasibility study. The Ocean Cleanup, Delft, The Netherlands. Availbable from: https://www.theoceancleanup.com/fileadmin/media-archive/Documents/TOC_Feasibility_study_lowres_V2_0.pdf
8. UNEP. (2011). UNEP Year Book 2011: Emerging issues in our global environment. United Nations Environment Programme. Nairobi, Kenya. Available from: http://wedocs.unep.org/bitstream/handle/20.500.11822/8276/-UNEP%20Year%20Book%202012_%20emerging%20issues%20in%20our%20global%20environment-2011UNEP_YEARBOOK_Fullreport.pdf
9. UNEP. (2014). UNEP Year Book 2014: Emerging issues in our global environment. United Nations Environment Programme. Nairobi, Kenya. Available from: http://wedocs.unep.org/bitstream/handle/20.500.11822/9240/-UNEP%20Year%20Book%202014%3a%20emerging%20issues%20in%20our%20global%20environment%20UNEP_YearBook_2014.pdf
10. UNEP, NOAA. (2011). The Honolulu Strategy. A Global Framework for Prevention and Management of Marine Debris. Available from: https://marinedebris.noaa.gov/sites/default/files/publications-files/Honolulu_Strategy.pdf
11. Ellen MacArthur Foundation. (2016). The New Plastics Economy: Rethinking the future of plastics. Available from: https://www.ellenmacarthurfoundation.org/publications/the-new-plastics-economy-rethinking-the-future-of-plastics
12. Allsopp M., Walters A., Santillo D., Johnston P. (2006). Plastic Debris in the World's Oceans. Greenpeace. Available from: http://www.greenpeace.org/archive-international/en/publications/reports/plastic_ocean_report/
13. Kooi M., Reisser J., Slat B., Ferrari F.., Schmid M.S., Cunsolo S., Brambini R., Noble K., Sirks L-A., Linders T.E.W., Schoeneich-Argent R.I., Koelmans A.A. (2016). The effect of particle properties on the depth profile of buoyant plastics in the ocean. *Scietific Reports*. **6**(33882)
14. The Ocean Cleanup. (2018). The Ocean Cleanup Foundation policy plan. Available from: https://www.theoceancleanup.com/fileadmin/media-archive/Documents/TOC_Foundation_Policy_Plan_Beleidsplan.pdf
15. Milgram, J.H. (1971). Forces and Motions of a Flexible Floating Barrier. *Journal of Hydronautics*. **5**(2). p. 41-51
16. Hofland B., van der Mheen M. (2015). 2D Physical model tests for The Ocean Cleanup: Efficiency of the boom cross-section. Deltares, Delft, The Netherlands.
17. van Schoten W. (2015). Calibration Numerical 2D Models. Mocean Offshore B.V., Amsterdam, The Netherlands.
18. Paalvast, M. (2016). 3D Model test results, Mocean Offshore B.V, Amsterdam, The Netherlands.
19. J.M.J. Journée, Massie W.W., Huijsmans R.H.M., (2015). Offshore Hydromechanics, Third edition. Delft University of Technology, Delft, The Netherlands.
20. BOC MetOcean B.V. (2015). *Report P0231-01: Floating barrier - Pacific Ocean*.
21. Holthuijsen L.H. (2007). Waves in Oceanic and Coastal waters. Cambridge University Press, Cambridge, U.K.
22. Chakrabarti S.K. (1987). Hydrodynamics of Offshore Structures. WIT Press, U.S.A.
23. DNVGL. (2010). Recommended practice DNV-RP-C205: Environmental conditoins and environmental loads, in Regular wave theories. Det Norske Veritas.
24. DNVGL. (2011). Recommended practice DNV-RP-H103: Modelling and analysis of marine operations, in General methods of analysis. Det Norske Veritas.
25. Journee J.M.J, Massie W.W. (2001). Course Notes Offshore Hydrodynamics. Delft University of Technology, Delft, The Netherlands
26. Hasselman et al. (1973). Measurements of Wind-Wave Growth and Swell Decay during the Joint North Sea Wave Project (JONSWAP). *Ergnzungsheft zur Deutschen Hydrographischen Zeitschrift Reihe*. **8**(12): p. 95.
27. Herbich, J.B. (1998). Developments in offshore engineering: Wave phenomena and offshore topics, 1st ed. Gulf professional publishing.
28. Ursell, F. (1949). On the heaving motion of a circular cylinder on the surface of a fluid. *The Quarterly Journal of Mechanics and Applied Mathematics*. **2** (2): p. 218-231.

29. Cummins, W. (1962). The impuls response function and ship motion.
30. Perez T., Fossen T.I. (2008). Time- vs. frequency-domain identification of parametric radiation force models for marine structures at zero speed. *Modelling, Identification and Control*. **29**(1): p. 1-19.
31. Berghdal L. (2009). Wave-induced Loads and Ship Motions. Chalmers University of Technology, Göteborg, Sweden.
32. Faltinsen O.M. (1993). Sea loads on ships and offshore structures. *Cambridge ocean technology series*. Cambridge University Press. Cambridge, U.K.
33. Riley, W. (2007). Mechanics of Materials 6th edition. John Wiley & Sons.
34. Hooke, R. (1678). Lectures de potentia restitutiva, or of spring explaining the power of springing bodies.
35. Journée, J.M.J. (2001) Verification and validation of ship motions program SEAWAY. p. 16-28. Delft University of technology, Ship Hydromechanics Laboratory, Delft, The Netherlands.
36. Porter., W.R. (1960). Pressure distributions, added-mass, and damping coefficients for cylinders oscillating in a free surface. University of California, Institution of Engineering Research. Berkeley, California, U.S.A.
37. Vugts, J.H. (1968). The hydrodynamic coefficients for swaying, heaving and rolling cylinders in a free surface. Technische Hogeschool Delft, Laboratorium voor scheepsbouwkunde. Delft, The Netherlands.
38. K. Podgórski, Rychlik I. (2016). Spatial size of waves. *Marine Structures*, **50**: p. 55-71.
39. Brodtkorb P.A., Johannesson P., Lindgren G., Rychlik I., Ryden J., Sjö E. (2000). WAFO – a Matlab toolbox for analysis of random waves and loads. *Proceedings of the 10th International Offshore and Polar Engineering conference*. International Society of Offshore and Polar Engineers. Seatle, Washington, U.S.A.
40. Rychlik I., Lindgren G., (1995), WAVE Analysis toolbox – a tutorial, Lund University, Department of Mathematical Statistics. Available from: http://www.maths.lth.se/matstat/staff/georg/documents/wattutor.ps
41. Brodtkorb P.A., Johannesson P., Lindgren G., Rychlik I., (2011). Tutorial for WAFO version 2.5. Lund University. Available from: http://www.maths.lth.se/matstat/wafo/documentation/wafotutor25.ps
42. Scott N., Hara T., Hwang P.A., Walsh J.E. (2004). Directionality and Crest Length statistics of Steep Waves in Open Ocean Waters. *Journal of Atmospheric and Ocean Technology*. **22**: p. 272-281.
43. Monaldo F. (2000). Measurement of wave crest length and groupiness from spaceborne Synthetic Aperture Radar. The John Hopkins University, Applied physics laboratory. Laurel, Maryland, U.S.A.
44. Gemmrich J., Thomson J., Erick Rogers W., Pleskachevsky A., Lehner S. (2016). Spatial characteristics of ocean surface waves. *Ocean Dynamics*. **66**(8): p. 1025-1035.
45. Luppes R., Bunnik T., Duz B., Helmholt-Kleefsman T., Iwanowski B., Loots E., Veldman A., Wellens P., Wemmenhove R., van der Plas P., van der Heiden H., (2014). MANUAL COMFLOW V3.4.1 [B]. University of Groningen.
46. Kleefsman K.M.T., Fekken G., Veldman A.E.P., Iwanowski B., Buchner B. (2005). A Volume-of-Fluid based simulation method for wave impact problems. *Journal of computational physics*. **206**(1): p. 363-393.
47. Wellens P.R. (2012). Wave Simulation in Truncated Domains for Offshore Applications. Delft University of Technology. Delft, The Netherlands.
48. Veldman A.E.P., Luppes R., Bunnik T., Huijsmans R.H.M., Duz B., Iwanowski B. Wemmenhove R., Borsboom M.J.A., Wellens P.R., van der Heijden H.J.L., van der Plas P. (2011) Extreme Wave Impact on Offshore Platforms and Coastal Constructions. *OMAE2011 30th International Conference on Ocean, Offshore and Arctic Engineering*. ASME. Rotterdam, The Netherlands.
49. Duz B., Huijsmans R.H.M., Wellens P.R., Borsboom M.J.A, Veldman A.E.P. (2011). Towards a General-Purpose Open Boundary Condition for Wave Simulations. *OMAE2011 30th International Conference on Ocean, Offshore and Arctic Engineering*. ASME. Rotterdam, The Netherlands.
50. Wenneker I. Wellens P.R., Gervelas R. (2010). Volume-of-Fluid model ComFLOW simulations of wave impacts on a dike. Coastal engineering proceedings. **1**(32)
51. ComFLOW homepage. Available from: http://www.math.rug.nl/cmnm/Comflow/Comflow
52. Bruinsma N., Paulsen B.T., Jacobsen N.G. (2016). Validation and application of a fully nonlinear numerical wave tank for simulating floating offshore wind turbines. *Ocean Engineering*. **147**: p. 647-658.
53. Morison J. Johnson J. Schaaf S. (1950). The force exerted by surface waves on piles. *Journal of Petroleum Technology*. **2**(05): p. 149-154.
54. Tanis A.H. (2016). A hydro-elastic model for fatigue lifetime assesment of The Ocean Cleanup Barrier. Delft University of Technology. Delft, The Netherlands.
55. Chakrabarti S.K., Tam W.A., Wolbert A.L. (1975). Wave forces on a randomly oriented tube. *Offshore Technology Conference*. Houston, Texas.
56. Dixon A.G., Greated C.A., Salter S.H. (1979). Wave forces on partially submerged cylinders. *Journal of the Waterway, Port, Coastal and Ocean division*. **105**(WW4): p.421-438.
57. Shafiee-Far M. (1997). Hydrodynamic interaction between fluid flow and oscillating slender cylinders. Delft University of Technology. Delft, The Netherlands.

Appendix A – Met-ocean data

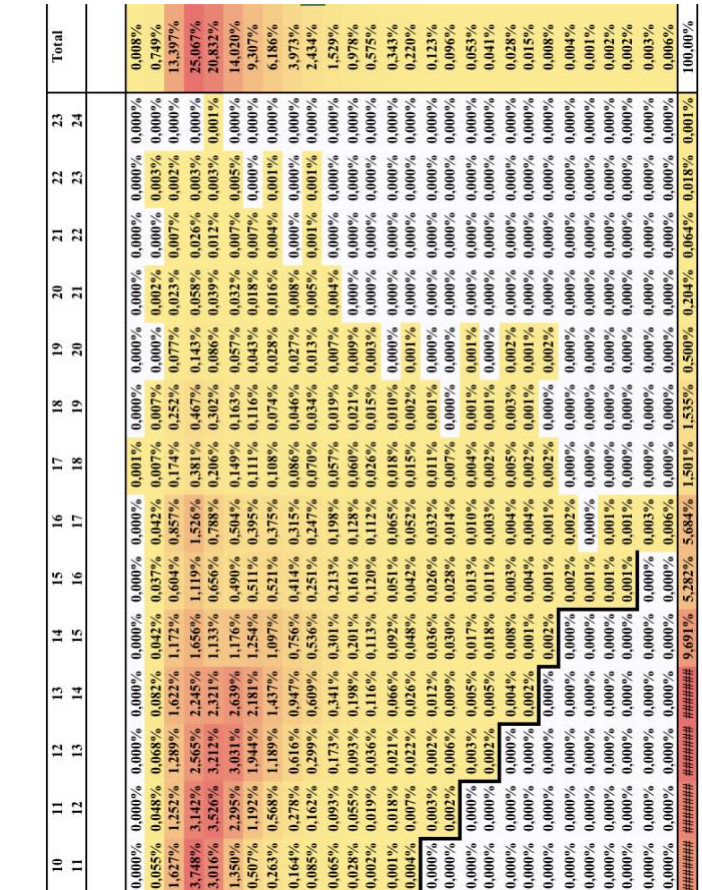

Full wave energy — average Hs = 2.53 m. from hindcast; 2.53 m. from scatter diagram

Tp (s) min	Tp (s) max	Hs (m) min	Hs (m) max	Hs (m) aver	0 1	1 2	2 3	3 4	4 5	5 6	6 7	7 8	8 9	9 10	10 11	11 12	12 13	13 14	14 15	15 16	16 17	17 18	18 19	19 20	20 21	21 22	22 23	23 24	Total
0	0,5	0	0,25		0,000%	0,000%	0,000%	0,006%	0,000%	0,001%	0,000%	0,000%	0,000%	0,000%	0,000%	0,000%	0,000%	0,000%	0,000%	0,000%	0,000%	0,001%	0,000%	0,000%	0,000%	0,000%	0,000%	0,000%	0,008%
0,5	1	0,25	0,75		0,000%	0,000%	0,000%	0,002%	0,026%	0,015%	0,031%	0,081%	0,127%	0,073%	0,055%	0,048%	0,068%	0,082%	0,042%	0,037%	0,042%	0,007%	0,007%	0,000%	0,002%	0,000%	0,003%	0,000%	0,749%
1	1,5	0,75	1,25		0,000%	0,000%	0,000%	0,001%	0,055%	0,115%	0,164%	0,659%	1,482%	1,961%	1,627%	1,252%	1,289%	1,622%	1,172%	0,604%	0,857%	0,174%	0,252%	0,077%	0,023%	0,007%	0,002%	0,000%	13,397%
1,5	2	1,25	1,75		0,000%	0,000%	0,000%	0,000%	0,027%	0,357%	0,708%	0,892%	2,336%	3,669%	3,748%	3,142%	2,565%	2,245%	1,656%	1,119%	1,526%	0,381%	0,467%	0,143%	0,058%	0,026%	0,003%	0,000%	25,067%
2	2,5	1,75	2,25		0,000%	0,000%	0,000%	0,000%	0,001%	0,161%	0,585%	0,997%	1,321%	2,464%	3,016%	3,526%	3,212%	2,321%	1,133%	0,656%	0,788%	0,206%	0,302%	0,086%	0,039%	0,012%	0,003%	0,001%	20,832%
2,5	3	2,25	2,75		0,000%	0,000%	0,000%	0,000%	0,000%	0,022%	0,203%	0,480%	0,580%	0,838%	1,350%	2,295%	3,031%	2,639%	1,176%	0,490%	0,504%	0,149%	0,163%	0,057%	0,032%	0,007%	0,005%	0,000%	14,020%
3	3,5	2,75	3,25		0,000%	0,000%	0,000%	0,000%	0,000%	0,004%	0,060%	0,278%	0,333%	0,351%	0,507%	1,192%	1,944%	2,181%	1,254%	0,511%	0,395%	0,111%	0,116%	0,043%	0,018%	0,007%	0,000%	0,000%	9,307%
3,5	4	3,25	3,75		0,000%	0,000%	0,000%	0,000%	0,000%	0,000%	0,004%	0,137%	0,191%	0,173%	0,263%	0,568%	1,189%	1,437%	1,097%	0,521%	0,375%	0,108%	0,074%	0,028%	0,016%	0,004%	0,001%	0,000%	6,186%
4	4,5	3,75	4,25		0,000%	0,000%	0,000%	0,000%	0,000%	0,000%	0,000%	0,045%	0,136%	0,135%	0,164%	0,278%	0,616%	0,947%	0,756%	0,414%	0,315%	0,086%	0,046%	0,027%	0,008%	0,000%	0,000%	0,000%	3,973%
4,5	5	4,25	4,75		0,000%	0,000%	0,000%	0,000%	0,000%	0,000%	0,000%	0,010%	0,034%	0,075%	0,085%	0,162%	0,299%	0,609%	0,536%	0,251%	0,247%	0,070%	0,034%	0,013%	0,005%	0,001%	0,001%	0,000%	2,434%
5	5,5	4,75	5,25		0,000%	0,000%	0,000%	0,000%	0,000%	0,000%	0,000%	0,000%	0,010%	0,050%	0,065%	0,093%	0,173%	0,341%	0,301%	0,213%	0,198%	0,057%	0,019%	0,007%	0,004%	0,000%	0,000%	0,000%	1,529%
5,5	6	5,25	5,75		0,000%	0,000%	0,000%	0,000%	0,000%	0,000%	0,000%	0,000%	0,005%	0,020%	0,028%	0,055%	0,093%	0,198%	0,201%	0,161%	0,128%	0,060%	0,021%	0,009%	0,000%	0,000%	0,000%	0,000%	0,978%
6	6,5	5,75	6,25		0,000%	0,000%	0,000%	0,000%	0,000%	0,000%	0,000%	0,000%	0,002%	0,010%	0,002%	0,019%	0,036%	0,116%	0,113%	0,120%	0,112%	0,026%	0,015%	0,003%	0,000%	0,000%	0,000%	0,000%	0,575%
6,5	7	6,25	6,75		0,000%	0,000%	0,000%	0,000%	0,000%	0,000%	0,000%	0,000%	0,000%	0,003%	0,001%	0,018%	0,021%	0,066%	0,092%	0,051%	0,065%	0,018%	0,010%	0,000%	0,000%	0,000%	0,000%	0,000%	0,343%
7	7,5	6,75	7,25		0,000%	0,000%	0,000%	0,000%	0,000%	0,000%	0,000%	0,000%	0,000%	0,001%	0,004%	0,007%	0,022%	0,026%	0,048%	0,042%	0,052%	0,015%	0,002%	0,001%	0,000%	0,000%	0,000%	0,000%	0,220%
7,5	8	7,25	7,75		0,000%	0,000%	0,000%	0,000%	0,000%	0,000%	0,000%	0,000%	0,000%	0,000%	0,000%	0,003%	0,002%	0,012%	0,036%	0,026%	0,032%	0,011%	0,001%	0,000%	0,000%	0,000%	0,000%	0,000%	0,123%
8	8,5	7,75	8,25		0,000%	0,000%	0,000%	0,000%	0,000%	0,000%	0,000%	0,000%	0,000%	0,000%	0,000%	0,002%	0,006%	0,009%	0,030%	0,028%	0,014%	0,007%	0,000%	0,000%	0,000%	0,000%	0,000%	0,000%	0,096%
8,5	9	8,25	8,75		0,000%	0,000%	0,000%	0,000%	0,000%	0,000%	0,000%	0,000%	0,000%	0,000%	0,000%	0,000%	0,003%	0,005%	0,017%	0,013%	0,010%	0,004%	0,001%	0,001%	0,000%	0,000%	0,000%	0,000%	0,053%
9	9,5	8,75	9,25		0,000%	0,000%	0,000%	0,000%	0,000%	0,000%	0,000%	0,000%	0,000%	0,000%	0,000%	0,000%	0,002%	0,005%	0,018%	0,011%	0,003%	0,002%	0,001%	0,000%	0,000%	0,000%	0,000%	0,000%	0,041%
9,5	10	9,25	9,75		0,000%	0,000%	0,000%	0,000%	0,000%	0,000%	0,000%	0,000%	0,000%	0,000%	0,000%	0,000%	0,000%	0,004%	0,008%	0,003%	0,004%	0,005%	0,003%	0,002%	0,000%	0,000%	0,000%	0,000%	0,028%
10	10,5	9,75	10,25		0,000%	0,000%	0,000%	0,000%	0,000%	0,000%	0,000%	0,000%	0,000%	0,000%	0,000%	0,000%	0,000%	0,002%	0,001%	0,004%	0,004%	0,002%	0,001%	0,001%	0,000%	0,000%	0,000%	0,000%	0,015%
10,5	11	10,25	10,75		0,000%	0,000%	0,000%	0,000%	0,000%	0,000%	0,000%	0,000%	0,000%	0,000%	0,000%	0,000%	0,000%	0,000%	0,002%	0,001%	0,001%	0,002%	0,000%	0,002%	0,000%	0,000%	0,000%	0,000%	0,008%
11	11,5	10,75	11,25		0,000%	0,000%	0,000%	0,000%	0,000%	0,000%	0,000%	0,000%	0,000%	0,000%	0,000%	0,000%	0,000%	0,000%	0,000%	0,002%	0,002%	0,000%	0,000%	0,000%	0,000%	0,000%	0,000%	0,000%	0,004%
11,5	12	11,25	11,75		0,000%	0,000%	0,000%	0,000%	0,000%	0,000%	0,000%	0,000%	0,000%	0,000%	0,000%	0,000%	0,000%	0,000%	0,000%	0,001%	0,000%	0,000%	0,000%	0,000%	0,000%	0,000%	0,000%	0,000%	0,001%
12	12,5	11,75	12,25		0,000%	0,000%	0,000%	0,000%	0,000%	0,000%	0,000%	0,000%	0,000%	0,000%	0,000%	0,000%	0,000%	0,000%	0,000%	0,000%	0,000%	0,000%	0,000%	0,000%	0,000%	0,000%	0,000%	0,000%	0,002%
12,5	13	12,25	12,75		0,000%	0,000%	0,000%	0,000%	0,000%	0,000%	0,000%	0,000%	0,000%	0,000%	0,000%	0,000%	0,000%	0,000%	0,000%	0,001%	0,001%	0,000%	0,000%	0,000%	0,000%	0,000%	0,000%	0,000%	0,002%
13	13,5	12,75	13,25		0,000%	0,000%	0,000%	0,000%	0,000%	0,000%	0,000%	0,000%	0,000%	0,000%	0,000%	0,000%	0,000%	0,000%	0,000%	0,000%	0,000%	0,000%	0,000%	0,000%	0,000%	0,000%	0,000%	0,000%	0,003%
13,5	14	13,25	13,75		0,000%	0,000%	0,000%	0,000%	0,000%	0,000%	0,000%	0,000%	0,000%	0,000%	0,000%	0,000%	0,000%	0,000%	0,000%	0,000%	0,000%	0,000%	0,000%	0,000%	0,000%	0,000%	0,000%	0,000%	0,006%
Total					0,000%	0,000%	0,000%	0,009%	0,110%	0,675%	1,755%	3,579%	6,557%	9,823%	########	########	########	########	9,691%	5,282%	5,684%	1,501%	1,535%	0,500%	0,204%	0,064%	0,018%	0,001%	100,00%

Figure 38 Full wave energy scatter plot. Metocean data provided for the location 30°N, 138°W.

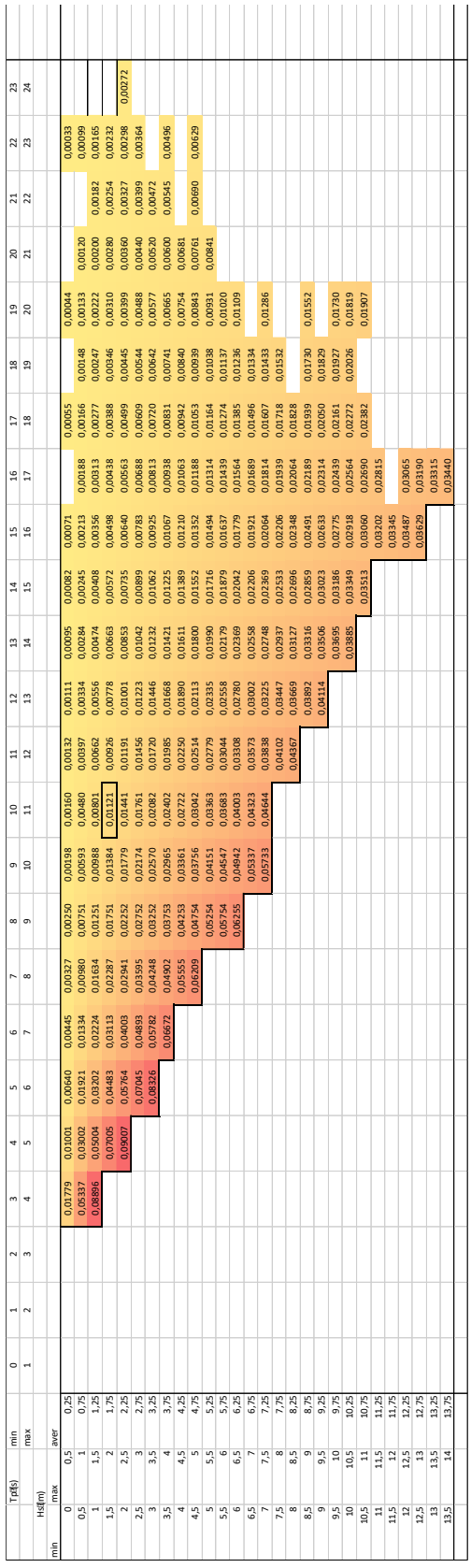

Figure 39 Wave steepness plot for full wave energy scatter plot

Wind sea occurs 49.9% of the time — average Hs = 1.63 — m. from hindcast 1.64 — m. from scatter diagram

Tp (s) min	Tp (s) max	Hs (m) min	Hs (m) max	Hs (m) aver	0 1	1 2	2 3	3 4	4 5	5 6	6 7	7 8	8 9	9 10	10 11	11 12	12 13	13 14	14 15	15 16	16 17	17 18	18 19	19 20	20 21	21 22	22 23	23 24	Total
0	0,5	0	0,25		0,000%	0,000%	0,467%	0,722%	0,725%	0,275%	0,184%	0,106%	0,062%	0,027%	0,015%	0,017%	0,020%	0,009%	0,005%	0,000%	0,000%	0,000%	0,000%	0,000%	0,000%	0,000%	0,000%	0,000%	2,682%
0,5	1	0,5	0,75		0,000%	0,000%	0,061%	1,875%	3,956%	2,324%	1,340%	0,646%	0,259%	0,103%	0,015%	0,011%	0,005%	0,003%	0,003%	0,000%	0,000%	0,000%	0,000%	0,000%	0,000%	0,000%	0,000%	0,000%	10,600%
1	1,5	1,25	1,25		0,000%	0,000%	0,000%	0,024%	3,083%	5,047%	3,561%	1,786%	0,801%	0,203%	0,029%	0,016%	0,004%	0,002%	0,000%	0,000%	0,000%	0,000%	0,000%	0,000%	0,000%	0,000%	0,000%	0,000%	14,557%
1,5	2	1,75			0,000%	0,000%	0,000%	0,000%	0,155%	2,663%	3,519%	2,323%	1,112%	0,475%	0,084%	0,020%	0,005%	0,004%	0,000%	0,000%	0,000%	0,000%	0,000%	0,000%	0,000%	0,000%	0,000%	0,000%	10,360%
2	2,5	2,25			0,000%	0,000%	0,000%	0,000%	0,000%	0,271%	1,351%	1,603%	1,002%	0,584%	0,174%	0,053%	0,012%	0,005%	0,000%	0,000%	0,000%	0,000%	0,000%	0,000%	0,000%	0,000%	0,000%	0,000%	5,054%
2,5	3	2,75			0,000%	0,000%	0,000%	0,000%	0,000%	0,012%	0,358%	0,748%	0,584%	0,381%	0,145%	0,079%	0,048%	0,010%	0,001%	0,000%	0,000%	0,000%	0,000%	0,000%	0,000%	0,000%	0,000%	0,000%	2,365%
3	3,5	3,25			0,000%	0,000%	0,000%	0,000%	0,000%	0,001%	0,038%	0,377%	0,362%	0,259%	0,114%	0,085%	0,074%	0,029%	0,006%	0,001%	0,000%	0,000%	0,000%	0,000%	0,000%	0,000%	0,000%	0,000%	1,347%
3,5	4	3,75			0,000%	0,000%	0,000%	0,000%	0,000%	0,000%	0,000%	0,134%	0,245%	0,168%	0,159%	0,097%	0,072%	0,035%	0,011%	0,000%	0,000%	0,000%	0,001%	0,000%	0,000%	0,000%	0,000%	0,000%	0,923%
4	4,5	4,25			0,000%	0,000%	0,000%	0,000%	0,000%	0,000%	0,000%	0,028%	0,116%	0,109%	0,112%	0,083%	0,079%	0,038%	0,016%	0,003%	0,001%	0,000%	0,000%	0,000%	0,000%	0,000%	0,000%	0,000%	0,586%
4,5	5	4,75			0,000%	0,000%	0,000%	0,000%	0,000%	0,000%	0,000%	0,003%	0,033%	0,053%	0,068%	0,080%	0,050%	0,056%	0,022%	0,005%	0,002%	0,000%	0,000%	0,000%	0,000%	0,000%	0,000%	0,000%	0,372%
5	5,5	5,25			0,000%	0,000%	0,000%	0,000%	0,000%	0,000%	0,000%	0,000%	0,008%	0,052%	0,053%	0,066%	0,057%	0,067%	0,026%	0,006%	0,003%	0,000%	0,000%	0,000%	0,000%	0,000%	0,000%	0,000%	0,338%
5,5	6	5,75			0,000%	0,000%	0,000%	0,000%	0,000%	0,000%	0,000%	0,000%	0,000%	0,011%	0,023%	0,038%	0,038%	0,051%	0,034%	0,019%	0,002%	0,002%	0,000%	0,000%	0,000%	0,000%	0,000%	0,000%	0,218%
6	6,5	6,25			0,000%	0,000%	0,000%	0,000%	0,000%	0,000%	0,000%	0,000%	0,004%	0,006%	0,018%	0,022%	0,037%	0,010%	0,008%	0,005%	0,000%	0,000%	0,001%	0,000%	0,000%	0,000%	0,000%	0,000%	0,110%
6,5	7	6,75			0,000%	0,000%	0,000%	0,000%	0,000%	0,000%	0,000%	0,000%	0,002%	0,002%	0,017%	0,019%	0,033%	0,026%	0,006%	0,005%	0,000%	0,000%	0,000%	0,000%	0,000%	0,000%	0,000%	0,000%	0,110%
7	7,5	7,25			0,000%	0,000%	0,000%	0,000%	0,000%	0,000%	0,000%	0,000%	0,001%	0,002%	0,007%	0,020%	0,021%	0,013%	0,014%	0,005%	0,002%	0,000%	0,000%	0,000%	0,000%	0,000%	0,000%	0,000%	0,083%
7,5	8	7,75			0,000%	0,000%	0,000%	0,000%	0,000%	0,000%	0,000%	0,000%	0,000%	0,000%	0,002%	0,009%	0,002%	0,022%	0,008%	0,011%	0,001%	0,000%	0,000%	0,000%	0,000%	0,000%	0,000%	0,000%	0,055%
8	8,5	8,25			0,000%	0,000%	0,000%	0,000%	0,000%	0,000%	0,000%	0,000%	0,000%	0,000%	0,002%	0,005%	0,009%	0,022%	0,012%	0,002%	0,000%	0,000%	0,000%	0,000%	0,000%	0,000%	0,000%	0,000%	0,051%
8,5	9	8,75			0,000%	0,000%	0,000%	0,000%	0,000%	0,000%	0,000%	0,000%	0,000%	0,000%	0,000%	0,003%	0,005%	0,014%	0,002%	0,000%	0,000%	0,000%	0,000%	0,000%	0,000%	0,000%	0,000%	0,000%	0,023%
9	9,5	9,25			0,000%	0,000%	0,000%	0,000%	0,000%	0,000%	0,000%	0,000%	0,000%	0,000%	0,000%	0,002%	0,005%	0,017%	0,005%	0,000%	0,000%	0,000%	0,001%	0,000%	0,000%	0,000%	0,000%	0,000%	0,029%
9,5	10	9,75			0,000%	0,000%	0,000%	0,000%	0,000%	0,000%	0,000%	0,000%	0,000%	0,000%	0,000%	0,000%	0,000%	0,004%	0,005%	0,004%	0,000%	0,001%	0,001%	0,000%	0,000%	0,000%	0,000%	0,000%	0,015%
10	10,5	10,25			0,000%	0,000%	0,000%	0,000%	0,000%	0,000%	0,000%	0,000%	0,000%	0,000%	0,000%	0,000%	0,002%	0,001%	0,002%	0,001%	0,000%	0,000%	0,000%	0,000%	0,000%	0,000%	0,000%	0,000%	0,007%
10,5	11	10,75			0,000%	0,000%	0,000%	0,000%	0,000%	0,000%	0,000%	0,000%	0,000%	0,000%	0,000%	0,000%	0,000%	0,000%	0,000%	0,000%	0,000%	0,000%	0,000%	0,000%	0,000%	0,000%	0,000%	0,000%	0,006%
11	11,5	11,25			0,000%	0,000%	0,000%	0,000%	0,000%	0,000%	0,000%	0,000%	0,000%	0,000%	0,000%	0,000%	0,000%	0,000%	0,000%	0,000%	0,000%	0,000%	0,000%	0,000%	0,000%	0,000%	0,000%	0,000%	0,002%
11,5	12	11,75			0,000%	0,000%	0,000%	0,000%	0,000%	0,000%	0,000%	0,000%	0,000%	0,000%	0,000%	0,000%	0,000%	0,000%	0,000%	0,000%	0,000%	0,000%	0,000%	0,000%	0,000%	0,000%	0,000%	0,000%	0,001%
12	12,5	12,25			0,000%	0,000%	0,000%	0,000%	0,000%	0,000%	0,000%	0,000%	0,000%	0,000%	0,000%	0,000%	0,000%	0,000%	0,000%	0,000%	0,000%	0,000%	0,000%	0,000%	0,000%	0,000%	0,000%	0,000%	0,002%
12,5	13	12,75			0,000%	0,000%	0,000%	0,000%	0,000%	0,000%	0,000%	0,000%	0,000%	0,000%	0,000%	0,000%	0,000%	0,000%	0,000%	0,000%	0,000%	0,000%	0,000%	0,000%	0,000%	0,000%	0,000%	0,000%	0,002%
13	13,5	13,25			0,000%	0,000%	0,000%	0,000%	0,000%	0,000%	0,000%	0,000%	0,000%	0,000%	0,000%	0,000%	0,000%	0,000%	0,000%	0,000%	0,000%	0,000%	0,000%	0,000%	0,000%	0,000%	0,000%	0,000%	0,003%
13,5	14	13,75			0,000%	0,000%	0,000%	0,000%	0,000%	0,000%	0,000%	0,000%	0,000%	0,000%	0,000%	0,000%	0,000%	0,000%	0,000%	0,000%	0,000%	0,000%	0,000%	0,000%	0,000%	0,000%	0,000%	0,000%	0,006%
Total					0,000%	0,000%	0,528%	2,672%	7,919%	########	########	7,755%	4,584%	2,432%	1,002%	0,690%	0,536%	0,433%	0,253%	0,099%	0,048%	0,009%	0,004%	0,000%	0,000%	0,000%	0,000%	0,000%	0,000%	49,91%

Figure 40 Wind sea scatter plot. Metocean data provided for the location 30°N, 138°W.

Swell occurs 99.6% of the time — average Hs = 1.81 — m. from hindcast 1.82 — m. from scatter diagram

Tp (s) min	Tp (s) max	Hs (m) min	Hs (m) max	Hs (m) aver	0 1	1 2	2 3	3 4	4 5	5 6	6 7	7 8	8 9	9 10	10 11	11 12	12 13	13 14	14 15	15 16	16 17	17 18	18 19	19 20	20 21	21 22	22 23	23 24	Total
0	0,5	0	0,25		0,000%	0,000%	0,000%	0,000%	0,007%	0,025%	0,083%	0,226%	0,444%	0,610%	0,271%	0,267%	0,464%	0,478%	0,293%	0,206%	0,192%	0,047%	0,043%	0,009%	0,007%	0,004%	0,007%	0,002%	3,685%
0,5	1	0,5	0,75		0,000%	0,000%	0,000%	0,000%	0,047%	0,291%	1,173%	2,455%	3,069%	4,414%	3,918%	2,223%	1,903%	2,255%	1,728%	1,055%	1,024%	0,303%	0,276%	0,079%	0,021%	0,005%	0,003%	0,001%	26,242%
1	1,5	1,25			0,000%	0,000%	0,000%	0,000%	0,003%	0,090%	0,619%	1,807%	2,848%	3,352%	3,736%	3,189%	2,111%	1,098%	0,598%	0,532%	0,589%	0,154%	0,100%	0,032%	0,015%	0,004%	0,001%	0,000%	20,877%
1,5	2	1,75			0,000%	0,000%	0,000%	0,000%	0,000%	0,002%	0,095%	0,459%	1,340%	2,221%	2,532%	2,858%	2,578%	1,644%	0,603%	0,287%	0,263%	0,059%	0,069%	0,026%	0,009%	0,001%	0,000%	0,000%	15,046%
2	2,5	2,25			0,000%	0,000%	0,000%	0,000%	0,000%	0,000%	0,016%	0,114%	0,303%	0,994%	1,574%	2,102%	2,280%	1,942%	0,830%	0,332%	0,231%	0,076%	0,075%	0,021%	0,008%	0,001%	0,000%	0,000%	10,900%
2,5	3	2,75			0,000%	0,000%	0,000%	0,000%	0,000%	0,000%	0,002%	0,034%	0,054%	0,239%	0,620%	1,337%	1,784%	1,750%	0,918%	0,353%	0,228%	0,079%	0,055%	0,018%	0,009%	0,001%	0,000%	0,000%	7,480%
3	3,5	3,25			0,000%	0,000%	0,000%	0,000%	0,000%	0,000%	0,000%	0,005%	0,015%	0,057%	0,202%	0,682%	1,298%	1,491%	0,901%	0,378%	0,257%	0,052%	0,024%	0,010%	0,004%	0,000%	0,000%	0,000%	5,377%
3,5	4	3,75			0,000%	0,000%	0,000%	0,000%	0,000%	0,000%	0,000%	0,012%	0,022%	0,055%	0,311%	0,775%	1,043%	0,730%	0,388%	0,240%	0,046%	0,028%	0,007%	0,000%	0,000%	0,000%	0,000%	0,000%	3,657%
4	4,5	4,25			0,000%	0,000%	0,000%	0,000%	0,000%	0,000%	0,000%	0,002%	0,004%	0,022%	0,127%	0,396%	0,721%	0,568%	0,252%	0,219%	0,059%	0,022%	0,002%	0,001%	0,000%	0,000%	0,000%	0,000%	2,395%
4,5	5	4,75			0,000%	0,000%	0,000%	0,000%	0,000%	0,000%	0,000%	0,000%	0,004%	0,009%	0,047%	0,181%	0,417%	0,412%	0,203%	0,210%	0,057%	0,009%	0,005%	0,000%	0,000%	0,000%	0,000%	0,000%	1,553%
5	5,5	5,25			0,000%	0,000%	0,000%	0,000%	0,000%	0,000%	0,000%	0,000%	0,003%	0,002%	0,022%	0,083%	0,231%	0,235%	0,183%	0,125%	0,040%	0,011%	0,003%	0,000%	0,000%	0,000%	0,000%	0,000%	0,937%
5,5	6	5,75			0,000%	0,000%	0,000%	0,000%	0,000%	0,000%	0,000%	0,000%	0,000%	0,001%	0,006%	0,026%	0,101%	0,131%	0,131%	0,110%	0,043%	0,007%	0,003%	0,000%	0,000%	0,000%	0,000%	0,000%	0,559%
6	6,5	6,25			0,000%	0,000%	0,000%	0,000%	0,000%	0,000%	0,000%	0,000%	0,000%	0,000%	0,000%	0,006%	0,066%	0,083%	0,101%	0,099%	0,020%	0,010%	0,003%	0,000%	0,000%	0,000%	0,000%	0,000%	0,386%
6,5	7	6,75			0,000%	0,000%	0,000%	0,000%	0,000%	0,000%	0,000%	0,000%	0,002%	0,002%	0,028%	0,054%	0,041%	0,055%	0,012%	0,008%	0,000%	0,000%	0,000%	0,000%	0,000%	0,000%	0,000%	0,000%	0,199%
7	7,5	7,25			0,000%	0,000%	0,000%	0,000%	0,000%	0,000%	0,000%	0,000%	0,000%	0,000%	0,000%	0,001%	0,005%	0,034%	0,024%	0,041%	0,012%	0,001%	0,001%	0,000%	0,000%	0,000%	0,000%	0,000%	0,119%
7,5	8	7,75			0,000%	0,000%	0,000%	0,000%	0,000%	0,000%	0,000%	0,000%	0,000%	0,000%	0,000%	0,000%	0,001%	0,018%	0,018%	0,021%	0,011%	0,001%	0,001%	0,000%	0,000%	0,000%	0,000%	0,000%	0,068%
8	8,5	8,25			0,000%	0,000%	0,000%	0,000%	0,000%	0,000%	0,000%	0,000%	0,000%	0,000%	0,000%	0,000%	0,000%	0,005%	0,018%	0,013%	0,006%	0,000%	0,000%	0,001%	0,000%	0,000%	0,000%	0,000%	0,042%
8,5	9	8,75			0,000%	0,000%	0,000%	0,000%	0,000%	0,000%	0,000%	0,000%	0,000%	0,000%	0,000%	0,000%	0,000%	0,004%	0,009%	0,009%	0,004%	0,001%	0,001%	0,001%	0,000%	0,000%	0,000%	0,000%	0,027%
9	9,5	9,25			0,000%	0,000%	0,000%	0,000%	0,000%	0,000%	0,000%	0,000%	0,000%	0,000%	0,000%	0,000%	0,000%	0,001%	0,006%	0,003%	0,001%	0,000%	0,000%	0,000%	0,000%	0,000%	0,000%	0,000%	0,011%
9,5	10	9,75			0,000%	0,000%	0,000%	0,000%	0,000%	0,000%	0,000%	0,000%	0,000%	0,000%	0,000%	0,000%	0,000%	0,002%	0,001%	0,003%	0,004%	0,002%	0,001%	0,000%	0,000%	0,000%	0,000%	0,000%	0,013%
10	10,5	10,25			0,000%	0,000%	0,000%	0,000%	0,000%	0,000%	0,000%	0,000%	0,000%	0,000%	0,000%	0,000%	0,000%	0,000%	0,000%	0,001%	0,003%	0,001%	0,001%	0,001%	0,000%	0,000%	0,000%	0,000%	0,007%
10,5	11	10,75			0,000%	0,000%	0,000%	0,000%	0,000%	0,000%	0,000%	0,000%	0,000%	0,000%	0,000%	0,000%	0,000%	0,000%	0,000%	0,000%	0,000%	0,000%	0,000%	0,002%	0,000%	0,000%	0,000%	0,000%	0,002%
11	11,5	11,25			0,000%	0,000%	0,000%	0,000%	0,000%	0,000%	0,000%	0,000%	0,000%	0,000%	0,000%	0,000%	0,000%	0,000%	0,000%	0,000%	0,002%	0,000%	0,000%	0,000%	0,000%	0,000%	0,000%	0,000%	0,002%
11,5	12	11,75			0,000%	0,000%	0,000%	0,000%	0,000%	0,000%	0,000%	0,000%	0,000%	0,000%	0,000%	0,000%	0,000%	0,000%	0,000%	0,000%	0,000%	0,000%	0,000%	0,000%	0,000%	0,000%	0,000%	0,000%	0,000%
12	12,5	12,25			0,000%	0,000%	0,000%	0,000%	0,000%	0,000%	0,000%	0,000%	0,000%	0,000%	0,000%	0,000%	0,000%	0,000%	0,000%	0,000%	0,000%	0,000%	0,000%	0,000%	0,000%	0,000%	0,000%	0,000%	0,000%
12,5	13	12,75			0,000%	0,000%	0,000%	0,000%	0,000%	0,000%	0,000%	0,000%	0,000%	0,000%	0,000%	0,000%	0,000%	0,000%	0,000%	0,000%	0,000%	0,000%	0,000%	0,000%	0,000%	0,000%	0,000%	0,000%	0,000%
13	13,5	13,25			0,000%	0,000%	0,000%	0,000%	0,000%	0,000%	0,000%	0,000%	0,000%	0,000%	0,000%	0,000%	0,000%	0,000%	0,000%	0,000%	0,000%	0,000%	0,000%	0,000%	0,000%	0,000%	0,000%	0,000%	0,000%
13,5	14	13,75			0,000%	0,000%	0,000%	0,000%	0,000%	0,000%	0,000%	0,000%	0,000%	0,000%	0,000%	0,000%	0,000%	0,000%	0,000%	0,000%	0,000%	0,000%	0,000%	0,000%	0,000%	0,000%	0,000%	0,000%	0,000%
Total					0,000%	0,000%	0,000%	0,000%	0,057%	0,409%	1,988%	5,100%	8,086%	########	########	########	########	8,148%	4,520%	3,935%	1,083%	0,742%	0,234%	0,072%	0,016%	0,011%	0,003%	99,58%

Figure 41 Swell sea scatter plot. Metocean data provided for the location 30°N, 138°W.

Appendix B – Morison's approach

In 1950, Morison [53] studied wave forcing on a vertical pile. He hypothesized that the horizontal wave force exerted on the pile consists of a superposition of a linear inertia term and a quadratic drag term:

$$F(t) = \underbrace{C_m \rho V \dot{u}(t)}_{Inertia\ term} + \underbrace{\frac{1}{2} C_d \rho A u(t)|u(t)|}_{Drag\ force} \tag{84}$$

With $F(t)$ the excitation force, C_m inertia coefficient, C_d drag coefficient, ρ mass density, V submerged volume, A frontal area, u water particle velocity, $\dot{u}$ water particle acceleration.
The inertia coefficient C_m and the drag coefficient C_d are dependent on the Reynolds number, Keulegan-Carpenter number, roughness and the geometry of the cylinder. Derivation of these coefficients for the boom is handled in [54].
Chakrabarti [22, 55] generalized Morison's equation to cylinders of random orientation. While Dixon [56] extended the formulae to the application of a partially submerged horizontal cylinder in waves. He mentioned that due to the varying immersion of the cylinder, the vertical force equation now has to account for the varying buoyancy. The varying buoyancy term is proportional to the displacement volume change.
The vertical component of the wave exciting force of a partially submerged horizontal cylinder is now written as:

$$F_z(t) = \underbrace{C_m \rho V \dot{u}(t)}_{Inertia\ term} + \underbrace{\frac{1}{2} C_d \rho A u(t)|\underline{w}(t)|}_{Drag\ term} + \underbrace{\rho g [V(t) - V_0]}_{Buoyancy\ term} \tag{85}$$

where, $F_z(t)$ vertical excitation force, $\underline{w}(t)$ normal velocity vector, $V(t)$ immersed volume at time t and V_0 initial immersed volume.
The initial Morison's equation considers a cylinder restrained in waves. Shafiee-Far's extension of the Morison formula [57] accounts for a moving structure:

$$F(t) = \underbrace{C_m \rho V \dot{u}_w(t) - C_a \rho V \dot{u}_s(t)}_{inertia\ term} + \underbrace{\frac{1}{2} C_d \rho A u_r(t)|u_r(t)|}_{Drag\ term} \tag{86}$$

Where the inertia coefficient is defined as $C_m = C_a + 1$ with C_a being the added mass coefficient. Now, Tanis [54] combined the equations 85 and 86 into extended Morison formulae for the application of a moving horizontal cylinder in waves. The wave exciting force in heave and surge direction are given as:

$$F_z(t) = \underbrace{C_m \rho V \dot{u}_w(t) - C_a \rho V \dot{u}_s(t)}_{inertia\ term} + \underbrace{\frac{1}{2} C_d \rho A u_r(t)|u_r(t)|}_{Drag\ term} + \underbrace{\rho g [V(t) - V_0]}_{Buoyancy\ term} \tag{87}$$

$$F_x(t) = \underbrace{C_m \rho V \dot{u}_w(t) - C_a \rho V \dot{u}_s(t)}_{inertia\ term} + \underbrace{\frac{1}{2} C_d \rho A u_r(t)|u_r(t)|}_{Drag\ term} \tag{88}$$

Appendix C – Conditions for oscillating cylinder in heave

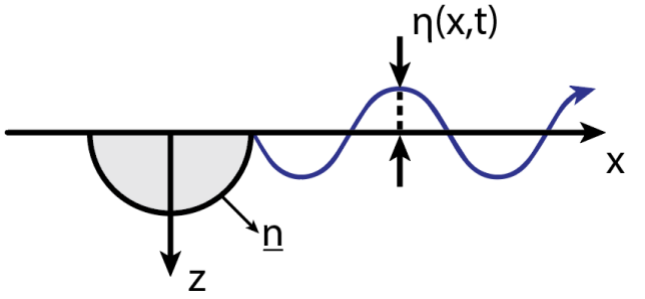

Figure 42 – Formulation of problem

Consider the half submerged cylinder from Figure 42. Assume that the position of the center corresponds with the free surface of the undisturbed fluid. Now, the velocity potential function ϕ has to satisfy the following conditions:

1. La Place condition:

$$\frac{\partial \phi^2}{\partial x^2} + \frac{\partial \phi^2}{\partial z^2} = 0 \tag{89}$$

2. Linearized free surface condition:

$$K\phi + \frac{\partial \phi}{\partial z} = 0 \tag{90}$$

with $K = \frac{\sigma^2}{g}$ with $\sigma = \frac{2\pi}{T} = heave\ freq.$

3. Sea bed boundary condition (deep water):

$$\frac{\partial \phi}{\partial z} = 0 \text{ for } z \to \infty \tag{91}$$

4. Boundary condition on cylinder:

$$\frac{\partial \phi}{\partial n} = U_n(x, z) \tag{92}$$

5. Radiation condition:

$$\lim_{R \to \infty} \phi = 0 \tag{93}$$

6. symmetric condition (case of heave):

$$\phi(-x, y) = \phi(x, y) \tag{94}$$

Appendix D – Added mass and hydrodynamic damping coefficients for a partially submerged circular cross-section with a diameter of 1.2m and a draft of 0.34m

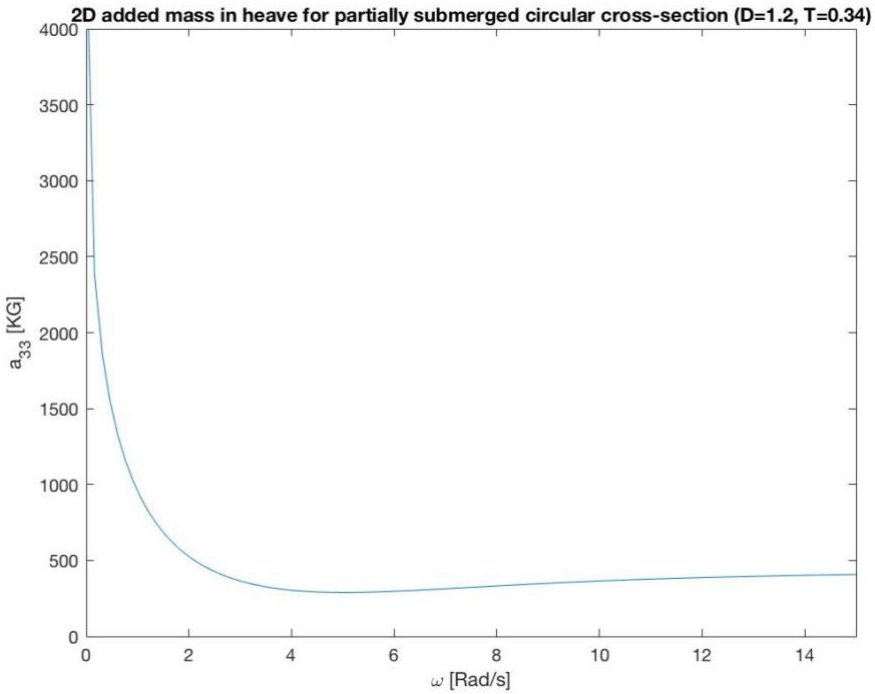

Figure 43 Two-dimensional added mass coefficient in heave a_{33} for a partially submerged circular cross-section with a diameter of 1.2m and a draft of 0.34m

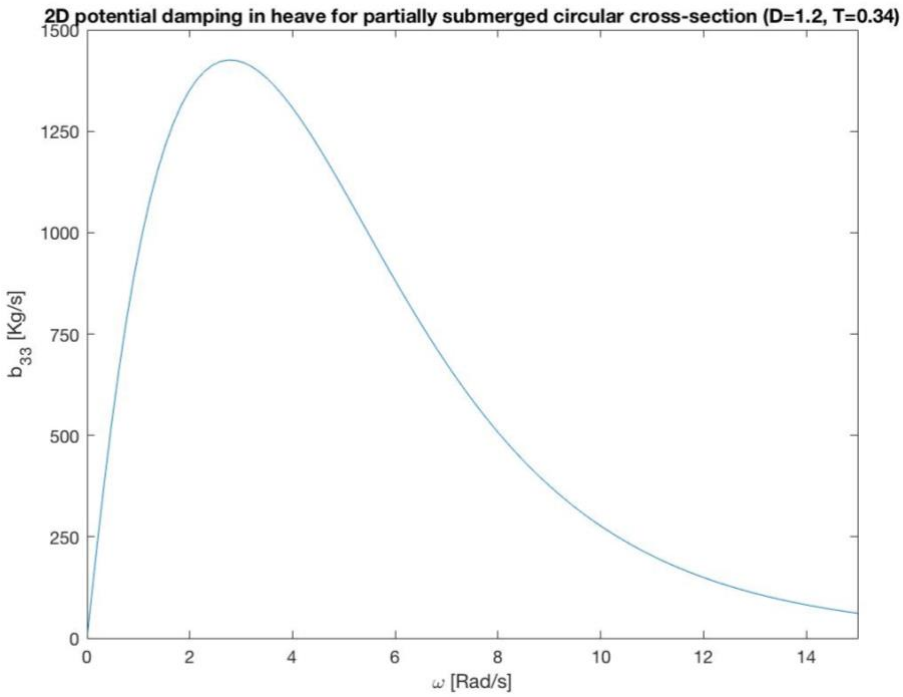

Figure 44 Two-dimensional potential damping coefficient in heave b_{33} for a partially submerged circular cross-section with a diameter of 1.2m and a draft of 0.34m

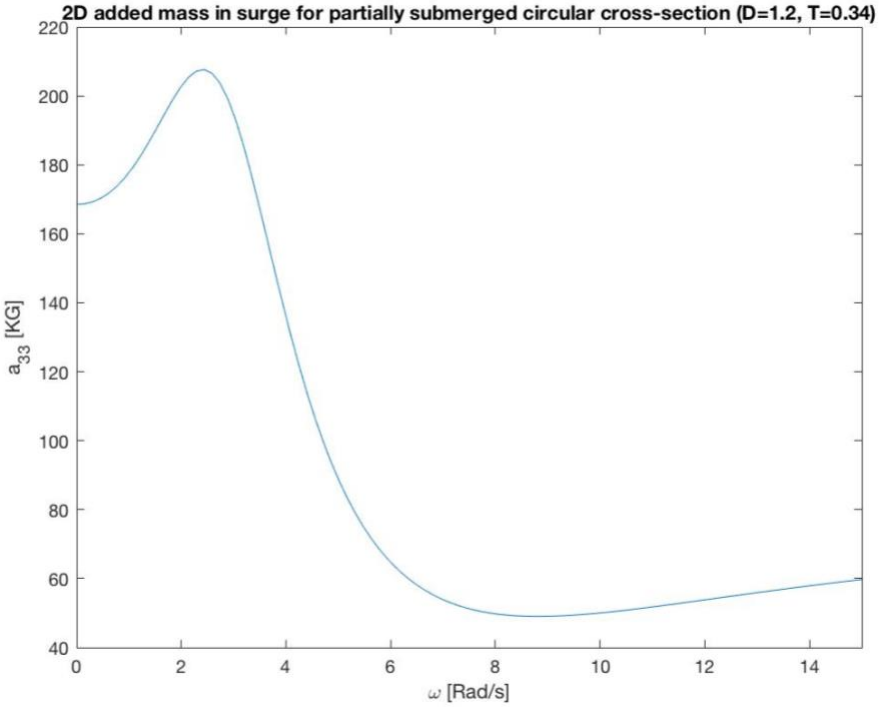

Figure 45 Two-dimensional added mass coefficient in surge a_{11} for a partially submerged circular cross-section with a diameter of 1.2m and a draft of 0.34m

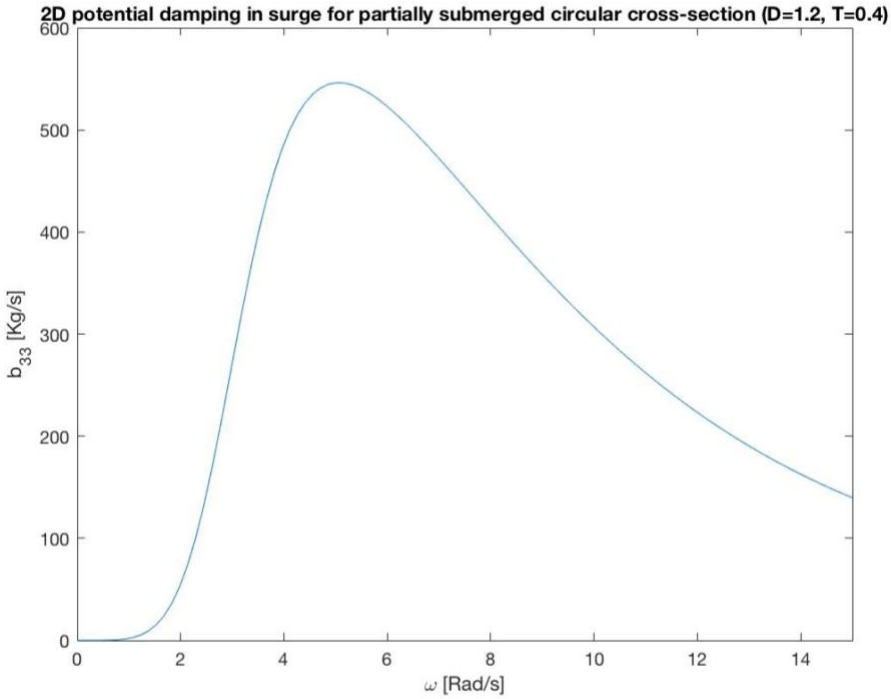

Figure 46 Two-dimensional potential damping coefficient in surge b_{11} for a partially submerged circular cross-section with a diameter of 1.2m and a draft of 0.34m

Appendix E – Response spectra of the floater in the case of Keq = 0 ('Pure hydrodynamic model')

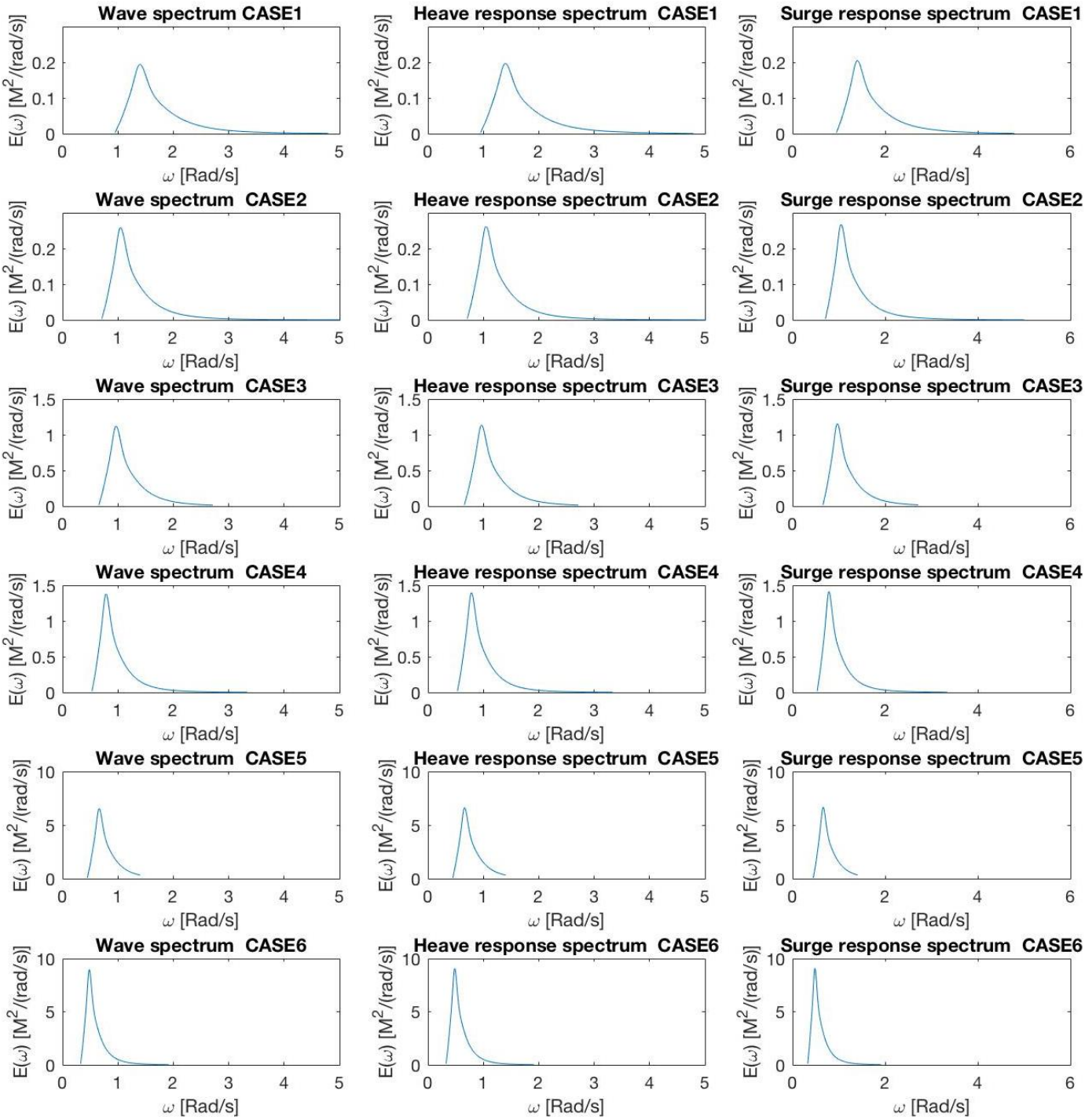

Figure 47 Wave spectrum of the environmental cases and the heave- and surge response spectra for the hydrodynamic model with a spring coefficient of keq=0

Appendix F – Comparison of beam model with FEMAP

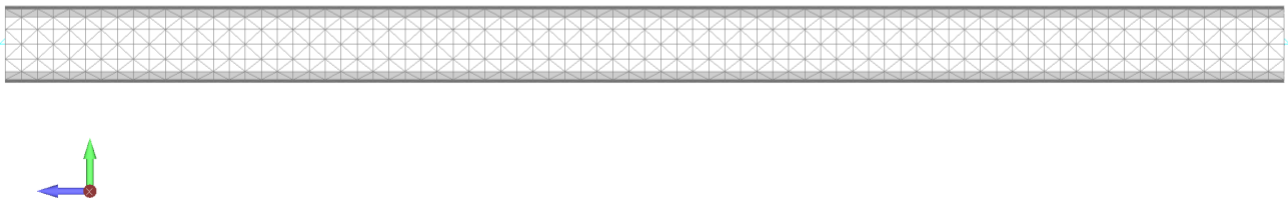

Figure 48 Undeformed comparison model in FEMAP

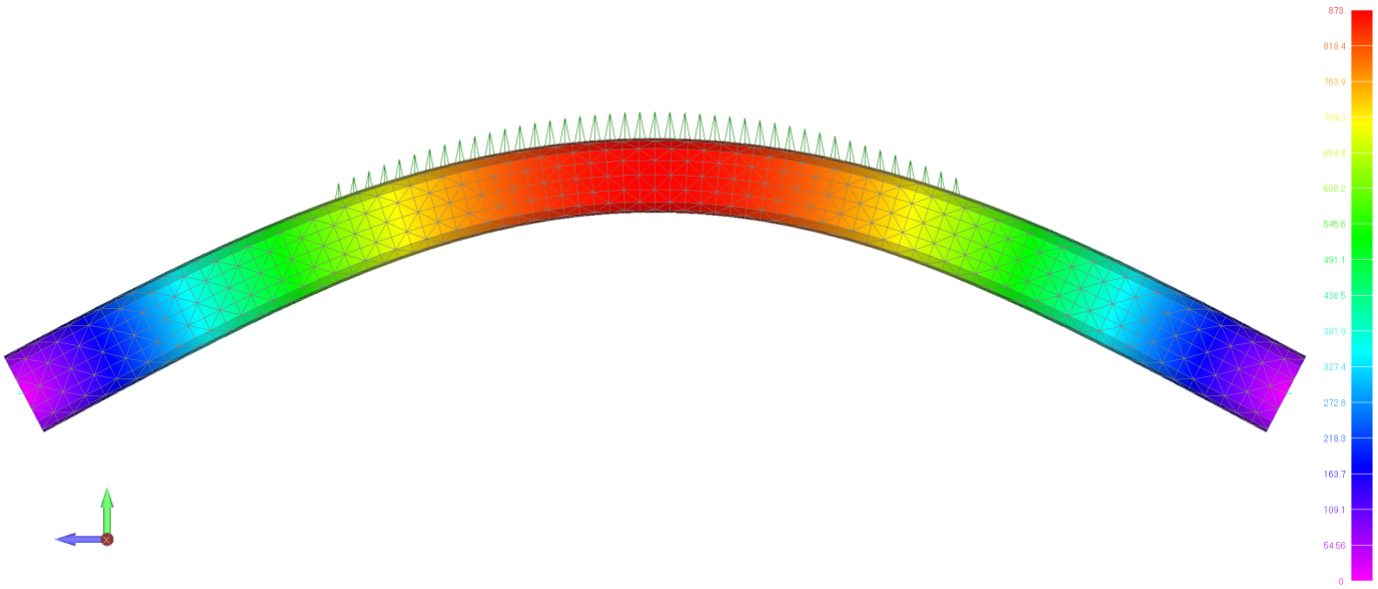

Figure 49 Deformed comparison model in FEMAP

Appendix G – Comparison of 'pure' hydrodynamic model with OrcaFlex

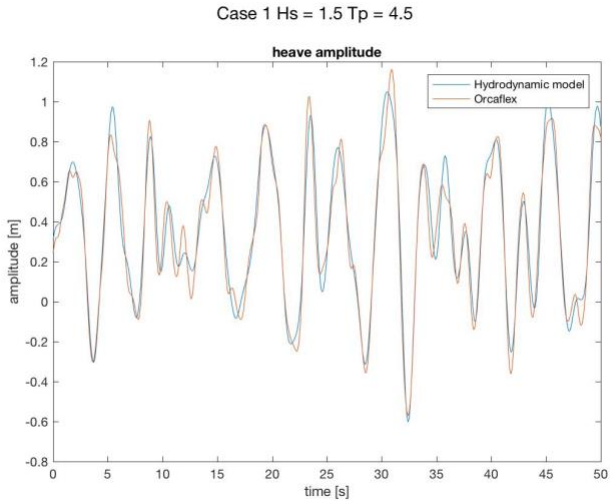

Figure 50 Comparison of heave response in hydrodynamic model and OrcaFlex model for wave case 1

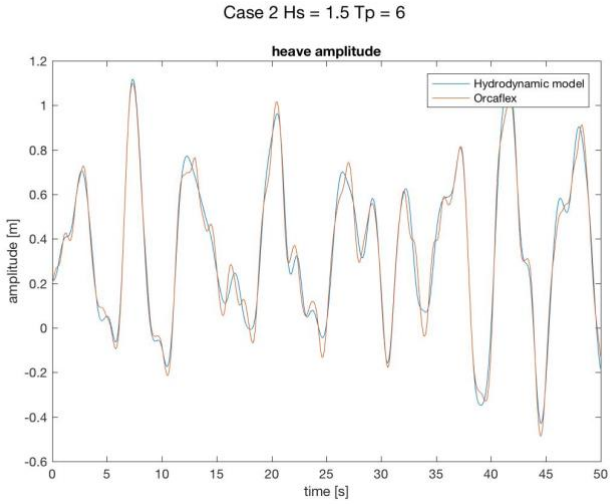

Figure 51 Comparison of heave response in hydrodynamic model and OrcaFlex model for wave case 2

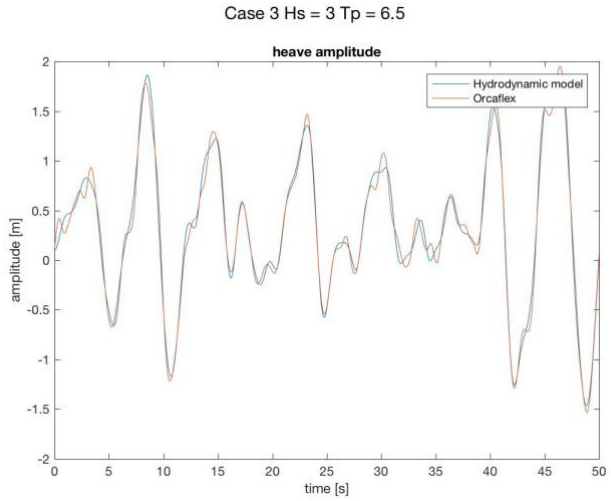

Figure 52 Comparison of heave response in hydrodynamic model and OrcaFlex model for wave case 3

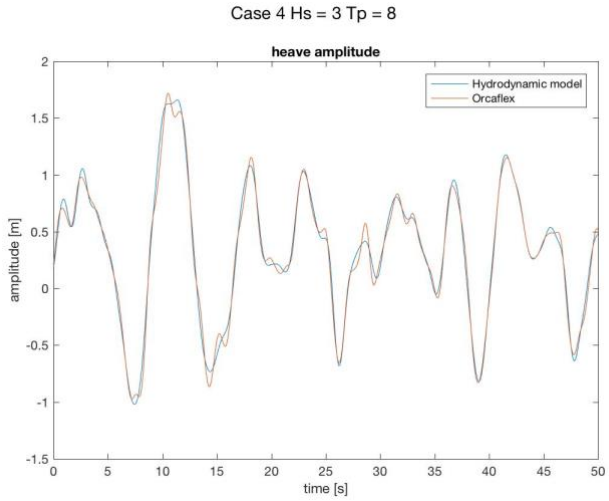

Figure 53 Comparison of heave response in hydrodynamic model and OrcaFlex model for wave case 4

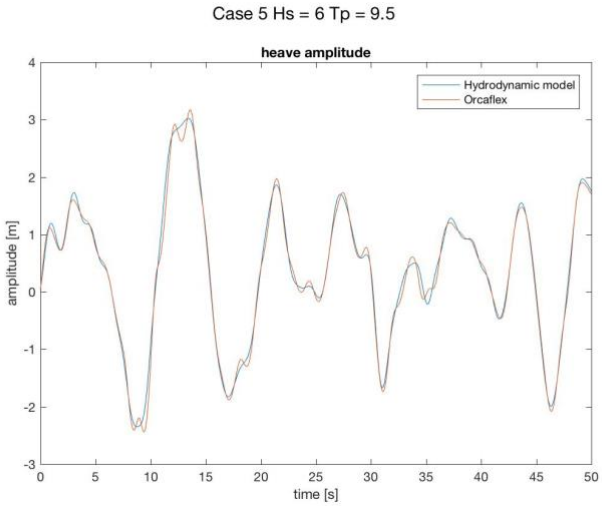

Figure 54 Comparison of heave response in hydrodynamic model and OrcaFlex model for wave case 5

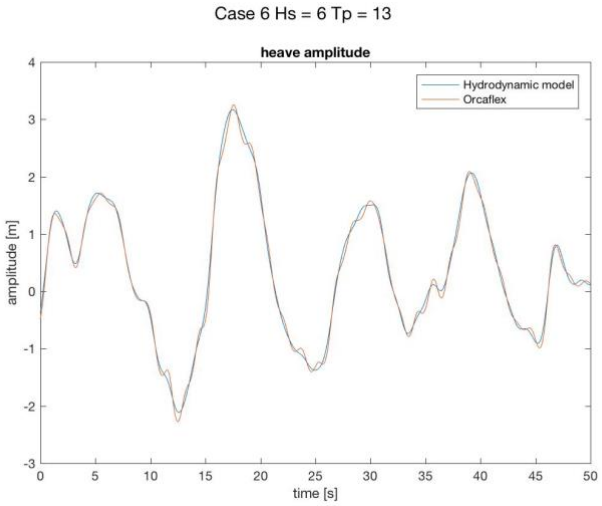

Figure 55 Comparison of heave response in hydrodynamic model and OrcaFlex model for wave case 6

Appendix H – Convergence of the ECDF of crest length measurements

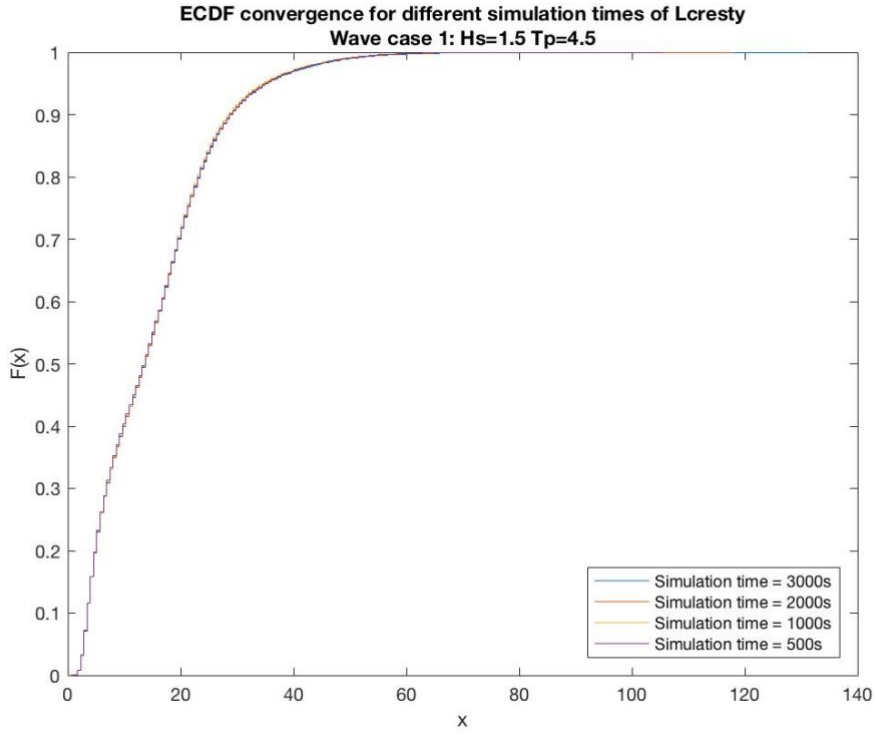

Figure 56 Convergence of ECDF against simulation time

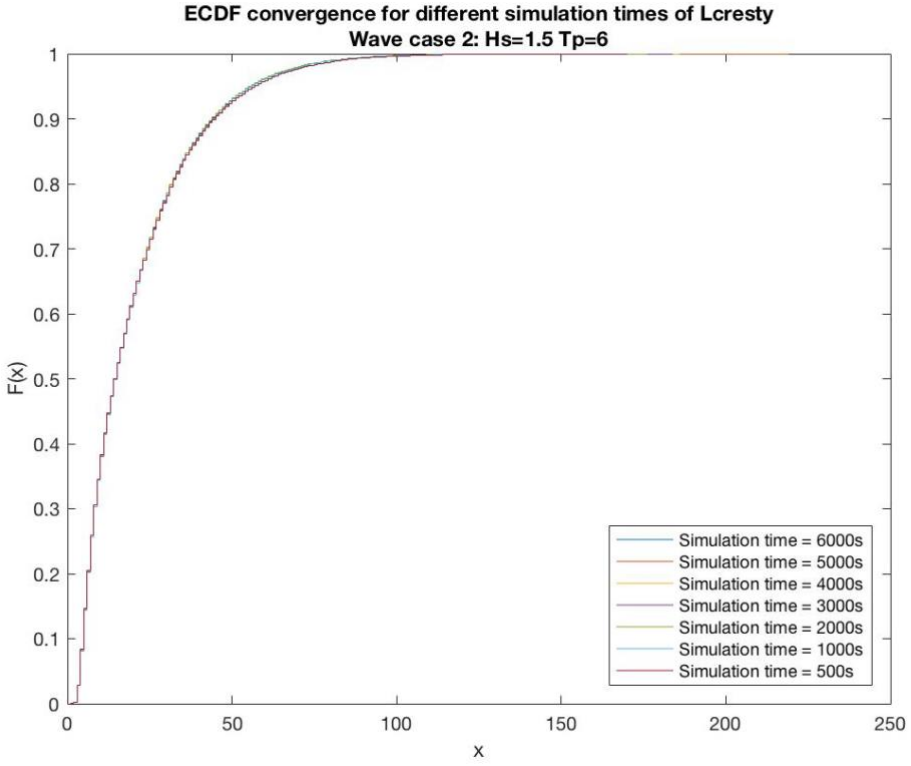

Figure 57 Convergence of ECDF against simulation time

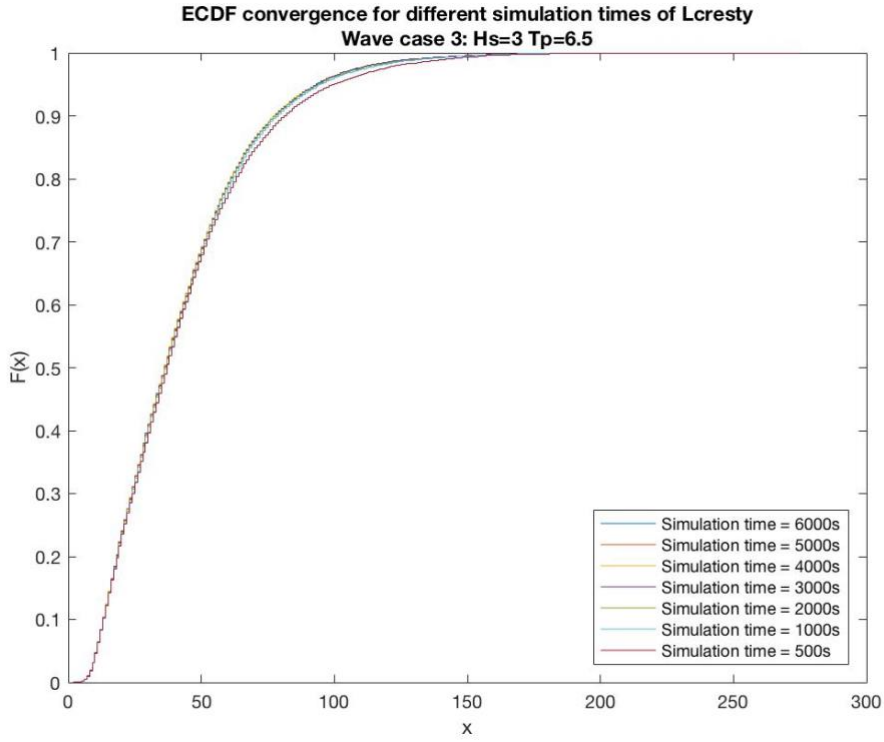

Figure 58 Convergence of ECDF against simulation time

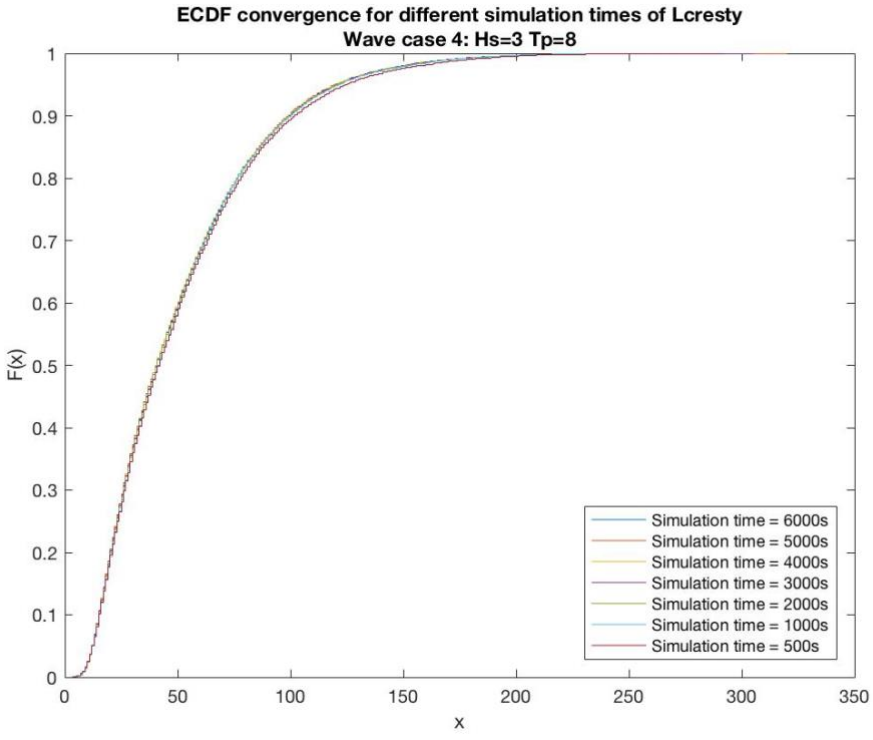

Figure 59 Convergence of ECDF against simulation time

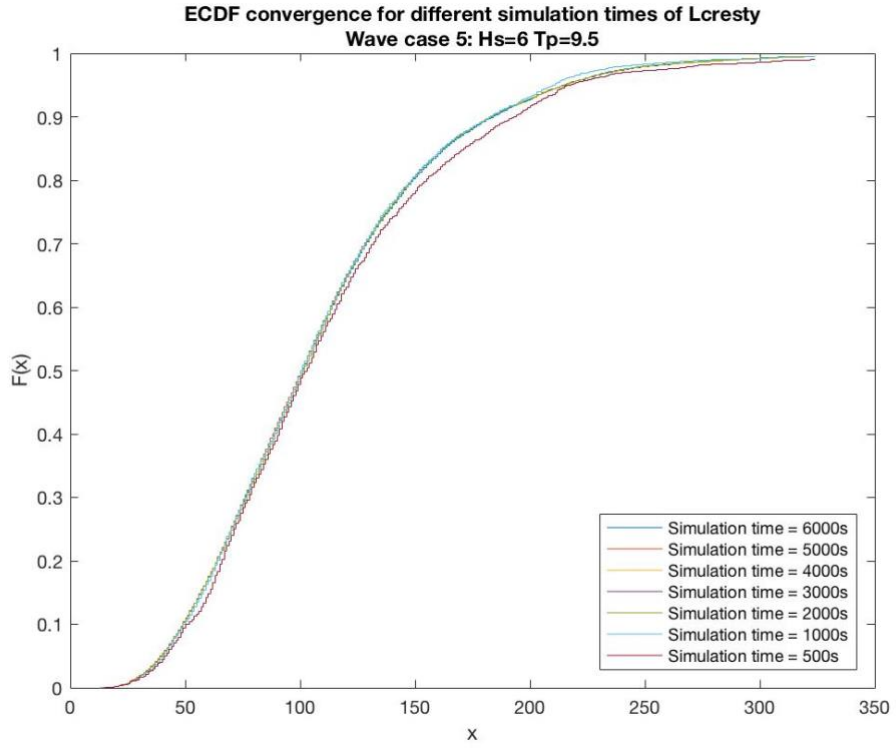

Figure 60 Convergence of ECDF against simulation time

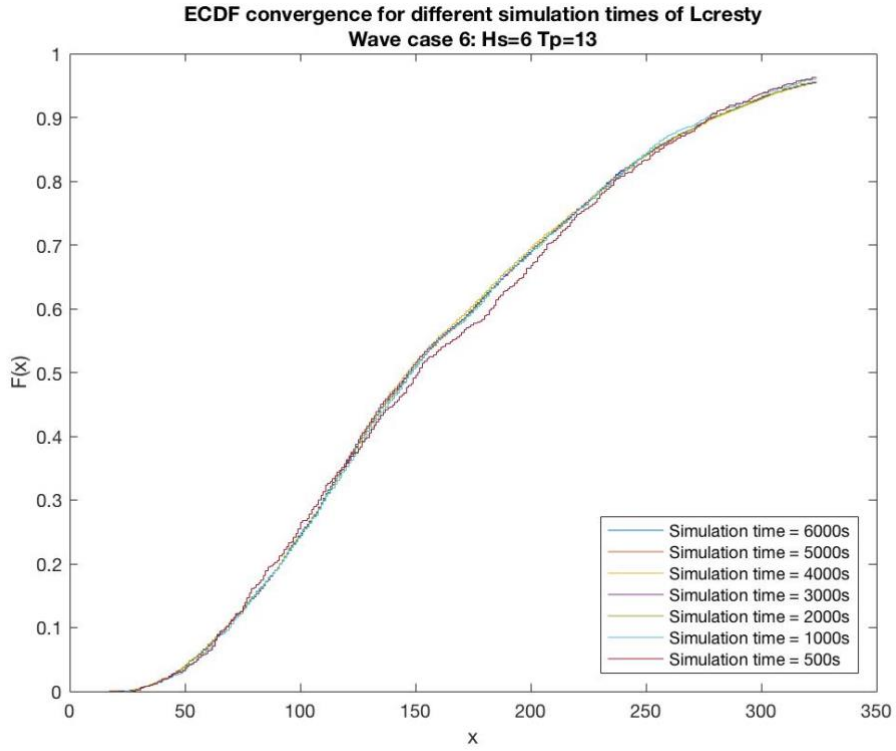

Figure 61 Convergence of ECDF against simulation time

Appendix I – Frequency response characteristics

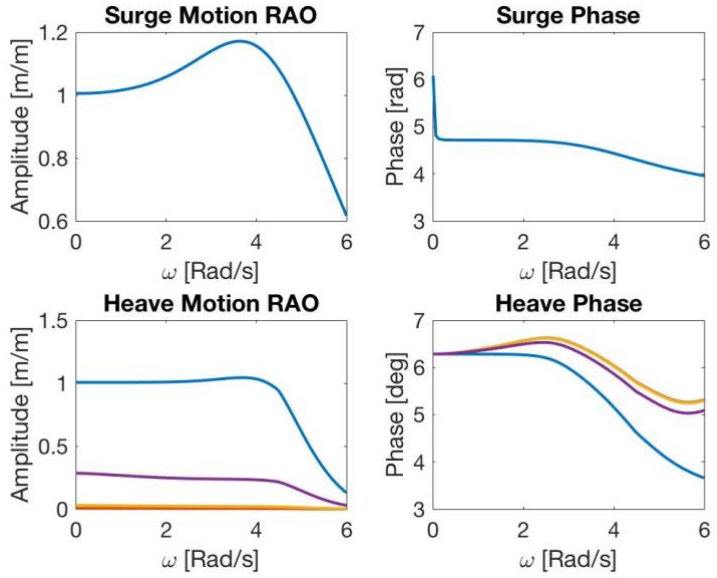

Figure 62 Frequency response characteristics case 1, the blue line indicates K0, the purple line KP050, the yellow line KP020 and the orange line KP005

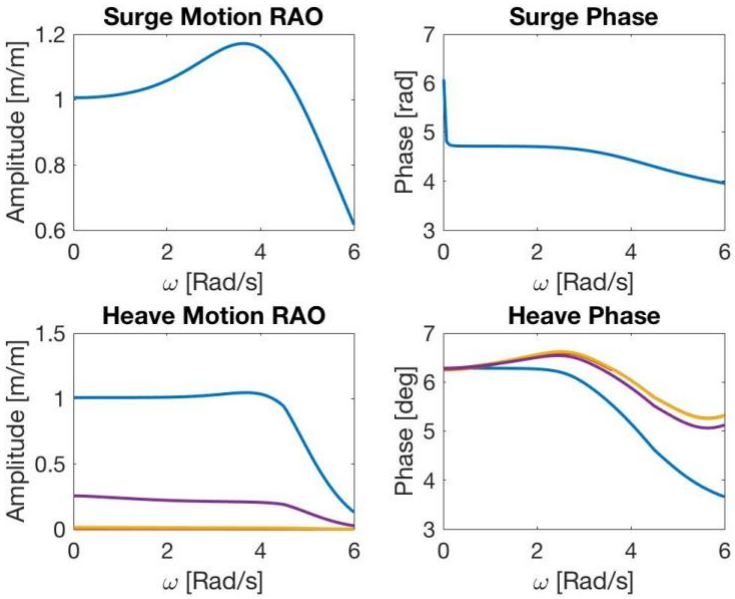

Figure 63 Frequency response characteristics case 2, the blue line indicates K0, the purple line KP050, the yellow line KP020 and the orange line KP005

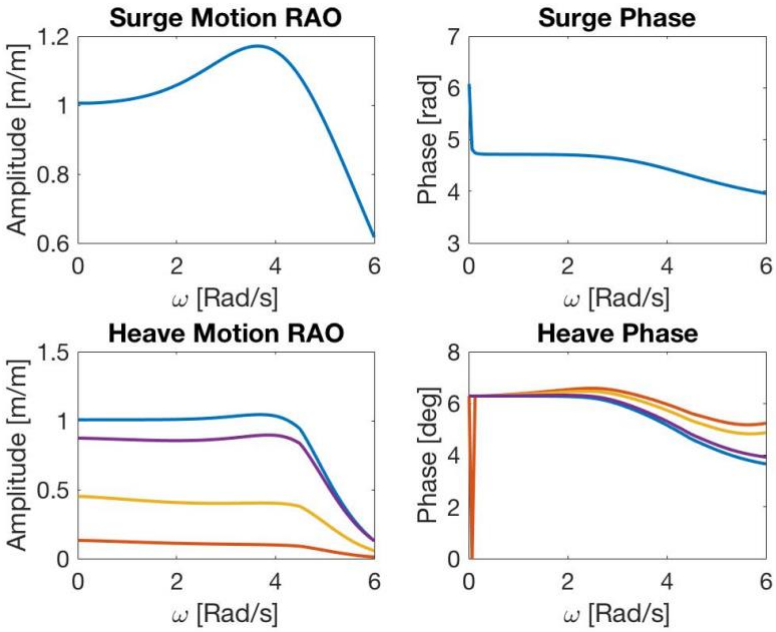

Figure 64 Frequency response characteristics case 3, the blue line indicates K0, the purple line KP050, the yellow line KP020 and the orange line KP005

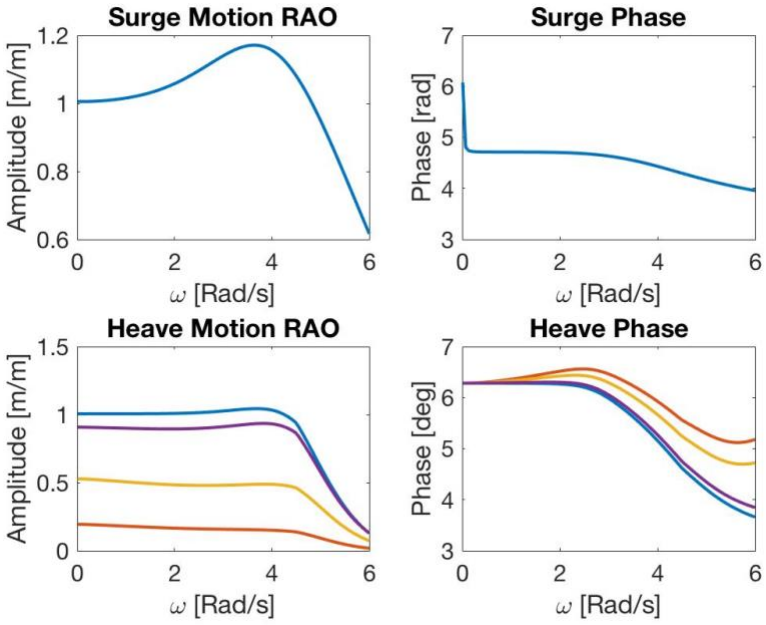

Figure 65 Frequency response characteristics case 4, the blue line indicates K0, the purple line KP050, the yellow line KP020 and the orange line KP005

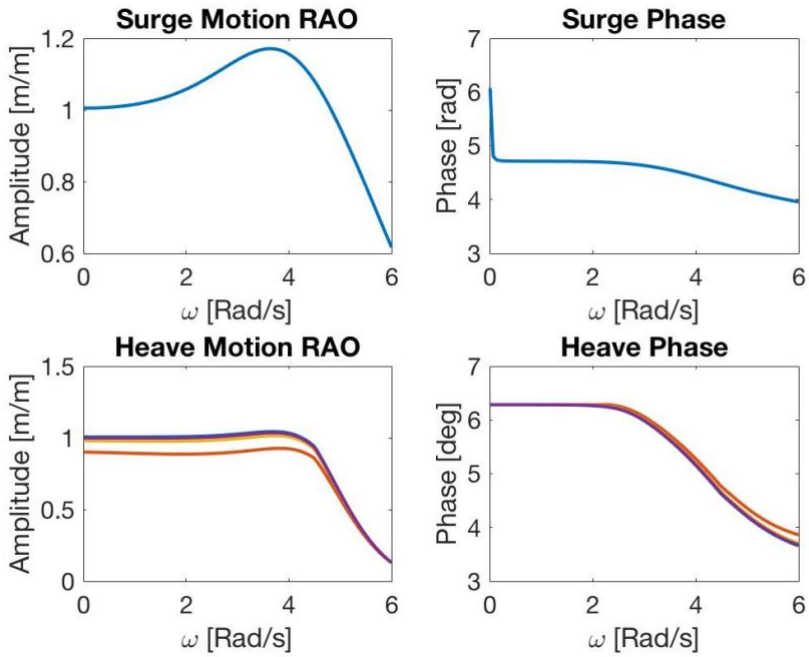

Figure 66 Frequency response characteristics case 5, the blue line indicates K0, the purple line KP050, the yellow line KP020 and the orange line KP005

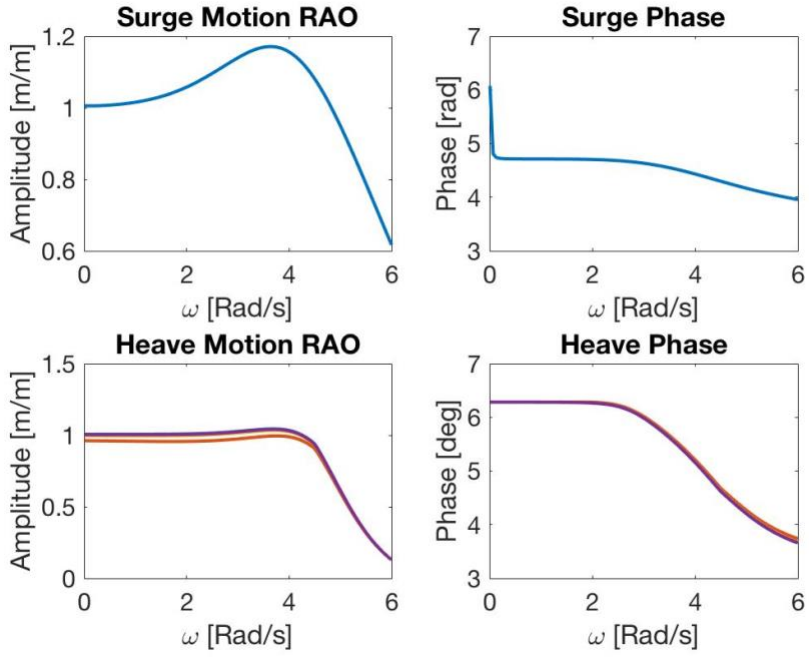

Figure 67 Frequency response characteristics case 6, the blue line indicates K0, the purple line KP050, the yellow line KP020 and the orange line KP005

Appendix J – Programmers' guide to PPR1 and PPR2

The data files generated by ComFLOW are of a certain binary file format. These files are flat binary files, they do not contain any metadata to interpret the data structure of the file. This makes it a very cumbersome task to write a straight-forward Matlab file, which is able to both read in the data files and calculate the desired results. It is also out of the scope of this thesis work to write a script which is able to do this. Therefore, the choice is made to alter the already existing post-processing tool (PPR1) that comes with ComFLOW, perform a few actions to reformat the data files and then use another self-written post-processing tool (PPR2) to retrieve the desired overtopping statistics.

The goal of this programmers' guide is to give a step-by-step description on how to retrieve the volume flux and overtopping statistics from the data files generated by ComFLOW.

Perform the following steps:

Step 1:
Add a folder named 'Matlabfiles' to the directory where your simulation was stored: …./ComFLOW/Runs/Simulation_XX

Step 2:
Open the createDerivedVariable.m file located in …./ComFLOW/ppr/@CMFSnapshot with Matlab.

Step 3:
See Table 13, it shows a part of the Matlab script createDerivedVariable.m. Add lines of code with green bar in front.

NOTE: Change line 513 to desired storage directory of files!: …./ComFLOW/Runs/ Simulation_XX /Matlabfiles

Step 4:
Open Matlab and change directory to the ppr folder: …/ComFLOW/ppr

Step 5:
In the command terminal of matlab:
- Type cmf_init and press enter
  - cmf_init.m has run
- Type comflow and press enter
  - comflow.m has run
  - Simulation editor/GUI ComFLOW starts up

Step 6:
In the simulation editor of PPR1:
- Choose simulation directory of simulation to be processed
- Click post-processing in the menu bar and open snapshots(2D/3D)
  - ComFLOW snapshotcenter opens

Step 7:
In the snapshotcenter of PPR1:
- Select data source
- Switch to 2D
- Select a random simulation file
- Switch to 2D plotting mode: XZ-plane
- Switch to U-component
- Press plot button and check if the U-component is plotted and XZ-plane visualized
- Click post-processing in the menu bar and open movie maker

Step 8:
In the movie maker of PPR1:
- Select plot set
- Check if all frames are selected
  - Select all frame box is ticked
- Generate movie
  - Every snapshot is now cycled through to be plot and added as a frame to the movie
  - While a snapshot is loaded and a plot is generated, the raw data of the ComFLOW file is addressed
  - Due to the lines added in createDerivedVariable.m, the data is stored into a .mat-format readable by Matlab.

Step 9:
In the editor of Matlab:
- Open a blank m-file and add the lines of code given in Table 11
- Change line 9 to the corresponding folder of the stored matlab files (see step 3)
- Save m-file as PPR2.m

Step 10:
Run PPR2.m

Execution of the PPR2 script outputs the overtopping statistics of the ComFLOW simulation.

```
                        obj.var.vortk.{k}(2:end-1,2:end-1,:) = (dvx-duy);
                    end
                end
            end
        end

    end

509.   datafile = obj.fnm;             %Full name datafile
510.   token = strtok(datafile,'.');  %Generate name for datafile to be saved
511.
512.   directory = cd;                 %original directory
513.   cd /Users/hansmaarten/'OneDrive - The Ocean Cleanup'/'Graduation
   project'/Model/Comflow/Runs/K0IWC2/Matlabfiles/ %change to storage directory
514.   save(token, 'obj')              %Save data as .mat file with token-name
515.   fprintf('file word opgeslagen onder %s \n',token)
516.   cd (directory);                 %change back to original directory



end
```

Table 10 Part of 'createDerivedVariable.m', lines of code with green bar in front to be added

```
1.
2.  %//In order to be able to read the input files, java classes have to be
3.  %added to the path, this is done by running cmf_init, from the PPR1 toolkit
4.  run [~~~location of ComFLOW folder~~~]/Comflow/ppr/cmf_init
5.
6.  %%//open the simulation editor  ~~mainly to remove annoying error showing in matlab
    terminal
7.  run [~~~location of ComFLOW folder~~~]/Comflow/ppr/comflow
8.
9.
10.
11.
12. %//change to storage directory of data files
13. cd [~~~location of ComFLOW folder~~~]/Model/Comflow/Runs/[~~~folder containing
    run~~~]/Matlabfiles/
14. working_folder = pwd;
15.
16. list_dir     = dir('*.mat');                  %//lists all files in directory
17. list_dir_cell = struct2cell(list_dir);          %//rewrite from struct to cell
18. fnm          = list_ dir_cell(1,:);             %List of filenames
19.
20.
21. cd [~~~location U_barrier file~~~]
22. velocity_barrier = xlsread('[name_file]','Sheet1','A1:[end]');
23.
24. for iii = 1:length(fnm)
25.    u_component(iii).U_barrier = velocity_barrier(iii)
26. end
27.
28. cd working_folder
29.
30. figure
31. for i = 1:length(fnm)
32.     matFilename = char(fullfile(working_folder, fnm(i)));
33.     matdata(i) =  load(char(matFilename));                  %//Read in data
34.     time(i) = matdata(i).obj.var.time;                      %//timestamp datafile
35.     fprintf('TIJD = %s \n',num2str(time(i)))
```

```
36.
37.     if i ==1
38.         dt(i)         = 0;
39.     else
40.         dt(i)         = time(i)-time(i-1);
41.     end
42.
43.     u_component(i).u = cell2mat(matdata(i).obj.var.u);
44.     u_component(i).u = u_component(i).u(:,4,:);
45.     u_component(i).u = permute(u_component(i).u,[3 1 2]);        %//u component
46.
47.     apperture(i).FB  = cell2mat(matdata(i).obj.var.fb);
48.     apperture(i).FB  = apperture(i).FB(:,4,:);
49.     apperture(i).FB  = permute(apperture(i).FB, [3 1 2]);        %//Volume apperture
50.
51.     fill_ratio(i).FS = cell2mat(matdata(i).obj.var.fs);
52.     fill_ratio(i).FS = fill_ratio(i).FS(:,4,:);
53.     fill_ratio(i).FS = permute(fill_ratio(i).FS, [3 1 2]);       %//Liquid fill ratio
54.
55.     apperture(i).FBCRD = apperture(i).FB;
56.     apperture(i).FBCRD(apperture(i).FBCRD ~= 0)                          = NaN;
57.     apperture(i).FBCRD(isnan(apperture(i).FBCRD))                        = 1; %//all
    boundary edges, including geometry edges now have a value of 0 and all fluid edges have a
    value of 1
58.
59.     size_ref = apperture(i).FBCRD;
60.     apperture(i).center   = regionprops(1 - apperture(i).FBCRD(4:(size(size_ref,1)-
    3),3:(size(size_ref,2)-2)), 'centroid');   %// center = regionprops(1 - FBCRD, 'centroid')
    als ook rand bc 1
61.     apperture(i).i_center = round(apperture(i).center.Centroid(1))+2;
    %//Cell edge located at midpoint barrier (x-direction)
62.     apperture(i).j_center = round(apperture(i).center.Centroid(2))+3;
    %//Cell edge located at midpoint barrier (z-direction)
63.
64.     apperture(i).FB_check = apperture(i).FB(apperture(i).j_center,apperture(i).i_center);
    %//Check if cell edge has 0 value
65.     if apperture(i).FB_check == 0
66.         apperture(i).message1 = 'Barrier gevonden';
67.         disp(apperture(i).message1)
68.     else
69.         apperture(i).message1 = sprintf('Barrier NIET GEVONDEN');
70.         uiwait(warndlg(apperture(i).message1));
71.         return
72.     end
73.
74.      u_component(i).u_FS_cells    =  apperture(i).FBCRD.*u_component(i).u;          %//u-
    components of fluid cells
75.      u_component(i).u_at_face     =  u_component(i).u_FS_cells(:,apperture(i).i_center);
    %//u components fluid cell at face edge location barrier
76.
77.      u_plot = u_component(i).u_FS_cells;              %//generate value for plot
78.      u_plot(u_plot == 0) = NaN;                       %//set all zero values to NaN
79.
80.      contourf(1-apperture(i).FB,[.49 .51]);           %//fill boundary cells (drawing of
    geometry)
81.      hold on
82.      image = imagesc(u_plot);                         %//draw U-velocities
83.      colormap('jet')                                  %//Uses jet color scheme
84.      set(image,'alphadata',~isnan(u_plot))            %//Ignores NaN values and sets NaN
    values to background colour
85.      colorbar                                         %//Adds a colorbar
86.      caxis([-2.25 2.75]);                             %//Set axis
87.      hold on
```

```
      full = fill_ratio(i).FS >.99;                                          %//Set conditions free surface (conditions based on PPR1)
      fsvar2 = (1-full).*fill_ratio(i).FS./(fill_ratio(i).FS+0.5) + full; %//Set conditions free surface (conditions based on PPR1)
      B = contour(fsvar2,[.5 .5],'LineWidth',2,'LineColor','blue');       %//draw free surface line
      hold on

   plot(apperture(i).i_center,apperture(i).j_center,'*','MarkerSize',4,'MarkerFaceColor','r') %//plot location center cell edges
      hold off
      axis([(size(u_component(1).u,2)/2-10) (size(u_component(1).u,2)/2+10) 65 85])
      title(['Time = ' num2str(time(i)) ' s '])
      drawnow
     % pause(.5)

dz = cell2mat(matdata(1).obj.grid.dzpmin);     %//dz [m]
   dy = cell2mat(matdata(1).obj.grid.dypmin);     %//dy [m]


       for j = apperture(i).j_center:size(u_component(i).u,1)

               u_component(i).u_ab(j)    = u_component(i).u_at_face(j);  %//u components at face above barrier center

       End

   dummy_var = u_component(i).u_ab

   for ii = 1:length(dummy_var)
        if dummy_var(ii)==0
           difference_U(ii) = 0;
        else
           difference_U(ii) = dummy_var(ii) - u_component(i).U_barrier; %Difference Velocity fluid and barrier
        end
   end
   u_component(i).u_ab_diff = difference_U


   %//Conversion of data to only keep positive u components at face above
   %barrier center, choice is made that negative flow rates are not
   %counted "once overtopped, volume is lost"
       u_component(i).u_ab_pos  = differency_U
       u_component(i).u_ab_pos(u_component(i).u_ab_pos<=0) = 0;

       %//Determination of volumetric flow trough surface per meter section of
       %the barrier according to equation 62 in Thesis rapport
       overtopping(i).VF_per_cell    = fill_ratio(i).FS(:,apperture(i).i_center-1)'.*u_component(i).u_ab_pos*(dz/dy);
       VF_total(i)                   = sum(overtopping(i).VF_per_cell);


   end

   Figure
   fill([0 0 100 100],[0 3 3 0], [0.8 0.8 0.8], 'EdgeColor', 'none')
   hold on
   plot(time,VF_total,'Color', [0 0.4470 0.7410]);title('Volumetric flow rate per meter section over barrier');xlabel('T [s]');ylabel('Q/m [(m^2/s)/m]');
   set(gca,'ylim', [0 3]);

   %//Total overtoppping volume per meter section of barrier according to
   %equation 63 in Thesis rapport
```

```
143.    Overtopping_volume = VF_total*dt';
```

Table 11 Script of code to derive overtopping flux and overtopping volume

Appendix K – Overtopping statistics: Volumetric flow rate

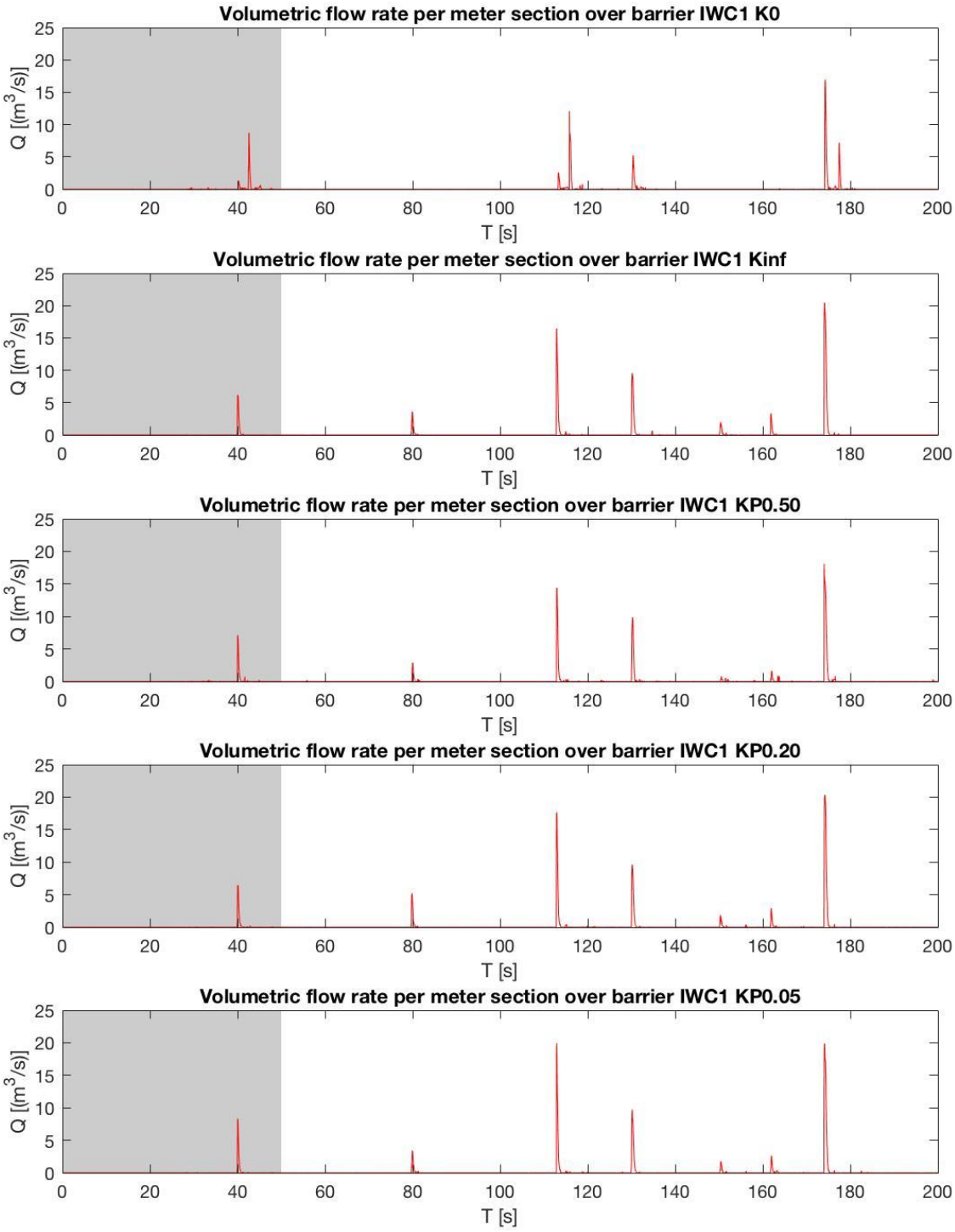

Figure 68 Volumetric flow rate case 1 [NOTE LIMITS Y-AXIS]

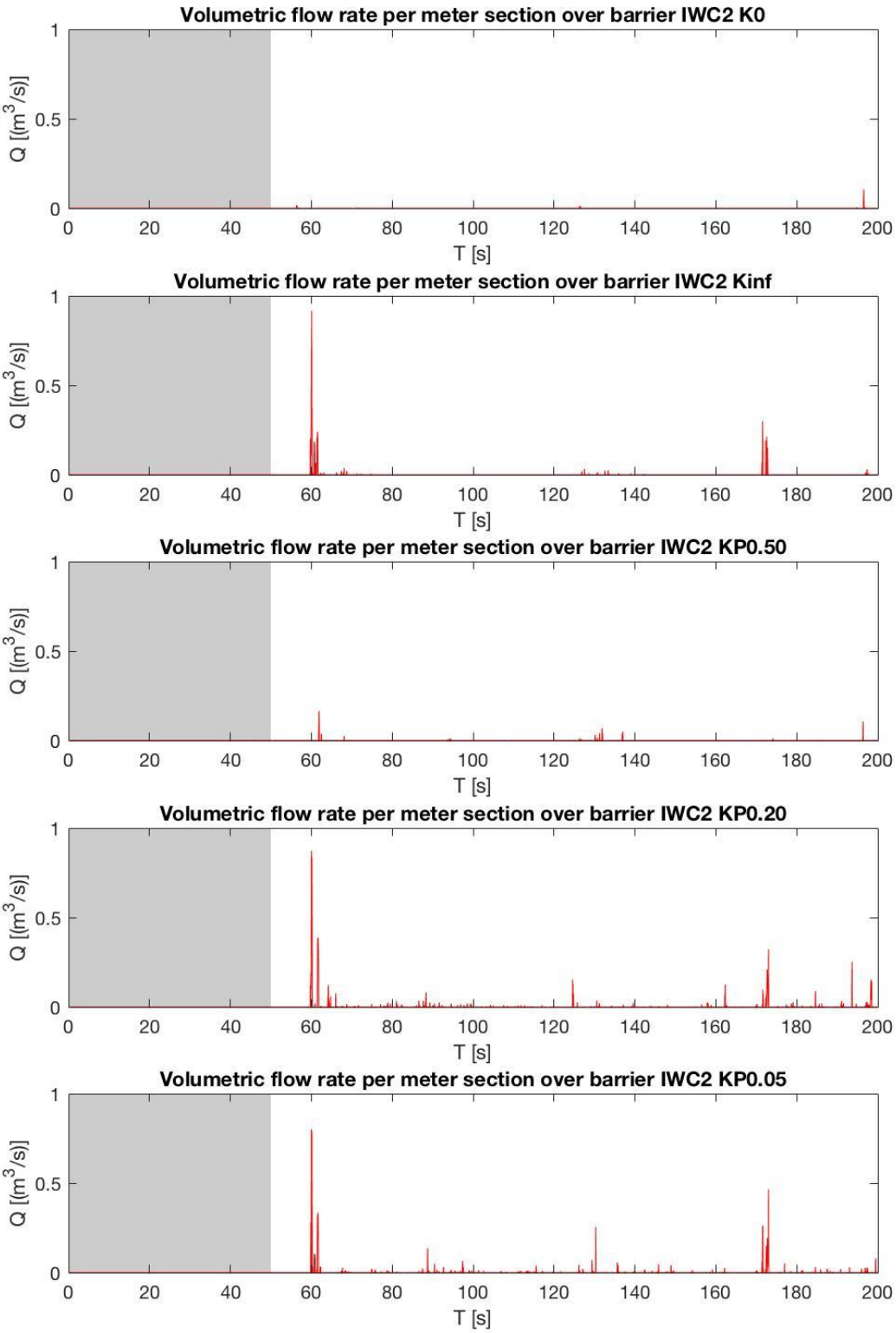

Figure 69 Volumetric flow rate case 2 [NOTE LIMITS Y-AXIS]

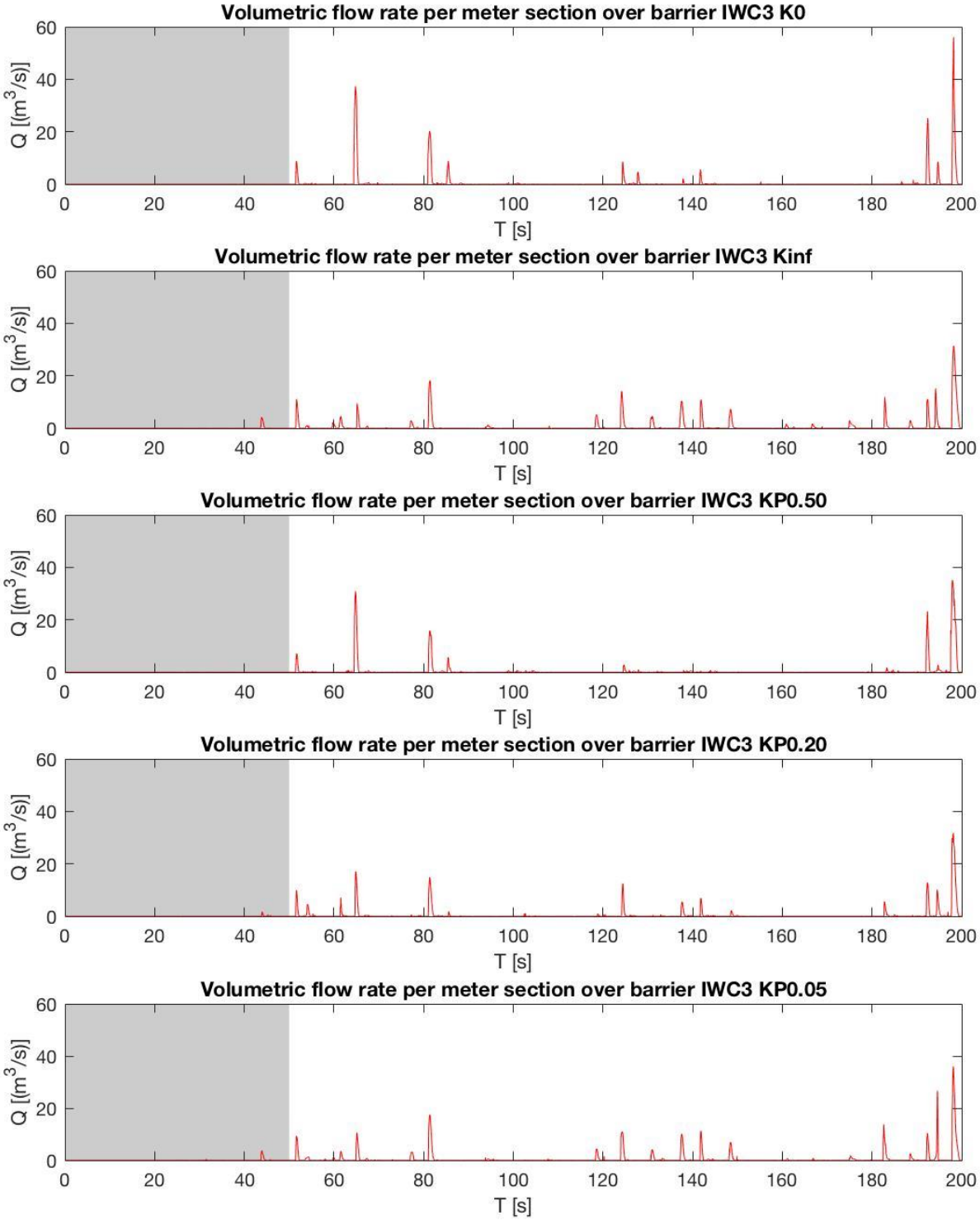

Figure 70 Volumetric flow rate case 3 [NOTE LIMITS Y-AXIS]

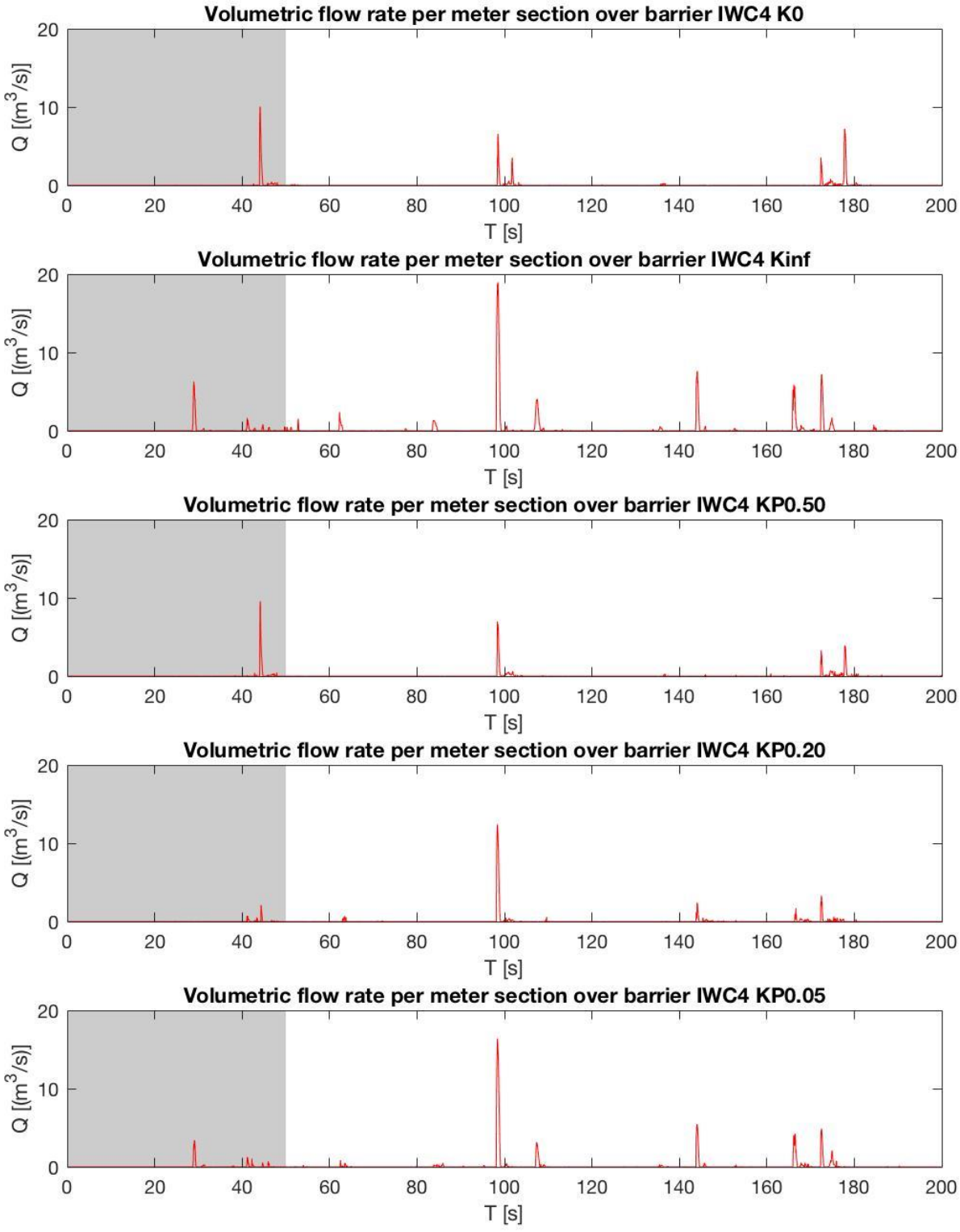

Figure 71 Volumetric flow rate case 4 [NOTE LIMITS Y-AXIS]

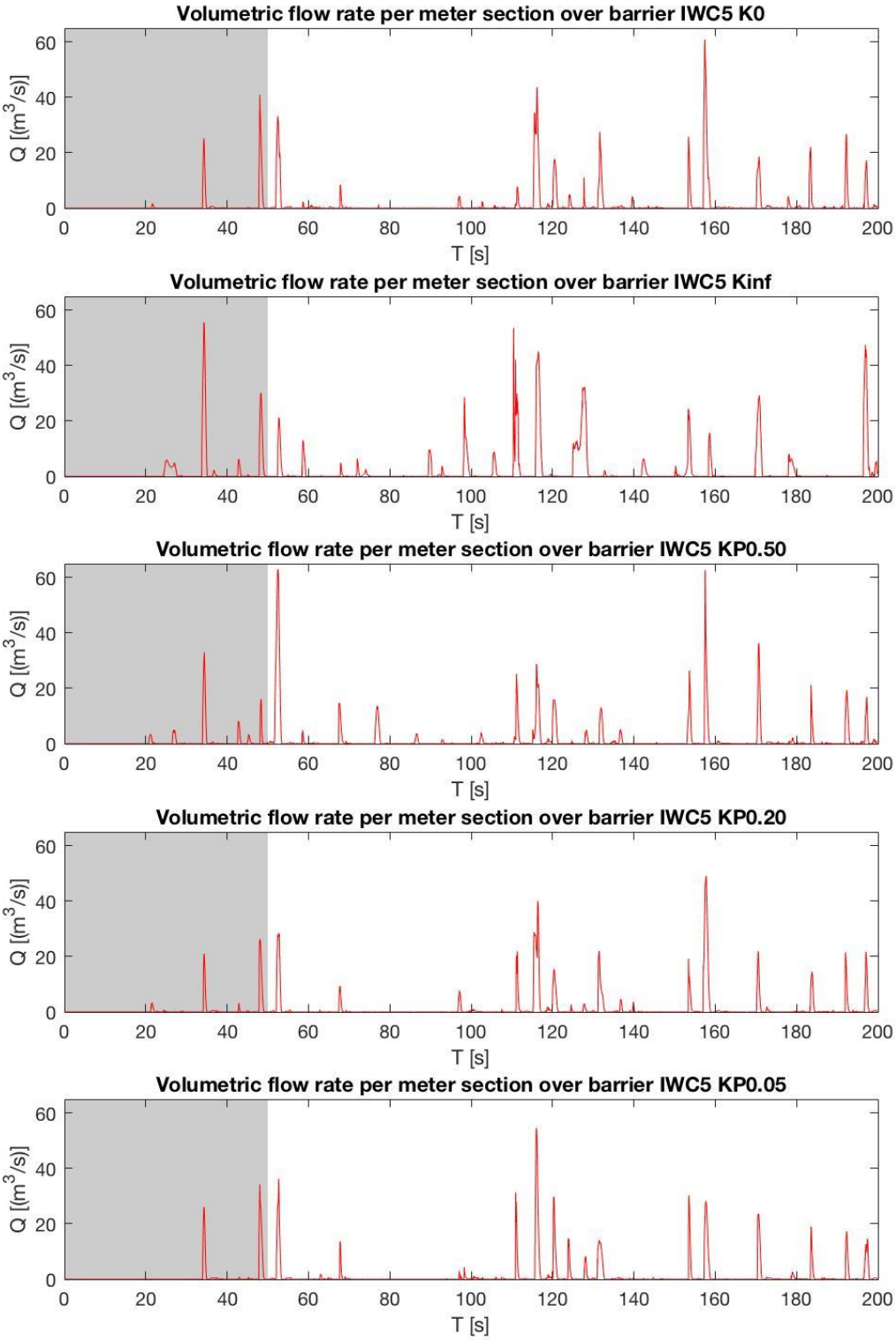

Figure 72 Volumetric flow rate case 5 [NOTE LIMITS Y-AXIS]

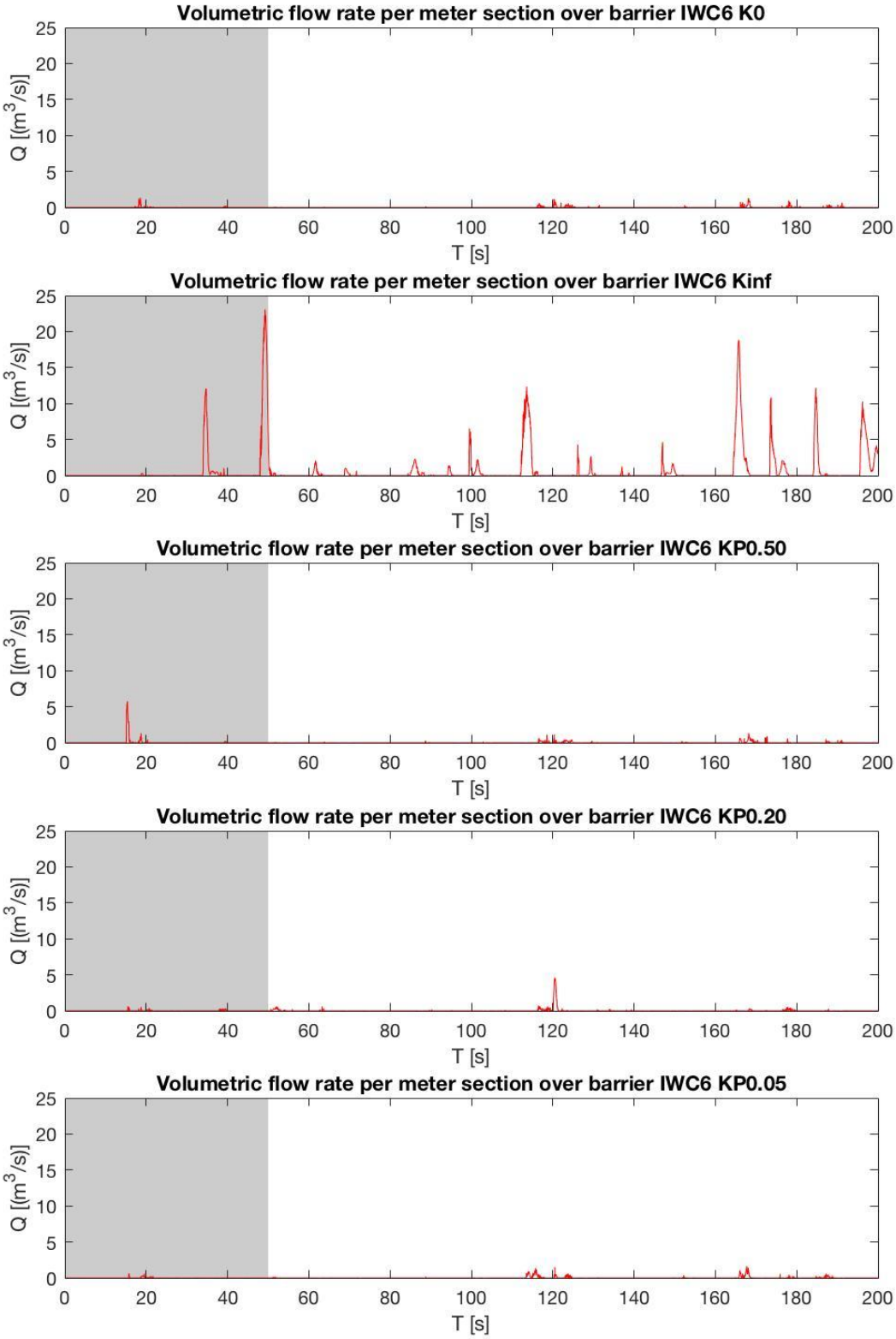

Figure 73 Volumetric flow rate case 6 [NOTE LIMITS Y-AXIS]

Appendix L – Overtopping statistics: Total overtopping volumes

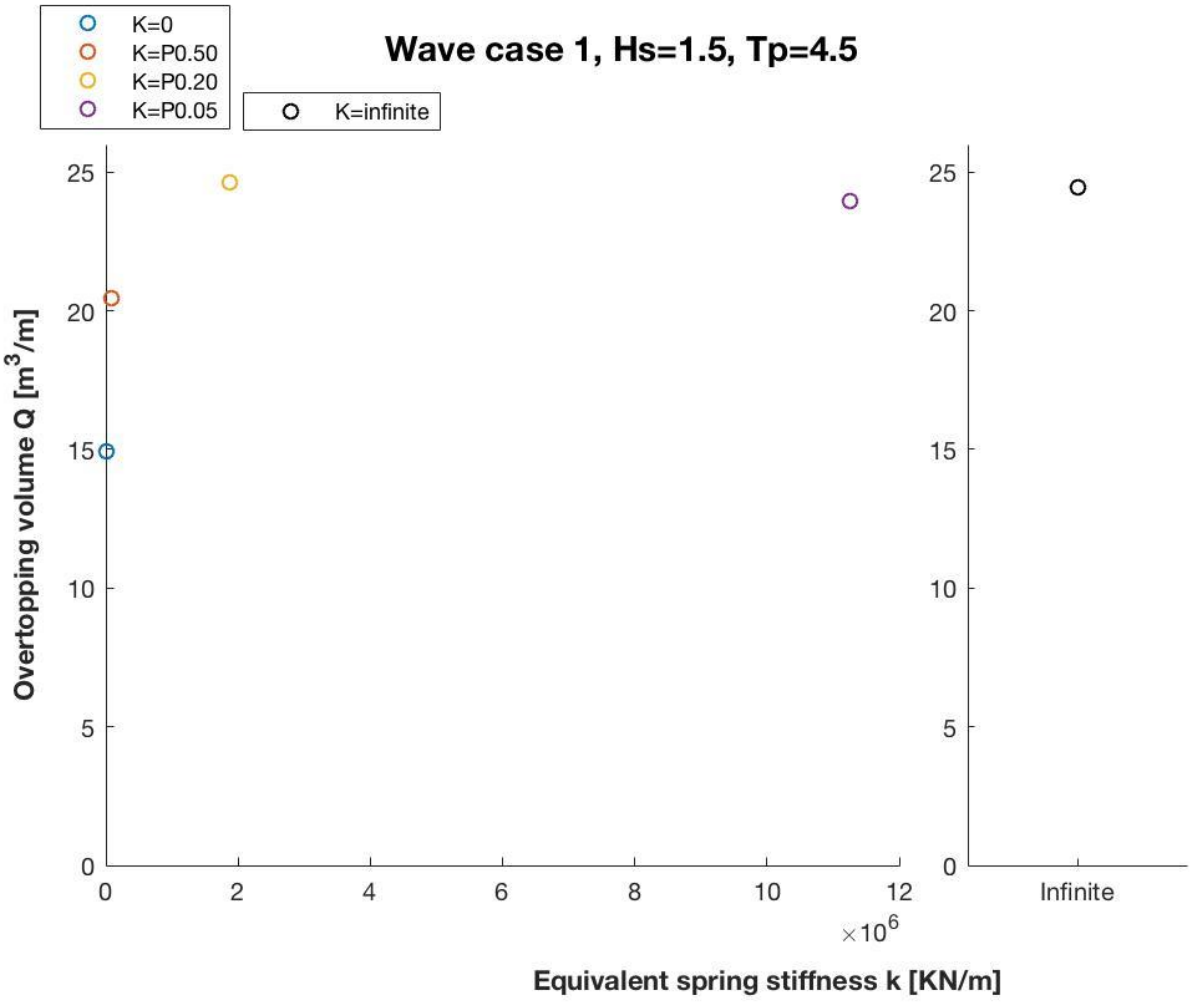

Figure 74 Total overtopping volume against spring stiffness: Case 1 (Hs=1.5m, Tp=4.5s) [NOTE LIMITS Y-AXIS]

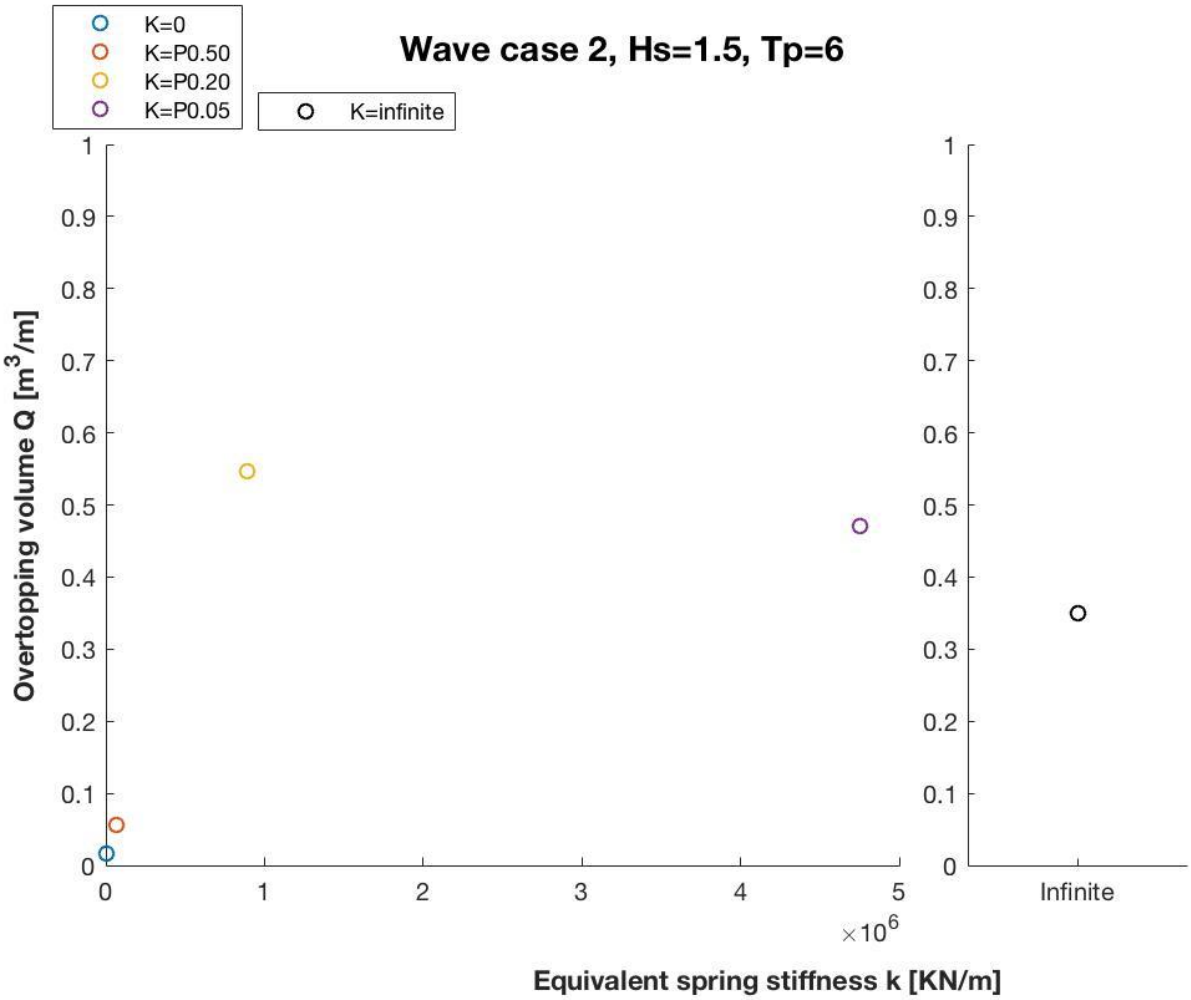

Figure 75 Total overtopping volume against spring stiffness: Case 2 (Hs=1.5m, Tp=6s) [NOTE LIMITS Y-AXIS]

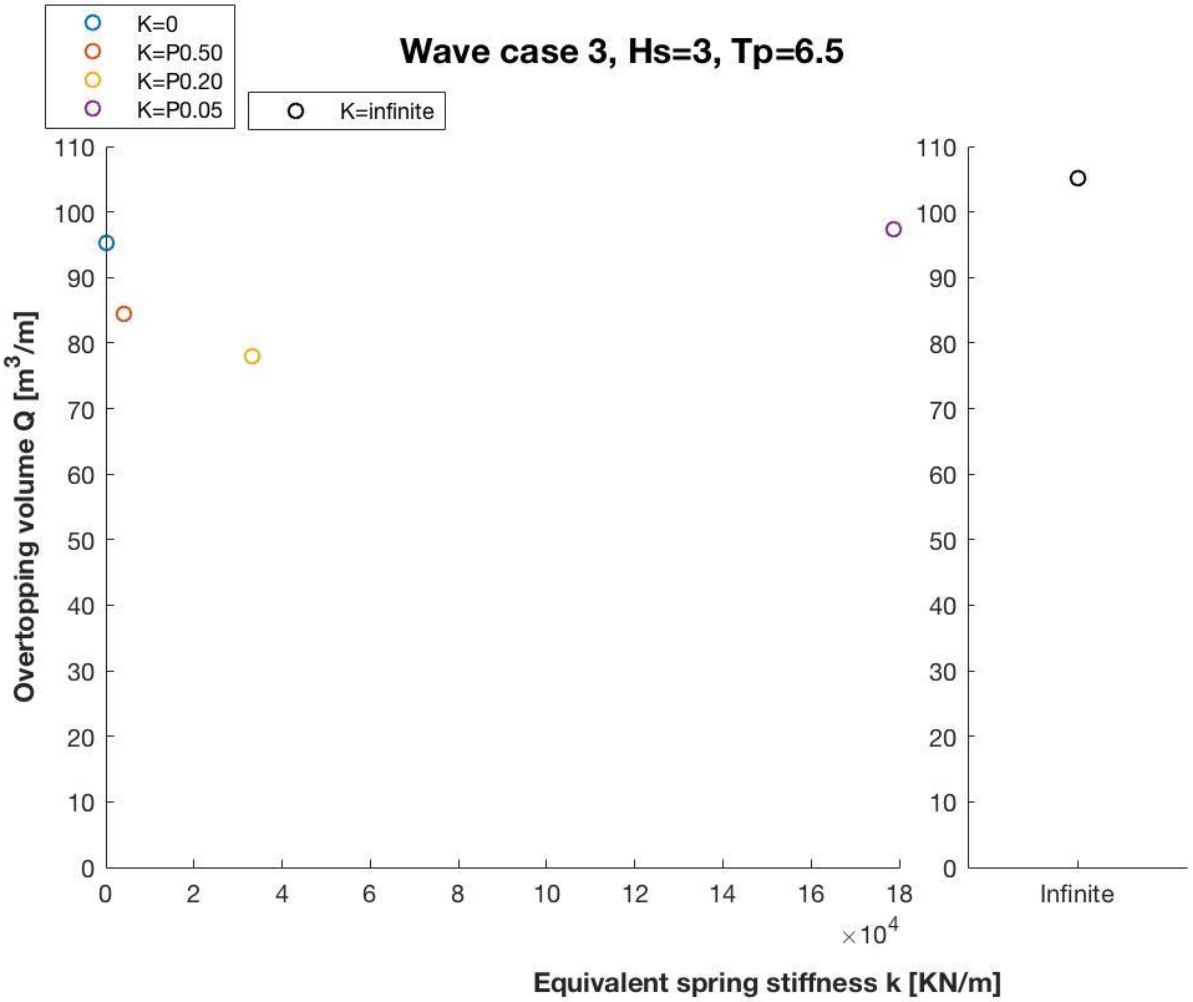

Figure 76 Total overtopping volume against spring stiffness: Case 3 (Hs=3, Tp=6.5) [NOTE LIMITS Y-AXIS]

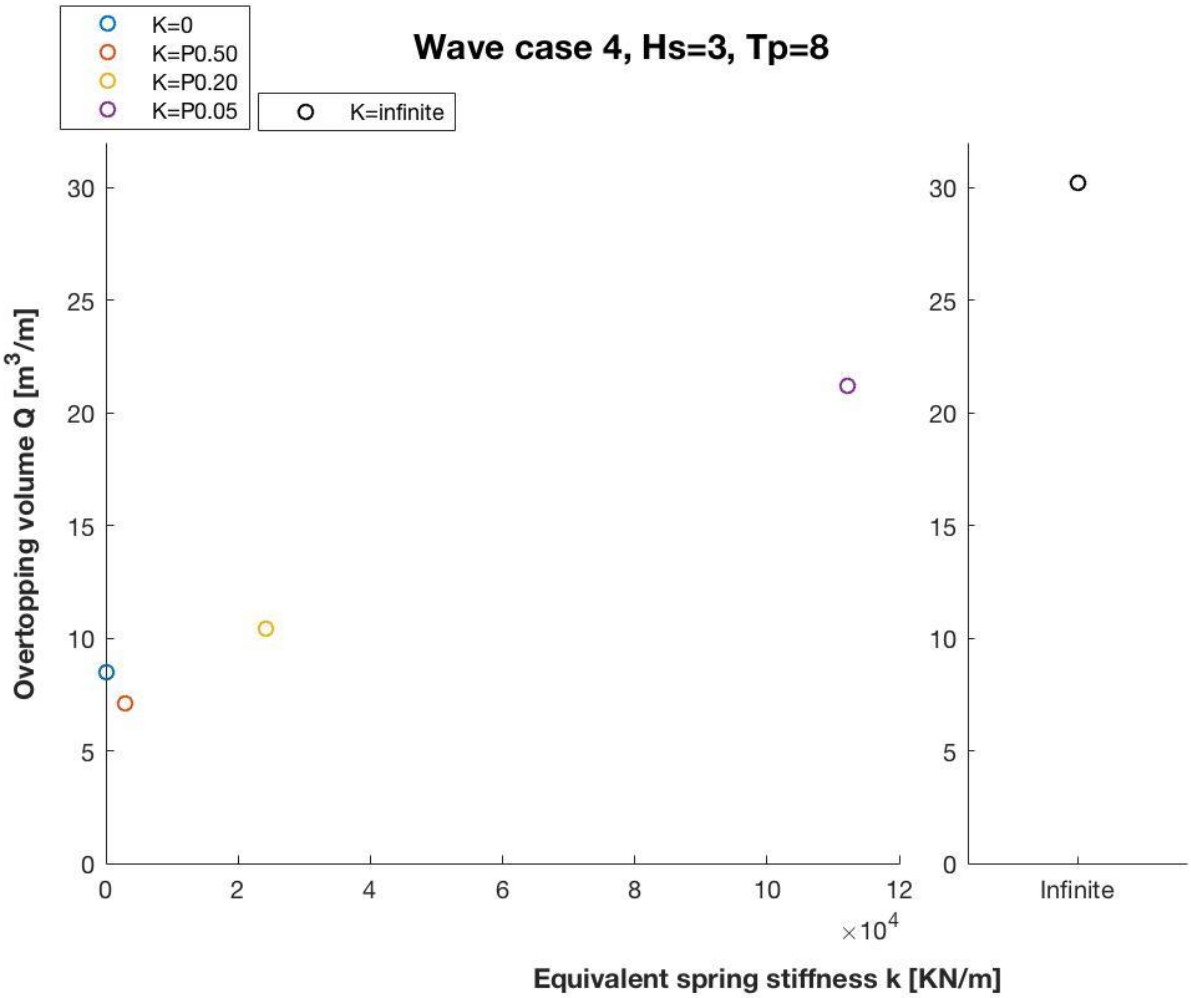

Figure 77 Total overtopping volume against spring stiffness: Case 4 (Hs=3m, Tp=8s) [NOTE LIMITS Y-AXIS]

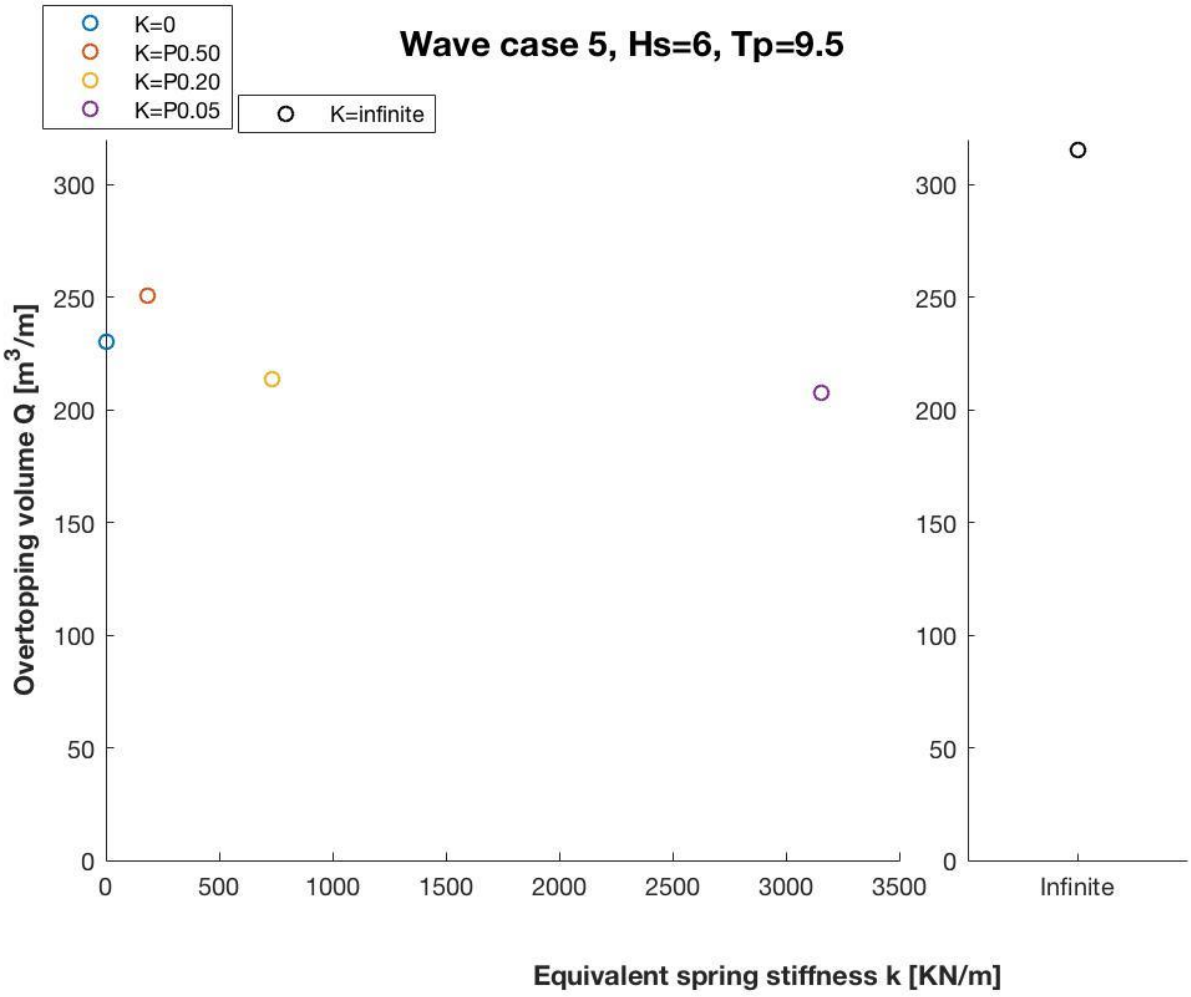

Figure 78 Total overtopping volume against spring stiffness: Case 5 (Hs=6m, Tp=9.5s) [NOTE LIMITS Y-AXIS]

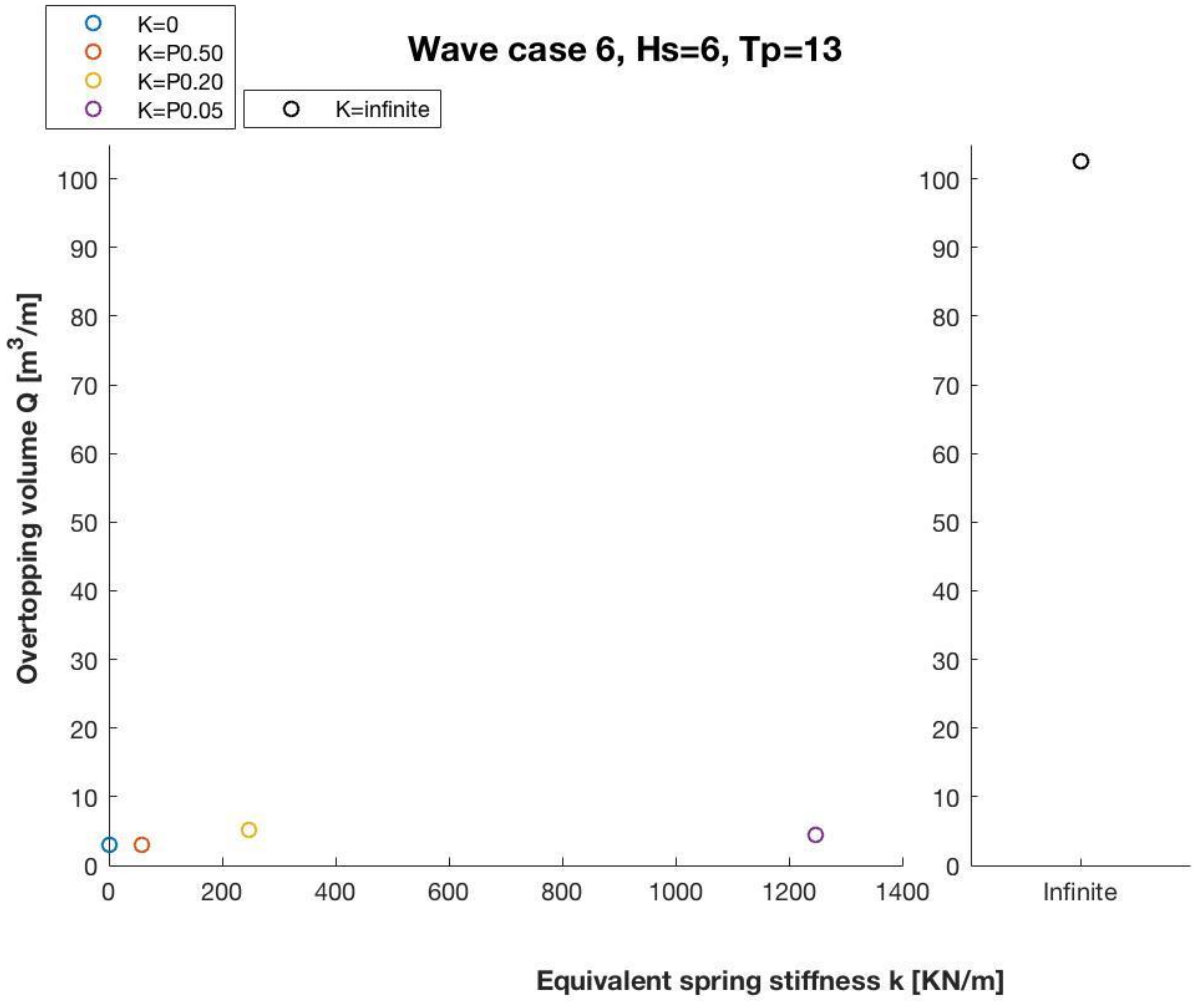

Figure 79 Total overtopping volume against spring stiffness: Case 6 (Hs=6m, Tp=13s) [NOTE LIMITS Y-AXIS]

Appendix M – Overtopping statistics: Total overtopping volume vs steepness

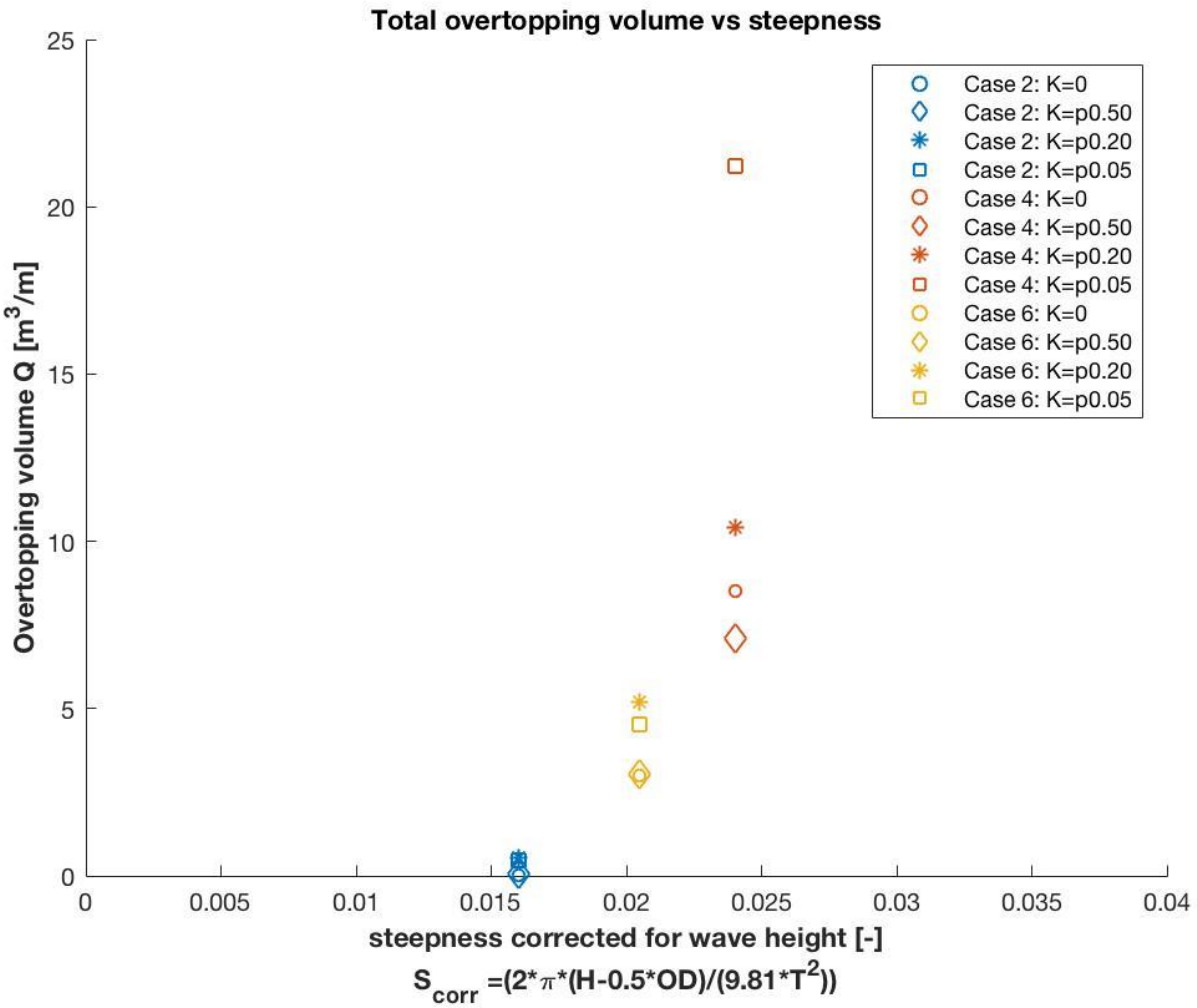

Figure 80 Overtopping volume plotted against wave steepness (corrected for wave height) for the wave cases 2, 4 and 6

Appendix N – Visualization of wave breaking event

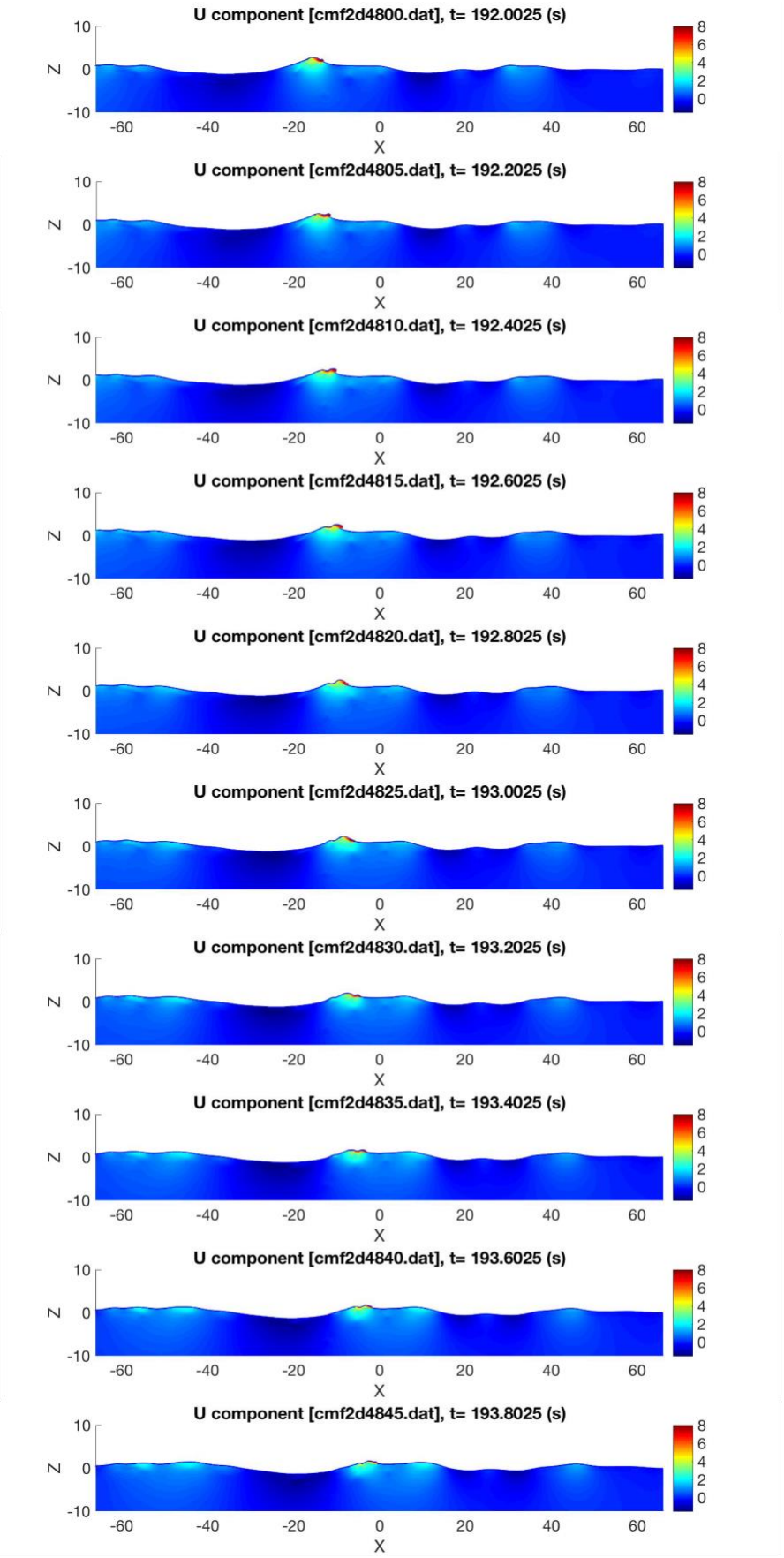

Figure 81 Wave breaking event occurring in the simulation of wave case 3

Appendix O – Wave check

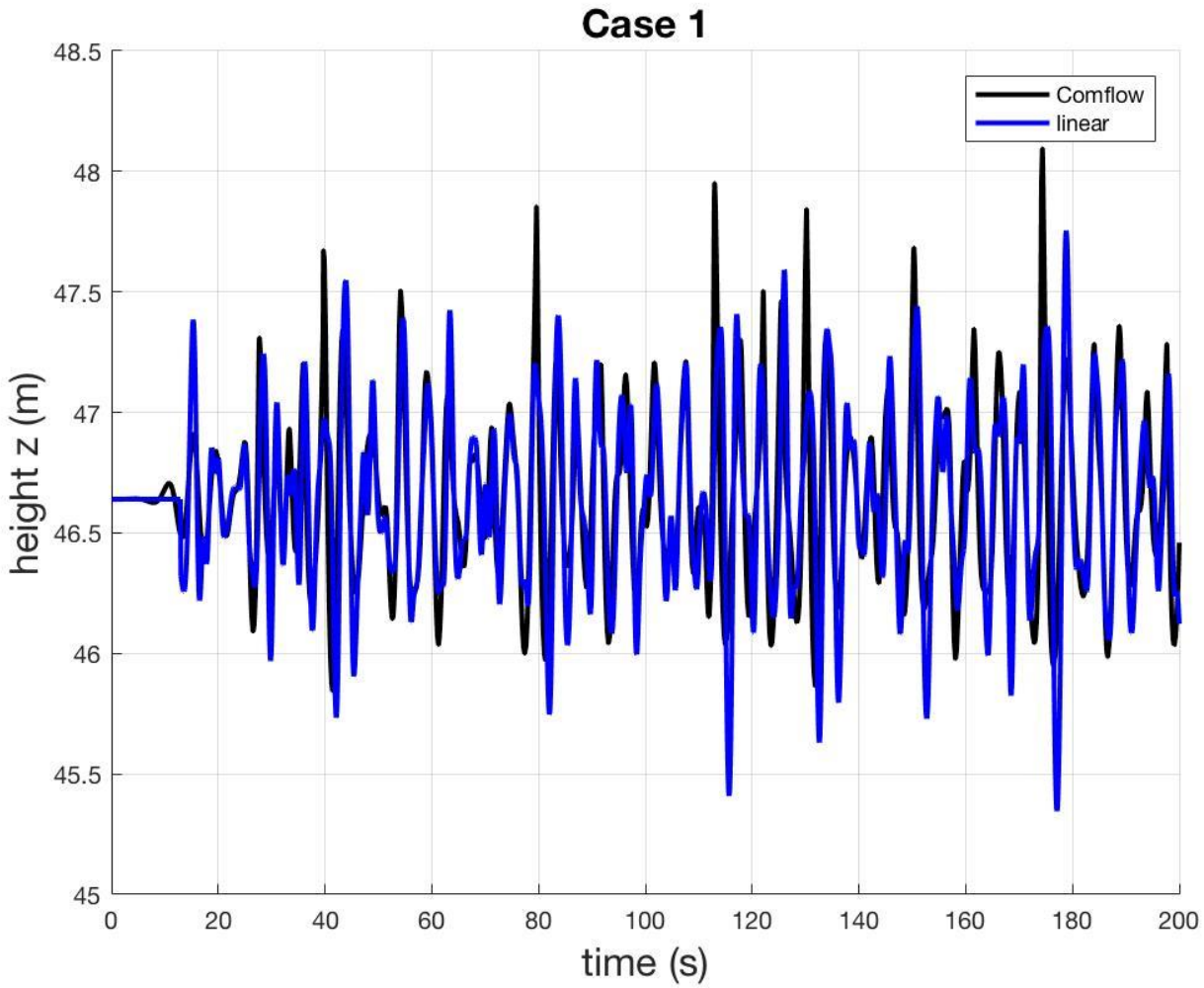

Figure 82 Comparison of linear wave signal inputted in hydrodynamic model with simulated wave in ComFLOW for environmental case 1 (Hs=1.5 Tp=4.5)

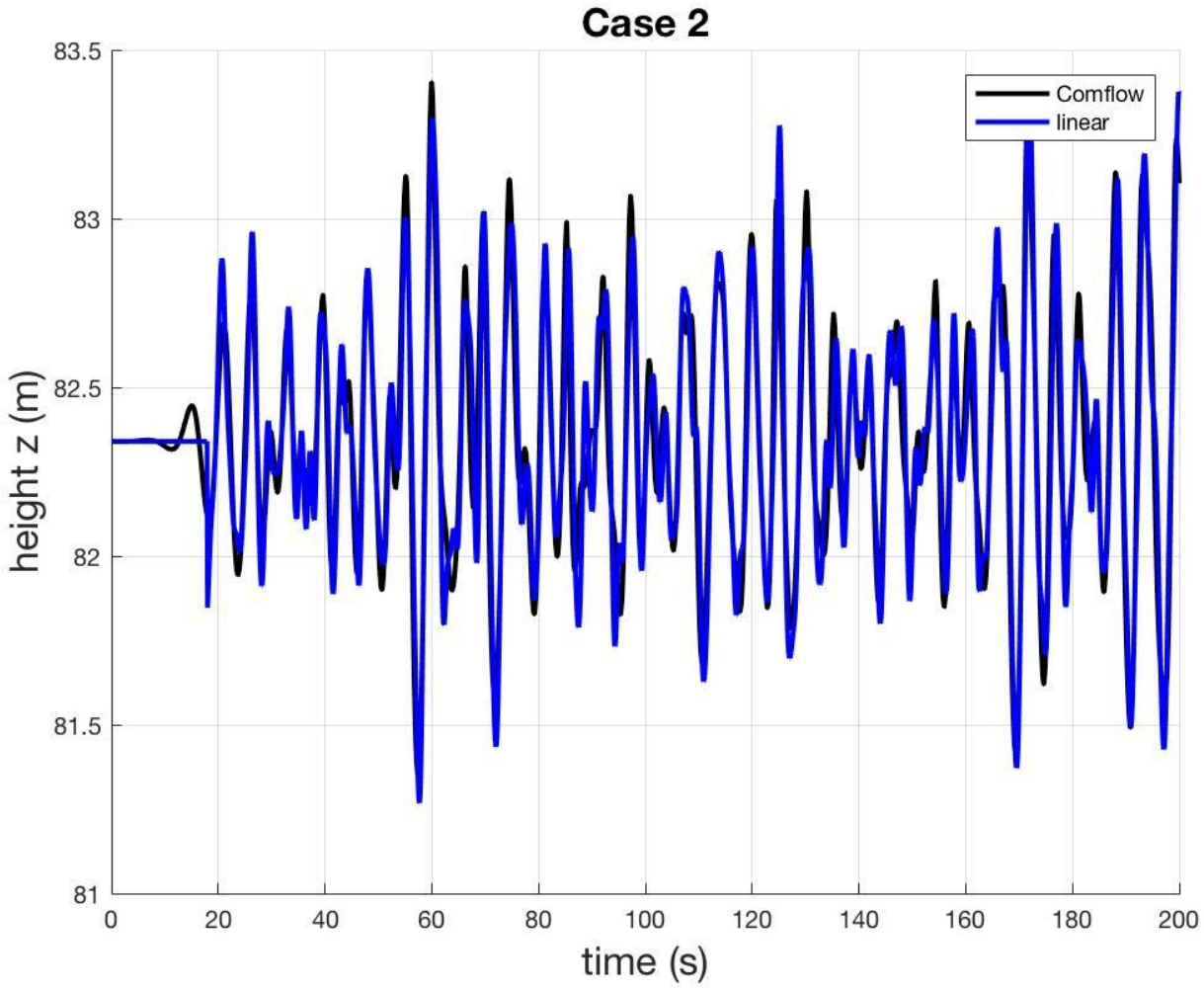

Figure 83 Comparison of linear wave signal inputted in hydrodynamic model with simulated wave in ComFLOW for environmental case 2 (Hs=1.5 Tp=6)

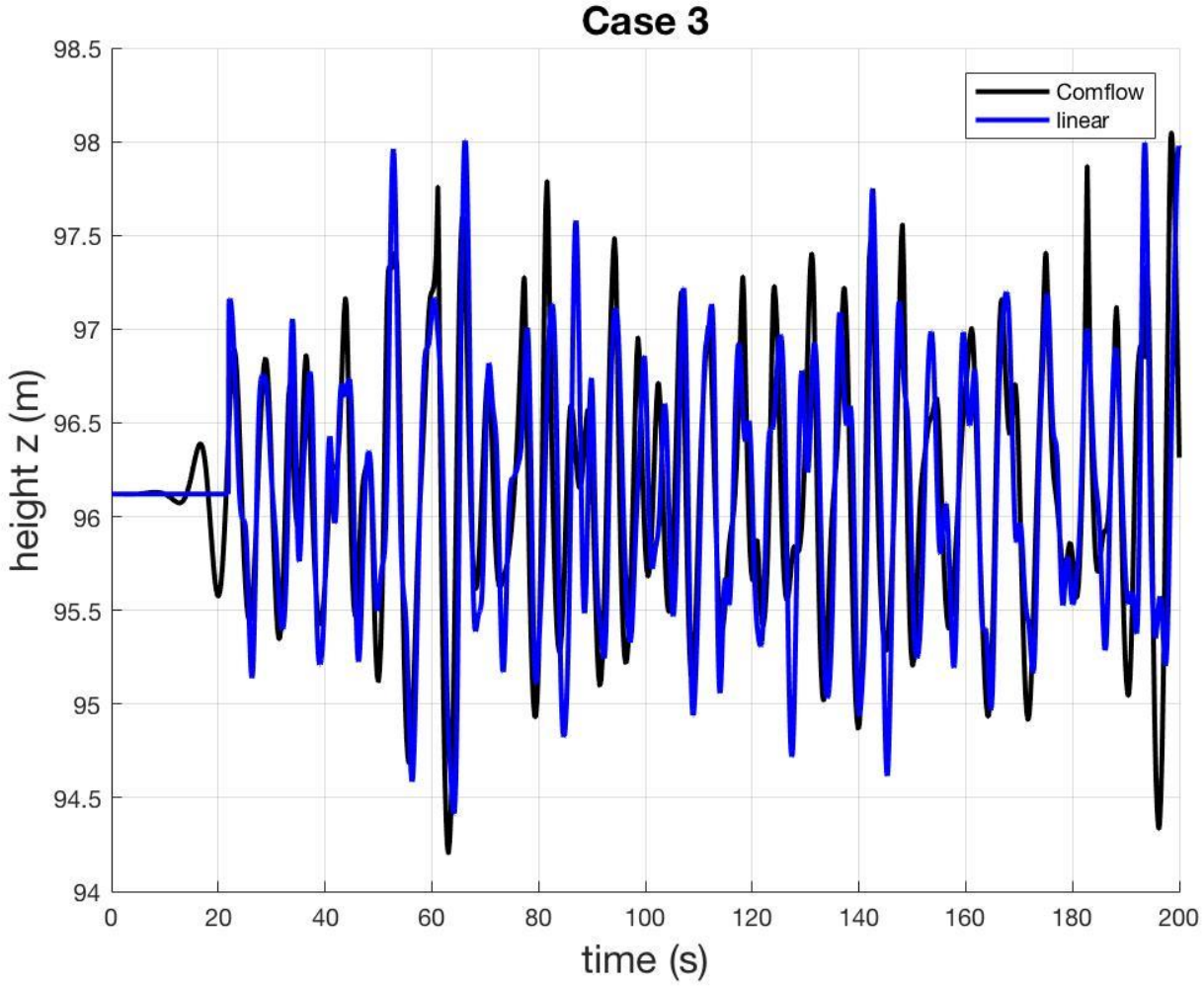

Figure 84 Comparison of linear wave signal inputted in hydrodynamic model with simulated wave in ComFLOW for environmental case 3 (Hs=3 Tp=6.5)

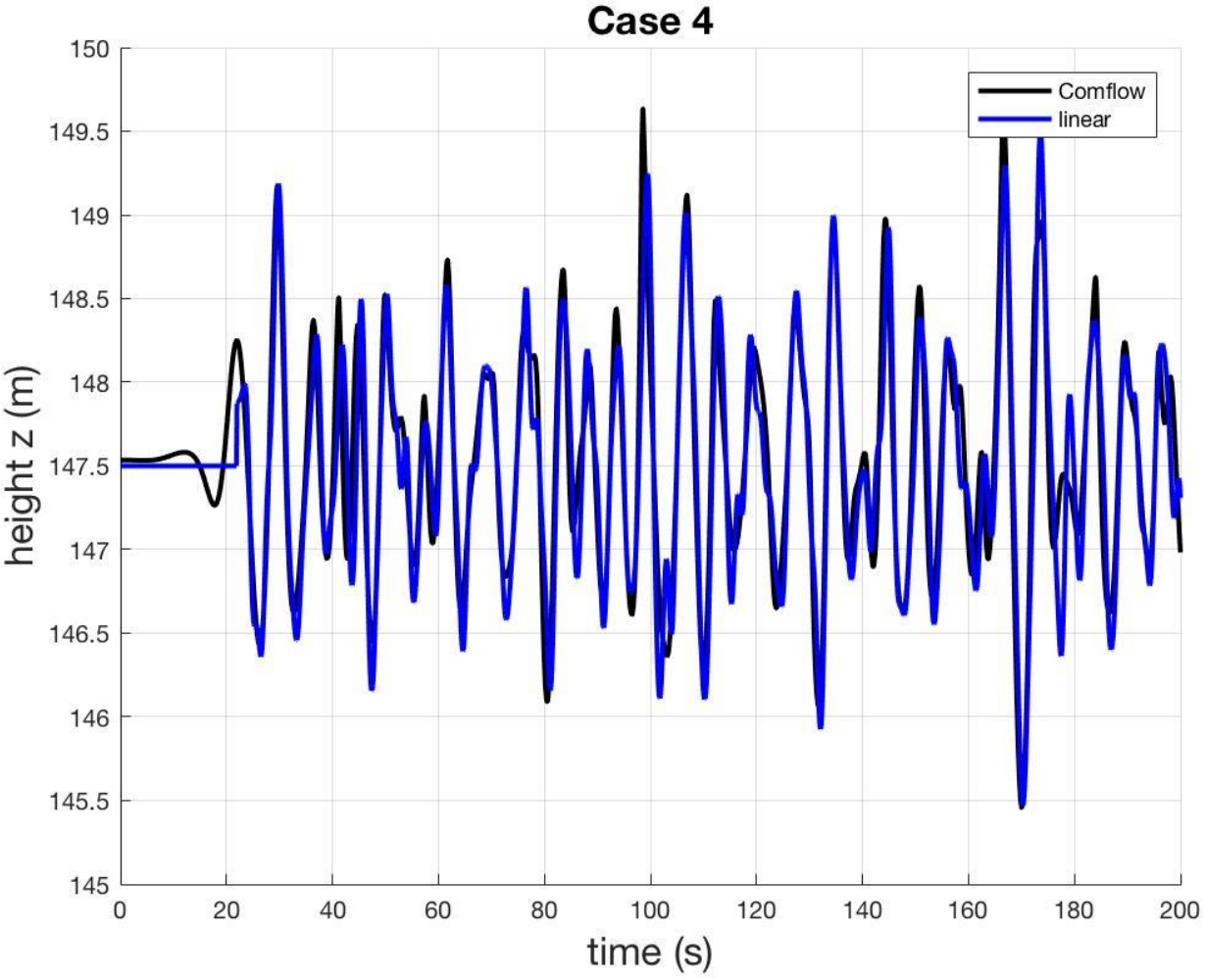

Figure 85 Comparison of linear wave signal inputted in hydrodynamic model with simulated wave in ComFLOW for environmental case 4 (Hs=3 Tp=8)

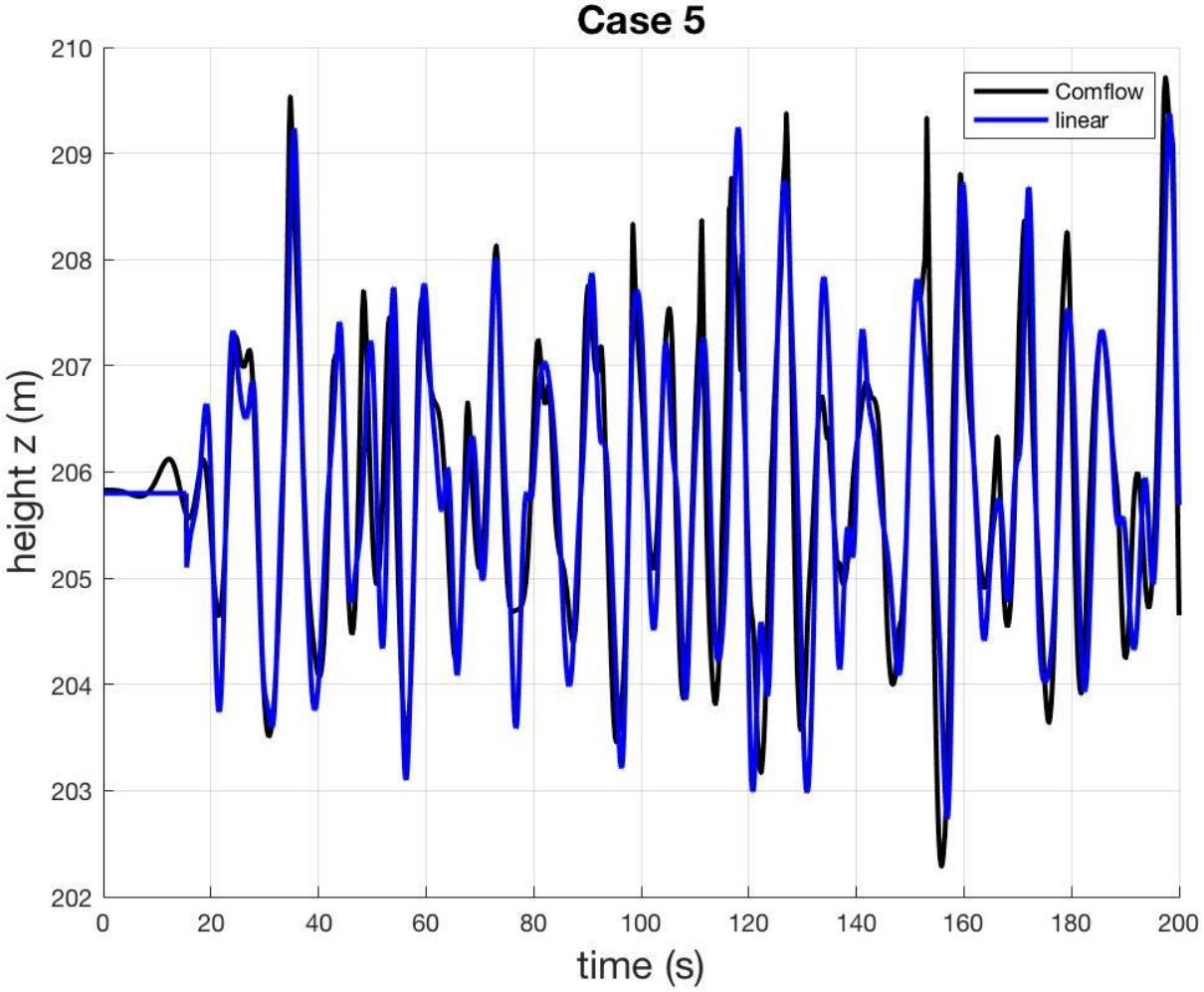

Figure 86 Comparison of linear wave signal inputted in hydrodynamic model with simulated wave in ComFLOW for environmental case 5 (Hs=6 Tp=9.5)

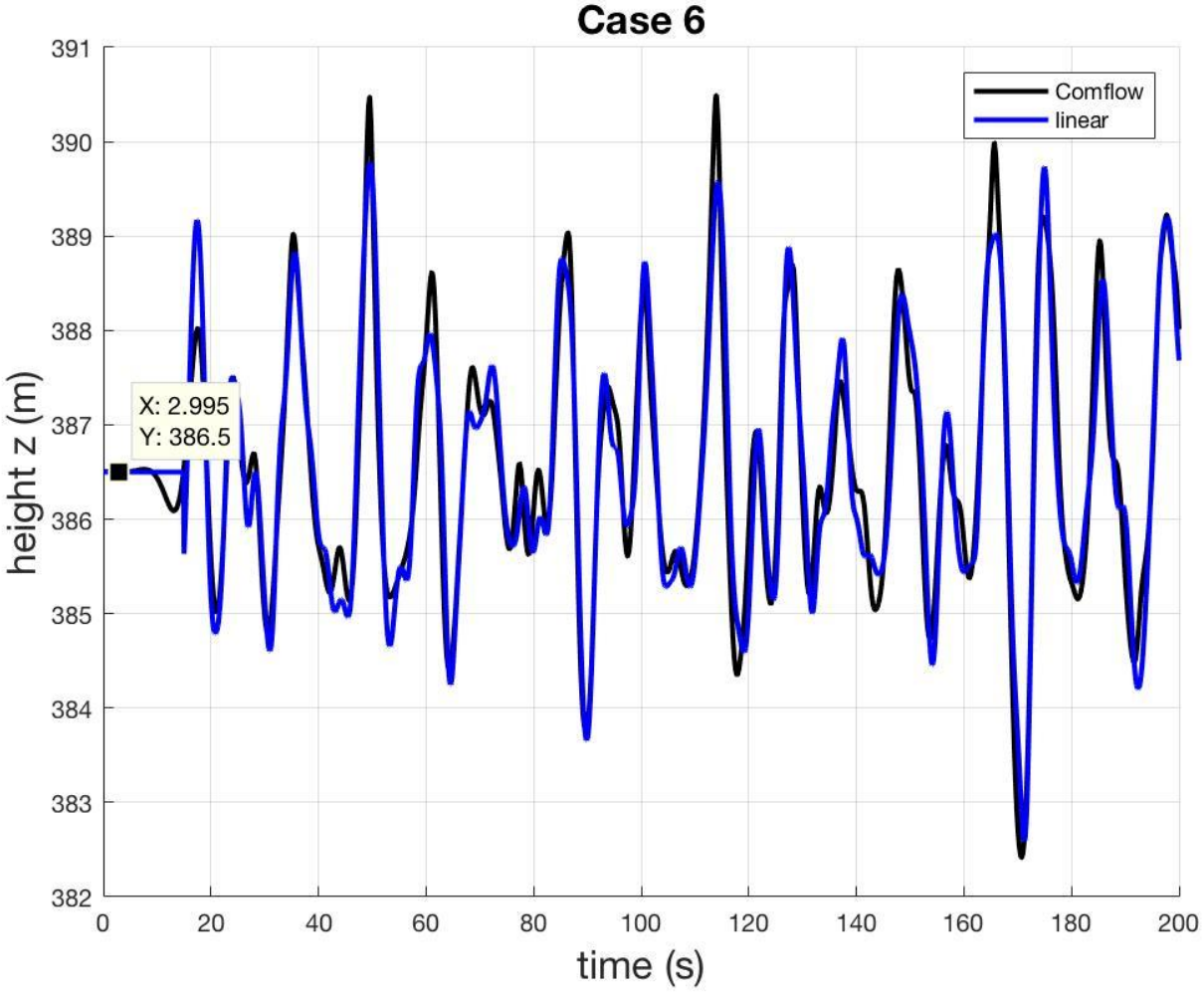

Figure 87 Comparison of linear wave signal inputted in hydrodynamic model with simulated wave in ComFLOW for environmental case 6 (Hs=6 Tp=13)